Carnegie Mellon University
CARNEGIE INSTITUTE OF TECHNOLOGY

THESIS

Submitted in Partial fulfillment of the Requirements

For the Degree of Doctor of Philosophy

TITLE

Simulation of Granular and Gas-Solid Flows Using Discrete Element Method

PRESENTED BY

Dhanunjay S. Boyalakuntla

ACCEPTED BY THE DEPARTMENT OF MECHANICAL ENGINEERING

MAJOR PROFESSOR Date

DEPARTMENT HEAD Date

APRROVED BY THE COLLEGE COUNCIL

DEAN Date

CARNEGIE MELLON UNIVERSITY

Simulation of Granular and Gas-Solid Flows Using Discrete Element Method

A DISSERTATION

SUBMITTED TO THE GRADUATE SCHOOL

IN PARTIAL FULFILLMENT OF THE REQUIREMENT

For the Degree

of

DOCTOR OF PHILOSOPHY

in

MECHANICAL ENGINEERING

by

DHANUNJAY S. BOYALAKUNTLA

Pittsburgh, Pennsylvania
December 2003

To My Parents and Swami

Abstract

In recent years there has been increased research activity in the experimental and numerical study of gas-solid flows. Flows of this type have numerous applications in the energy, pharmaceuticals, and chemicals process industries. Typical applications include pulverized coal combustion, flow and heat transfer in bubbling and circulating fluidized beds, hopper and chute flows, pneumatic transport of pharmaceutical powders and pellets, and many more. The present work addresses the study of gas-solid flows using computational fluid dynamics (CFD) techniques and discrete element simulation methods (DES) combined. Many previous studies of coupled gas-solid flows have been performed assuming the solid phase as a continuum with averaged properties and treating the gas-solid flow as constituting of interpenetrating continua. Instead, in the present work, the gas phase flow is simulated using continuum theory and the solid phase flow is simulated using DES. DES treats each solid particle individually, thus accounting for its dynamics due to particle-particle interactions, particle-wall interactions as well as fluid drag and buoyancy. The present work involves developing efficient DES methods for dense granular flow and coupling this simulation to continuum simulations of the gas phase flow.

In this thesis, existing models (viz. the hard sphere and soft sphere models) for DES for spherical particles have been explored and the soft sphere model has been implemented. Efficient search algorithms and data structures for computing inter-particle interaction have been explored. Two different search algorithms, No-binary Search

(NBS), and Quadtree/Octree search, have been implemented. The former provides an O(N) search procedure for like-sized particles. The latter is an O(NlogN) procedure, but can admit particles of different sizes.

Coupling of DES for solids and continuum for gas/liquid flow has also been done. The fluid flow computation has been done using MFIX, a solver developed at the Department of Energy's National Energy Technology Laboratory (NETL) for multiphase flows; the DES simulation provides the particle dynamics. In order to complete the coupled calculations, the void fraction and the volume averaged cell solid volume velocity corresponding to the DES particle distribution are computed. Interphase drag is computed from experimental correlations. Pressure force on the solids is also computed. Finally, a segregated coupling algorithm for the fluid and solid is used, with several DES time steps constituting one fluid time step. Granular temperature calculations are also done.

The DES-MFIX coupled code developed has been used to address two areas of industrial importance (i) granular material behavior with no fluid interaction (ii) gas-solid flows. For granular material behavior vibrated granular beds have been studied. For gas-solid flows, fluidized beds, which are of great importance in chemical engineering have been studied.

Simulations have been performed to observe pure granular behavior in vibrating beds. Benchmark cases have been simulated and the results obtained match the published literature. The dimensionless acceleration amplitude and the bed height are the parameters governing bed behavior. Various interesting behaviors such as heaping, round and cusp surface standing waves, as well as kinks, have been observed for different

values of the acceleration amplitude for a given bed height. Furthermore, binary granular mixtures (granular mixtures with two particle sizes) in a vibrated bed have also been studied. In the kink formation regime, binary mixtures have been found to demonstrate horizontal segregation, wherein the bigger particles cluster at the kinks thus forming alternate sections of big and small particles. Though this phenomenon must be confirmed using three-dimensional simulations, this type of segregation can be used in industrial applications for sorting.

Gas-solid flow simulations have been performed to study fluidized beds. Benchmark 2D fluidized bed simulations have been performed and the results have been shown to satisfactorily compare with those published in the literature. A comprehensive study of the effect of drag correlations on the simulation of fluidized beds has been performed. It has been found that nearly all the drag correlations studied make similar predictions of global quantities such as the time-dependent pressure drop, bubbling frequency and growth. But the local behavior predicted by different drag correlations is quite different and this may result in differences in the heat and mass transfer and hence the overall chemical conversion in the bed. Granular temperature differences in the bed predicted by various drag correlations have also been presented. In addition, binary mixture fluidized bed simulations have also been performed to delineate the effect of particle size. Substantial segregation is observed at the bed base in regions isolated from the inlet jet, for low superficial gas velocities.

In conclusion, discrete element simulation has been successfully coupled to continuum gas-phase. Though all the results presented in the thesis are two-dimensional, the present implementation is completely three dimensional and can be used to study 3D

fluidized beds to aid in better design and understanding. Other industrially important phenomena like particle coating, coal gasification etc., and applications in emerging areas such as nano-particle/fluid mixtures can also be studied through this type of simulation.

Acknowledgements

I sincerely thank my advisors, Dr. Jayathi Y. Murthy (School of Mechanical engineering, Purdue University) and Dr. Cristina Amon, who have helped me work in the area of my research interest in computational fluid dynamics and heat transfer. My sincere heartfelt thanks to Dr. Jayathi Y. Murthy for all her support and patient guidance throughout the period of my Masters and PhD work with her. Her training, advice and insight into things have been invaluable.

I would like to thank my thesis committee members, Dr. Kenji Shimada and Dr. Allen Robinson, for being on the committee and for their cooperation and suggestions.

I am indebted to my parents for everything they did for me; their generous support, motivation and trust in me since childhood, which helped me aim higher from time to time. Thanks to my sister and brother and their respective families for being a constant source of inspiration.

Thanks to the financial support from Department of Energy (DOE) and the use of the MFIX (Multiphase Flow with Interphase eXchanges) code, developed by Dr. Madhava Syamlal and his group at the National Energy Technology Labs (NETL). Thanks also to Dr. Thomas O'Brien of NETL.

Thanks to all my wonderful friends in CMU and Purdue for being there for me at all times. My gratitude goes to my music teacher and her family for the knowledge they have given me and for their valuable input in life. Thanks also to all my relatives whose confidence in me further encouraged my performance and betterment.

Last but not the least, my sincere thanks to all my teachers since childhood, who have been instrumental in installing knowledge and morals in me and in shaping me.

Table of Contents

List of Figures

List of Tables

Nomenclature

d : Particle diameter

e : Coefficient of restitution

g : Acceleration due to gravity

h/d : Non-dimensionalized particle bed height

k : Spring stiffness constant in soft-sphere model

m : Particle mass

$\vec{r}$: Particle position vector

C_{DS} : Single particle drag coefficient

D_m : Non-dimensionalized bed drag correlation for MFIX correlation

D_t : Non-dimensionalized bed drag correlation for Tsuji correlation

D_k : Non-dimensionalized bed drag correlation for other correlations like Wen &Yu

I : Moment of inertia of a particle

$\vec{F}$: Force vector

$\vec{F}_{Dgs}$: Drag force between the gas and solid phases

F_{gs} : Particle bed drag coefficient

Re : Reynolds number

U_g : Gas/fluid Velocity

U_g : Gas/fluid Velocity

V_g : Gas/fluid Velocity

V_g : Gas/fluid Velocity

ΔV : Fluid computational cell volume size

Greek Letters

Γ : Acceleration amplitude

$\vec{T}_c$: Torque force on the particle

δ : Particle-particle pr particle-wall overlap

ε_g : Volume fraction of fluid phase (void fraction)

ε_{sm} : Volume fraction of m^{th} solids phase

η : Damping coefficient in the soft-sphere model

ρ : Density

μ : Friction factor

$\vec{\omega}$: Angular velocity

Subscripts

f : Fluid

g : Gas/fluid

i, j : Index (of particle or computational cell)

m : Solid phase

n : Normal direction forces/overlaps

p : Particle

s : Solid

t : Tangential direction forces/overlaps

Chapter 1

Introduction

The flow of fluids of single phase has occupied the attention of scientists and engineers for many years. The equations for the motion and thermal properties of single-phase fluids are well-accepted and closed form solutions for specific cases are well-documented. The state of the art for multiphase flows is considerably more primitive in that the correct formulation of the governing equations is still under debate. For this reason, the study of multiphase flows represents a challenging and potentially fruitful area of endeavor. Hence there has been an increased research activity in the experimental and numerical study of multiphase flows. Multiphase flows can be broadly classified into four groups; gas-liquid, gas-solid, liquid-solid and three-phase flows. Gas-solid flows are usually considered to be a gas flow with suspended solid particles. This category includes pneumatic transport, bubbling/circulating fluidized beds and many others. In addition, there is also a great deal of industrial interest in pure granular flows in industrial equipment such as mixers, hoppers, ball mills, and chutes.

The focus of this thesis is the numerical simulation of granular and gas-solid flows. Generally, two different approaches may be taken to model the gas-solid flows (Crowe, Sommerfeld and Tsuji, 1998):

Continuum Approach: Here, the gas and the solid are treated as interpenetrating continua. Continuity and momentum equations are written for each phase, and interphase interaction is accounted for through appropriate sources and sinks in the phase momentum equations. This approach requires a constitutive equation for the solid phase

to relate the solids stress tensor to the velocity field; the fluid phase is typically modeled as Newtonian. The interphase interaction terms typically involve empirical relationships for drag, heat transfer and other exchanges.

Combined Continuum - Discrete Element Approach: Here the fluid phase is treated as before, assuming a continuum. The solid phase is not, however, treated as a continuum. Instead, the motion of individual particles is tracked using Newton's laws, accounting for collisions with other particles, with walls and the fluid-particle interaction forces. The hydrodynamic influence of the particles on the gas appears both as a volumetric blockage as well as an interphase drag. Other effects, such as interphase heat and mass transfer can also be accounted for in this approach.

The focus of this thesis is the computation of gas-solid flows in bubbling and circulating fluidized beds using discrete element simulation (DES) to represent the solid phase. In the rest of the chapter, we first review existing work in the simulation of granular flows, and then discuss gas-solid flow modeling. We then present the aims of the thesis, and describe its organization.

1.1. Modeling of Granular Flows

All simulations of gas-solid flows require the solution of the velocity and spatial distribution of the solid phase. The solid phase may be represented either as a continuum with constitutive relations to describe its stress-strain relationship, or as a conglomeration of discrete elements, as described above. A widely-used continuum approach is to develop a kinetic theory for the particulate phase similar to the kinetic theory of gases; theories of this type have been quite successful in the rapid granular regime, which is

dominated by inter-particle collision. A number of kinetic theories have been published, including those by Savage and Jeffrey (1981) for elastic spherical particles, Jenkins and Savage (1983) for spherical and nearly elastic particles, and Lun et al (3) for inelastic particles. The development of these kinetic theories mimics the kinetic theory of gases in that binary collision of particles are considered first, followed by statistical averaging. In contrast, a variety of continuum mixture theories exist based on continuum mechanics approaches. Here the objective is to formulate stress-strain relationships from fundamental requirements for coordinate and rotational invariance, postulated relationships between stress and strain or strain-rate etc. Examples of this class of theories may be found in the review by Massoudi and Boyle(1991)

An alternative to continuum theories is discrete element simulation (DES). Two types of theories are widely used in conjunction with DES. In the rapid granular regime, where collisional interactions dominate, the hard sphere model is used. Here, particle volume fractions are low enough that binary collisions may be assumed; collisions may also be modeled as instantaneous. Between collisions, particles travel in straight lines; particle trajectories change only at collision. In contrast, dense granular flows are best modeled using the soft sphere model (Cundall and Strack, 1979). Here, a particle is assumed in enduring contact with several particles over extended periods of time. The interaction force is typically modeled using a spring-mass-dashpot type of model for normal and tangential forces. A detailed description of this type of model is given in Chapter 2.

Other experimental, theoretical and numerical works done in studying pure granular material are presented in Chapter 3.

1.2. Modeling of Gas-Solid Flows

Theoretical, experimental and numerical studies are being conducted by various research groups to understand the gas-solid flow dynamics. A good overview of work in this area may be found in Crowe, Sommerfeld and Tsuji (1998). Hydrodynamic modeling of gas-solid flows has been undertaken in one form or another for over forty years now. Pritchett et al (1978) simulated a 2D fluidized bed using the two-fluid model and showed the formation of bubbles in fluidized bed. Bouillard (1989) used a two fluid model to investigate a fluidized bed with any solid blockages inside the bed. There are a number of other studies using this approach. Detamore et al (2001) have performed an analysis of scale-up of circulating fluidized beds using kinetic theory. Significant contributions to the modeling of gas-solid flows are made by Gidaspow and co-workers (Ding et al, 1990) who combined kinetic theory for the granular phase with continuum representations for the gas phase.

Glasser et al (1995, 1997, 1998) have performed theoretical studies and computed the solutions for one-dimensional and two-dimensional traveling wave solutions for the equations of motion for gas and particles in a fluidized bed. They used the Newtonian model for the solid stress tensor. They found that the solutions for fully developed two-dimensional waves capture the bubble phenomenon in fluidized beds. In fluidized beds regions of high and low particle concentration are seen to form intermittantly. The regions of low particle concentration are known as bubbles and those of high particle concentration are called clusters. They have also proposed a non-dimensional number whose value indicates whether bubbles form or not. This non-dimensional value depends

on the density of the particles, the terminal settling velocity of a particle, gravity and particle phase viscosity.

Cluster formation is one of the important phenomena in gas-solid flows. The frequency of inter-particle collision is high in regions of the bed where the particle density increases due to fluctuation. Since the collisions are assumed inelastic the granular temperature decreases and so does the solids pressure. As a result more particles migrate into this region, further increasing the density and resulting in cluster formation (Goldhirsch and Zanetti, 1993). They have proposed a mechanism for clustering instability and have also developed a formula for characteristic inter-cluster distance.

Dasgupta et al (1994, 1998) have developed model for gas-particle flow in a vertical channel. For the solid stress tensor they used the Newtonian model. In such flows, when the particle number increases, the inertial and viscous effects are dominated by the inter-particle collisions. Srivastava et al (1998) have experimentally studied gas-solid flows in a circulating fluidized bed (CFB) under both stable and unstable operating conditions, by using electrical capacitance tomography to obtain particle distribution at various cross sections.

More recently, combinations of DES and gas-phase continuum simulations have begun to appear in the literature. In one of the earliest works in this area, Tsuji et al (1992) used the soft sphere model and modified it slightly to simulate the gas-solid flow in a horizontal pipe with particles of 10 mm diameter. They captured the formation of plugs. They have correlated the plug flow velocity and the height of the stationary deposited layer. They reported that the time-step limit proposed by Cundall and Strack (1979) resulted in instability in their calculations and proposed to calculate the time-step from

the characteristic frequency of a one-dimensional vibration system involving a particle of simulation. Nakanishi et al (1991) describe the use of DES to perform gas-solid flow simulations for a discharge bin. They used DEM for solid phase and a continuum description for the gas phase and discuss the advantages of air jets on the walls of the discharge. The air jets push the particles off the walls and force them to exit. Tsuji et al (1993) have also simulated a two-dimensional fluidized bed using a DES soft sphere model. They could capture reasonably the formation of bubbles, slugs and particle mixing as observed in experiments. Rhodes et al (2001) performed a discrete element simulation of a fluidized bed and captured cohesion behavior characterized by lumping of particles and the formation of fixed structures, among others. Xu and Yu (1997) have combined DES and CFD to simulate the gas-solid flow in a fluidized bed. Popken et al (1999) compared kinetic theory and discrete element schemes for modeling granular Couette flows. They have reported that the two methods give similar results both qualitatively and quantitatively. Tsuji et al (2003) have also simulated a two-dimensional fluidized bed using DES soft sphere model. They studied the effects of particle size and particle density in a fluidized bed and found that better mixing occurs for beds where the particle sizes are closer to each other and also when there is little density difference. Li and Kuipers (2003) have studied the effect of various drag correlations on the flow structures formed in fluidized beds and report that correlations with non-linear dependence on the void fraction exhibit clusters with finer length scales. They have also reported the effects of inter-particle inelastic collisions. Tanaka et al (1996) have reported conditions for mixing and segregation.

These combined DES and gas-phase simulations all assume that the gas-phase control volumes over which computations are done contain many hundreds of particles. Thus, they do not resolve the flow around individual particles. Instead, the interphase drag is taken from experimental correlations. Over the last few years, a few studies have been published which try to represent the flow over individual particles directly without recourse to experiments (Patankar et al, 2001; Pan et al, 2001; Joseph et al, 2001. However, these are extremely time-consuming and require frequent re-meshing, and only a few hundred particles may be simulated for short time scales.

1.3. Scope of the Thesis

The present work involves developing efficient DES methods for dense granular flow and coupling this simulation to continuum simulations of the gas phase flow. The resulting solver is to be applied to detailed simulation of canonical flows relevant to bubbling and circulating fluidized beds. The specific objectives of the proposed work are:

1. To develop a DES capability for spherical particles of variable diameter. A soft sphere model is used.
2. To develop efficient search algorithms and data structures for computing inter-particle interaction.
3. To test the developed capability for pure granular flows to demonstrate the validity of the formulation and its implementation.
4. To couple the discrete element simulation with a simulation capability for the gas phase. The implementation will allow for several particulate

phases characterized by particle size. The coupled solution methodology is implemented in NETL's MFIX code, described in the appendix.

5. Apply the coupled gas-solid flow capability to the investigation of the detailed physics of fluidized beds. Of particular interest is the investigation of particle density and particle size effects.
6. Study the effect of the various drag correlations (published in literature) on the simulation results.

The following work has been completed: A soft-sphere model has been implemented. Two different search algorithms, No-binary Search (NBS), and Quadtree/Octree search, have been implemented. The former provides an O(N) search procedure for like-sized particles. The latter is an O(NlogN) procedure, but can admit particles of different sizes. Simulations have been performed to observe pure granular behavior in vibrating beds. The results obtained match those in published literature. Various interesting behaviors like heaping, round and cusp surface standing waves and kinks have been observed for different values of the acceleration parameter. Kink formation in granular beds with binary particle size distribution has been studied and horizontal segregation has been reported.

Coupling of DES and gas/liquid flow has been done. The fluid flow computation has been done using MFIX, a solver developed for multiphase flows. In order to complete the coupled calculations, the void fraction corresponding to the DES particle distribution is computed. Interphase drag is computed from experimental correlations. Finally, a segregated coupling algorithm for the fluid and solid is used, with several DES time steps

constituting one fluid time step. 2D computations of gas-solid flows in fluidized beds have been performed. Binary mixture fluidized beds have also been simulated. Effects of the drag correlations on the simulation results have also been studied.

A more detailed description of the discrete element simulation (DES) is described in Chapter 2. The hard sphere model and the soft sphere model are explained. The soft sphere model is dealt with in detail since it forms the basis of the work done here. Various important factors such as the determination of the spring stiffness constant and the damping coefficient are described. A procedure to compute the forward time step is explained. Efficient search algorithms are presented.

In Chapter 3. the results obtained for pure granular material simulations using DES are presented. Two-dimensional vibrated granular beds have been simulated and the results obtained are presented. Phenomena observed in vibrated granular beds, such as heaping, round and cusp surface waves and kink formation, have been produced by simulations and presented. The results are satisfactory compare well with published experiments and existing benchmark simulations. Kink formation in granular beds with binary mixures with varying particle sizes and density distribution has been simulated and horizontal segregation is reported.

The gas-solid flow simulation method employed in the present work is reported in Chapter 4. An efficient and effective gas-solid coupling is the key to good simulation. The gas side continuum theory is explained. The segregated coupling method used to couple the DES computation with the continuum gas data is explained. Multiple solid time steps are employed for a single fluid time step. Information associated with the solid, such as the volume fraction in each fluid cell, the averaged solid velocity and the

like, are computed and fed into the MFIX continuum solver. The drag and buoyancy interactions between the gas and solid are then computed. The granular temperature is computed to provide data to modelers developing continuum theories. Various drag correlations that are used to compute the drag exerted by the gas and solid phases on each other are discussed and compared. The method is validated by comparison with published experimental/simulations of benchmark cases including flow in a particle-laden driven cavity and gas-solid flow in a fluidized bed (Tsuji 1993, 1996, 2003; Xu and Yu, 1997; Kuipers 2003). The results match published results reasonably well. A Driven cavity simulation is also performed for validation.

In Chapter 5, application and results of the model are discussed. Since empirical drag correlations are used to couple fluid and solid, it is important to quantify the effect of different empirical drag correlations on the solution. Fluidized simulations for some widely used drag correlations have been performed. It is shown that though the broad bed behavior, like the pressure drop and bubble formation frequency do not alter much with the drag correlation used, local information such as the void fraction distribution in the bed is affected substantially by different drag correlations. This points to the need to develop a better experimental and theoretical understanding of gas-particle drag in fluidized beds. Granular temperature variations, volume fraction variations and other details are studied. Fluidized beds with binary particle mixtures are also simulated and segregation/mixing studied.

Finally, Chapter 6 summarizes the contributions of the thesis and makes recommendations for future work.

Chapter 2

Discrete Element Simulation

Particle-particle collision is negligible in dilute gas-particle flows. As the particle concentration becomes higher, particles collide with each other and the loss of particle kinetic energy due to inter-particle collision cannot be neglected. Thus inter-particle interaction becomes important in wall-dominated dilute flows as well as in dense particle flows. Since from a macroscopic viewpoint, the solid phase in a fluidized bed behaves like a kind of fluid, most researchers in the early ’70s assumed the solid phase to be a continuum and modeled a granular flow as a two-fluid flow problem. In analyzing systems for which the Bagnold number *Ba* is greater than 40 and less than 450, particle-particle interactions and particle-fluid interactions must both be taken into account and when *Ba* is greater than 450 the system is dominated by particle-particle interactions. DES is well suited to yield detailed data on the behavior of the granular component of these flows. In DES the system is assumed to consist of individual particles and the whole system is analyzed by analyzing each particle individually. Apart from the earlier theories like Monte-Carlo simulation, which is a statistically based DES method, today two models which explicitly consider the particulate nature of granular materials and the particulate interactions are widely used for DES. They are the *hard sphere model* and the *soft sphere model*. The detailed algorithm for gas-solid coupling is discussed later. The following sections explain the hard-sphere and soft-sphere models for particle-particle and particle-wall interactions. In the present work the soft-sphere model has been used.

Hence it will be dealt with in detail. Other details of the simulation, such as the search techniques for nearest neighbors, are also described.

2.1. Hard Sphere Model

In dilute gas-solid flows where the particulate phase is quite disperse, the inter-particle collisions are analogous to molecular dynamics in rarefied gases. Though the particle collisions are inelastic, energy is re-supplied to the system through particle acceleration, gravity, or through collision with a moving boundary. Most published literature has considered only binary collisions for rapid granular flow regimes. Particles move in well-defined trajectories until collision with another particle occurs. These interactions are modeled as instantaneous collisions and the post-collision state of the particles is determined from classical dynamics (Campbell, 1982). The hard sphere model considers the Newtonian equations of motion in the integral form and is based on the impulsive force which is defined by the integral of the forces acting on a particle versus time, as seen in Figure 2.1. The equations and detailed description of hard sphere model can be found in Campbell (1982) and Crowe et al (1998).

2.2. Soft Sphere Model

Most of the commonly observed gas-solid flows are dense particle flows and exhibit multiple-particle long-duration contacts. The soft sphere model, proposed by Cundall and Strack (1979) is the most applicable in such regimes. Though the soft sphere model requires more computational power than the hard sphere model, some information like the inter-particle force information obtained in the model cannot be

obtained in the hard sphere model. Also the hard sphere model breaks down in systems with long inter-particle contact durations.

2.2.1. Particle-Particle Interaction

The soft sphere model starts with the differential equations and the variations in momentum and displacement are obtained for arbitrary times as solutions to differential equations. The forces acting on each particle in the system are calculated. Using Newton's second law, the acceleration of each particle is calculated. Then, by integrating the acceleration in time, new particle states are calculated in terms of the velocity and position. When two elastic particles collide in reality, they deform. The soft sphere model assumes an overlap displacement δ as shown in Figure 2.2., instead of considering the actual deformation.

The inter-particle contact forces, namely, the normal, damping and sliding forces, act on the two particles and are modeled in the soft sphere model using mechanical elements like springs, dash-pots, sliders etc, as shown in Figure 2.3. The normal contact between two particles is modeled as a linear spring in parallel with a dashpot element. The spring provides an elastic restoration force while the dashpot dissipates energy during contact. As a result the effective coefficient of restitution is less than one. The tangential contact model is slightly more complex. In the tangential model the spring is in series with Coulombic friction sliding element. The spring allows the particle to respond elastically, while the sliding friction element allows particles to slide against each other. The magnitude of tangential force is limited by the sliding element.

The effect of these mechanical elements on particle motion appear through the spring stiffness constant k, the damping coefficient η, and the friction coefficient μ_f. Both translational and rotational motion is considered. The translational motion is caused by contact force, interaction forces with the fluid and gravitational force. Only contact forces are considered to cause rotational motion. From Newton's second law, the translational and rotational accelerations are given by

$$\ddot{\vec{r}} = \frac{\vec{F}}{m} + \vec{g}$$

$$\dot{\vec{\omega}} = \frac{\vec{T}_C}{I}$$

where $\vec{r}$ is the position vector of the particle center of gravity, m is the particle mass, $\vec{F}$ is the total force acting on the particle, $\vec{g}$ is the gravity vector, $\vec{\omega}$ is the rotational velocity, $\vec{T}_C$ is the total torque caused by contact forces, I is the moment of inertia ($=\frac{2}{5}ma^2$ for a sphere of radius a). ($\dot{}$) denotes the time derivative.

The contact force can be written as:

$$\vec{F}_C = \vec{f}_C + \vec{f}_D$$

where $\vec{f}_C$ is the total force on the particle due to inter-particle contact and $\vec{f}_D$ is the force on the particle due to fluid drag and pressure gradient.

From the spring-damper model, when particle i is in contact with particle j, the normal component of the contact force, $\vec{f}_{Cnij}$, acting on the particle i is given by the sum of forces due to the spring and dash-pot. Figure 2.4. shows the sign convention.

$$\vec{f}_{Cnij} = -k\vec{\delta}_{nij} - \eta\vec{v}_{nij}$$

where δ_{nij} is the particle displacement caused by the normal force, $\vec{v}_{nij}$ is the normal component of the relative velocity and is given by $\vec{v}_{nij} = \vec{v}_{rij} \cdot \vec{n}_{ij}$, where $\vec{v}_{rij}$ is the velocity vector of particle *i* with respect to particle *j* and $\vec{n}_{ij}$ is the normal vector between them.

$$n_{ij} = \frac{\vec{x}_j - \vec{x}_i}{\left|\vec{x}_j - \vec{x}_i\right|}$$

δ_{nij} is the normal overlap and is the distance traveled by the particle pair with the normal component of the relative velocity in the given time step. The total overlap at a given time is the accumulation of the overlaps since the particles came into contact

$$\vec{\delta}_{nij} = \vec{v}_{nij}\Delta t$$

It may also be computed directly as the difference between the sum of the radii and the center to center distance $\delta_{nij} = (r_i + r_j) - \left|\vec{x}_i - \vec{x}_j\right|$

The tangential component of the contact force $\vec{f}_{Ctij}$, is given by

$$\vec{f}_{Ctij} = -k\vec{\delta}_{tij} - \eta\vec{v}_{sij}$$

where δ_{tij} is the displacement in tangential direction. The suffixes *n* ad *t* imply normal and tangential respectively. The slip velocity $\vec{v}_{sij}$ is given by

$$\vec{v}_{sij} = \vec{v}_{rij} - \vec{v}_{nij} + r\left(\vec{\omega}_i + \vec{\omega}_j\right) \times \vec{n}_{ij}$$

where *r* is the radius of the particle. Also

$$\left|\vec{f}_{Ctij}\right| \le \mu_f \left|\vec{f}_{Cnij}\right|$$

Finally the total contact forces on a particle *i* due to its neighbors *j* is the summation of forces due to individual neighbor pairs.

$$\vec{f}_{Ci} = \sum_j \left(\vec{f}_{Cnij} + \vec{f}_{Ctij} \right)$$

$$\vec{T}_{Ci} = \sum_j \left(r\vec{n}_{ij} \times \vec{f}_{Ctij} \right)$$

2.2.2. Particle-Wall Interaction

The particle-wall pair is dealt just as a pair of particles, but with a few modifications. All the equations mentioned earlier hold when the neighbor particle j in the above equations is replaced by wall. In this case,

$$\left|\vec{v}_j\right| = \left|\vec{\omega}_j\right| = 0$$

Though in terms of equations a particle-wall pair is treated just as a particle-particle pair, the complexity increases in the way one treats the wall itself. There are a few ideas regarding this. One such idea is to treat the wall as a reflecting body. So when a particle comes in contact with the wall it is reflected but the velocity is altered by taking into account the coefficient of restitution, as seen in Figure 2.5. If there were no wall, the particle traveling with initial velocity v_p^o would have crossed the domain and traveled a distance $v_p^o \Delta t$. But when the wall is treated as a reflecting body, the particle still travels a distance $v_p^o \Delta t$ but would remain inside the domain. The time Δt_1, taken to reach the wall is calculated and the particle is placed inside the domain at a distance $v_p^o \left(\Delta t - \Delta t_1\right)$. And when the coefficient of restitution e is to be accounted for, the velocity of the particle

after contact with the wall would be $v_p^1 = v_p^o.e$ And hence the particle would be placed at $v_p^1(\Delta t - \Delta t_1)$ and the total distance traveled would be $v_p^o \Delta t_1 + v_p^1(\Delta t - \Delta t_1)$. Wall movement and other factors can be incorporated by vector manipulation.

Another way is to replace the neighbor *j* with the wall. In this case the wall is treated as a particle with infinite radius. Thus the normal between any particle and the wall would always be the normal to the wall itself. In practice one can only declare a big number to represent infinity. A better way of ensuring that the normal of the particle-wall pair is normal to the wall is to dynamically declare a particle of the same size as that of particle *i* whenever it comes in contact with the wall. The new particle has the same translational velocity as that of the wall and its position is such that it is a radius away from the wall, outside the particle bed domain and mirroring the particle (see Figure 2.6). Since its position and velocity are fixed, the wall particle effectively acts as a boundary condition. The normal between the particle and the wall particle is same as the normal to the wall.

Another situation of interest is periodic boundaries. Periodic boundaries are necessary when simulating large particle systems. Instead of simulating the whole system, only a repeating module in the system is identified and simulated. Periodicity is imposed by allowing the particles crossing over a boundary to be introduced into the system at the opposite boundary. In this case the particles close to the periodic boundary are identified at each time step and particles with the same velocity and properties are declared on the opposite periodic boundary and outside the particle bed domain. This procedure enables the particles at a periodic boundary and inside the particle bed domain

to see the particles at the other periodic boundary, thus behaving as they would in a large system.

Let a one-dimensional periodic domain of length L be considered. If a particle is close to x=L, then in a periodic case it should feel the influence of neighbor particles close to x=0. Hence at every time step the particles close to x=0 (i.e., say within one or two diameters distance from x=0) are identified and positioned at x=L such that a particle of position x_i at distance *i* and within a diameter distance from x=0 is reproduced as x_{i+L} such that it is at a distance *i* from x=L. That way all particles between x=0 and x=L , which are close to x=L will see their complete neighbor list for force calculations. If a particle $x_{L+\delta}$ crosses x=L then it is introduced into the domain at x=0 by changing its position to x_δ . A similar process is performed for particles near the x=0 region.

2.2.3. Determination of Key Parameters

An important issue in the soft sphere model is the determination of key parameters such as the spring stiffness constant *k* and the damping coefficient η. Numerical parameters such as the time step Δt are determined from these values.

The spring stiffness k is deduced from Hertzian contact theory. According to the Hertzian contact theory, the relation between the normal force F_n and normal displacement δ_n is given by

$$F_n = \delta_n^{3/2}$$

In case of two spheres of the same radius *r*,

$$k_n = \frac{\sqrt{2r}E_s}{3\left(1-\sigma_s^2\right)}$$

where E_s is Young's modulus for the solid and σ_s its Poisson's ratio. In case of the particle-wall contact the normal stiffness constant is given by

$$k_n = \frac{\frac{4\sqrt{r}}{3}}{\frac{1-\sigma_s^2}{E_s}+\frac{1-\sigma_w^2}{E_w}}$$

where E_w is Young's modulus and σ_w the Poisson's ratio for the wall. The tangential force and the tangential displacement are related as

$$F_t = \frac{2\sqrt{2r}G_s}{2-\sigma_s}\delta_n^{1/2}\delta_t$$

where G_s is the shear modulus and is related to E_s by

$$G_s = \frac{E_s}{2(1+\sigma_s)}$$

Thus, for contact between two particles, k_t is given by

$$k_t = \frac{2\sqrt{2r}G_s}{2-\sigma_s}\delta_{nij}^{1/2}$$

and for contact between a particle and wall

$$k_t = \frac{8\sqrt{r}G_s}{2-\sigma_s}\delta_{nij}^{1/2}$$

When physical properties such as Young's modulus and Poisson's ratio are known. Cundall and Strack (1979) proposed that the damping coefficient η be calculated using $\eta = 2\sqrt{mk}$. Tsuji et al. (1992) showed that the damping coefficient for a nonlinear

spring is numerically related to the coefficient of restitution as $\eta = \alpha\sqrt{mK}\,\delta^{1/4}$ where α is a constant related to the coefficient of restitution *e*. The coefficient of restitution *e* is defined as the ratio of particle velocities before and after the collision. For a system of particles *e* is a fixed constant

$$e = -\frac{v}{v_0}$$

The equation of motion for a spring dashpot model is $m\ddot{x} + \eta\dot{x} + kx = 0$

Under given initial conditions of $x = 0; \dot{x} = v_i$ at *t*=0 is given by

$$x = \frac{v_i}{q}\sin(qt)\exp(-\gamma\omega_o t)$$

$$\dot{x} = \frac{v_i}{q}\exp(-\gamma\omega_o t)\{q\cos(qt) - \gamma\omega_o \sin(qt)\}$$

where

$$\omega_o = \sqrt{k/m}$$

$$\gamma = \frac{\eta}{2\sqrt{mk}}$$

$$q = \omega_o\sqrt{1-\gamma^2}$$

The oscillation period is $2\pi/q$. A particle colliding with another particle at time t=0 detaches itself at time t=π/q. The velocity when it detaches is

$$v_o = -v_i \exp(\gamma\omega_o \pi/q)$$

Therefore

$$e = -\frac{v_o}{v_i} = \exp(-\gamma\omega_o \pi/q)$$

Hence for a fixed value of coefficient of restitution (Tsuji et al, 1993)

$$\eta = 2\gamma\sqrt{mk}$$

$$\gamma = \frac{\alpha}{1+\alpha^2}$$

$$\alpha = \frac{1}{\pi}\ln\left(\frac{1}{e}\right)$$

These parameters are important in determining the time step Δt for numerical integration. Because contact forces can only be determined after determining which particles are in contact, explicit time stepping methods are necessary. Explicit schemes impose a limit on the time step due to stability considerations. Smaller time steps ensure greater stability but one should choose a suitable time step so that the computational time is optimized. Cundall and Strack (1979) suggested that a time step be chosen such that

$$\Delta t \lhd 2\sqrt{\frac{m}{k}}$$

However Tsuji et al (1992) report that the above criterion resulted in instability and proposed that the time step be chosen depending on the system frequency. They chose a spring mass system with the mass of a particle in the granular flow and the chosen spring stiffness constant. The value of the time step is kept smaller than the frequency of the system. Another way is to choose the time step such that the highest frequency of the system could be integrated accurately (Wassgren, 1996). The smaller of the translational and rotational periods of oscillation is chosen. For a 2D problem the maximum number of non-overlapping neighbors any particle can have is six. The translational period of a particle with six neighbors is

$$\tau_{trans} = 2\pi\sqrt{\frac{m}{6k}}$$

and the rotational period is given by

$$\tau_{rot} = 2\pi\sqrt{\frac{I}{6kr^2}}$$

It can be shown that $\tau_{rot} \lhd \tau_{trans}$ and the time step is chosen to be one-tenth of τ_{rot}.

An explicit scheme is used in numerical simulations of above models. The new values of translational and rotational velocities and the new position of a particle are calculated from the old values.

$$\vec{v}_{new} = \vec{v}_{old} + \ddot{\vec{r}}_{old}\,\Delta t$$

$$\vec{r}_{new} = \vec{r}_{old} + \vec{v}_{new}\Delta t$$

$$\vec{\omega}_{new} = \vec{\omega}_{old} + \dot{\vec{\omega}}_{old}\,\Delta t$$

It is important to note that the neighbor list for each particle is necessary at every time step to compute the contact force. This is one of the most time consuming processes in DES using the soft sphere model. Faster search algorithms are key to reducing the overall computational time.

2.3. Search Algorithms

2.3.1. N^2 Search:

This is the most easy search algorithm to implement. In this process, neighbors are found by calculating the distance between the particle of interest and every other particle in the system. Such a search has an operation count of $O(N^2)$, where N is the number of particles, and is extremely expensive for large-scale simulations. Some useful

alternate search techniques have been explored, of which the most significant are presented here.

2.3.2. Quadtree and Octree Search

The concepts of quadtrees (2D) and their 3D counterparts, octrees, is not new in the field of geometric modeling. The concept of quadtrees (octrees) is a hierarchical data structure that recursively subdivides a cubic volume into four (eight) smaller cubes called quadrants (octants) respectively until a decomposition criterion is met. This decomposition process is often presented as a tree of out-degree four (eight) respectively. The idea is to divide the plane more efficiently into regions of a maximum desired resolution. In short quadtrees and octrees are hierarchical variants of efficient spatial occupancy enumeration.

Typically, to store data, the domain is meshed into a number of boxes of equal size and the data in each such box is stored. As opposed to such standard methods of dividing the plane and distributing the data using the grid, which results in unnecessary storage of redundant data, quadtrees are a more efficient method for storing as well as processing operations. Figure 2.7 shows a pictorial comparison of a standard mesh and a quadtree. Quadtrees have been used extensively for two and three dimensional grid generators, though their role there is only to define the objects to be meshed. Presently quadtrees are being used not only for defining the objects to be meshed, but also to provide an O(NlogN) search algorithm for arbitrary point distributions.

A good description of the octree search procedures is given in Lohner(1998). In this type of search, particles are first arranged in quads which are then searched for

neighbors. An array LQUAD(1:7, MQUAD) is defined to store the particles. Here MQUAD denotes the maximum number of quads allowed. For each quad IQ, we store in LQUAD(1:7, IQ) the following information.

LQUAD(7,IQ): < 0 - the quad is full

= 0 - the quad is empty

>0 (<4) – number of particles in the quad

LQUAD(6,IQ): > 0 - the parent quad the present quad came from

LQUAD(5,IQ) : > 0 – the position of the present quad in its parent quad

LQUAD(1:4, IQ) : for LQUAD(7,IQ)>0 – the points stored in the quad

for LQUAD(7,IQ)<0 – the quads into which the present quad is subdivided

In each quad a maximum of 4 particles are stored. The quad in which the particles lie is known as their parent quad. If a fifth particle falls into a quad, then the quad is divided into four sub-quads (known as the children quads) and the old particles are relocated into their respective new children quads. Then the fifth particle is introduced into the new quad it falls in. If the quad is full again the division of the parent quad into 4 child quads is repeated until a vacant storage space is found. The process is performed such that no quad has more than 4 particles. The next step after allotting all the particles into their respective quads is to search for neighbors for a particle. In order to find the neighbors for a given particles a search region is created around the particles such that the particles falling in the search region contain all the neighbors of the particle of interest. In order to find the particles that fall in the search region, the levels of the quadtree are traversed, eliminating at the highest possible level all quads that lie outside the search

region. Once the quads that overlap with the search region are identified the particles in those quads are searched for the neighbors of the particle of interest (See Figure 2.8). Lohner (1998) shows the schematic of the process. It is not difficult to see that a quadtree is an $O(N\log_4 N)$ search algorithm and analogously an octree is an $O(N\log_8 N)$ search algorithm, where N is the number of particles. For octree, the array structure would be

LQUAD(1:11, MQUAD) to store these particles, parent quad and other information

LQUAD(11, IQ): < 0: the octant is full

= 0: the octant is empty

> 0: the number of particles stored in the octant

LQUAD(10, IQ): > 0: the octant the present octant came from

LQUAD(9, IQ): > 0: the position (1-8) in the octant the present octant came from

LQUAD(1:8, IQ): for LQUAD(11, IQ)> 0: the particles stored in this octant

for LQUAD(11, IQ)< 0: the octant s into which the present octant was subdivided

2.3.3. No-Binary Search

No-Binary Search (NBS) algorithm is proposed by Munjiza and Andrews (1998). As the name suggests, the NBS algorithm does not involve a binary search at any stage. The algorithm is an O(N) search. The performance of this algorithm is not influenced by packaging density, while memory requirements are insignificant. The major limitation of the algorithm is its applicability to only systems comprising bodies of similar size. The computational domain is first discretized into cells such that only one particle fits in a cell. Then the particles are all assorted into their respective integerized x, y or z zones

using linked lists. To find the neighbors of a particle, its integerized x, y and z coordinates, represented by ix, iy and iz respectively, are found; these indicate the cell into which the particle falls. Then, only particles whose integerized coordinates are neighbors of ix, iy and iz i.e., particles of the linked lists representing integerized coordinates ix-1, ix, ix+1, iy-1, iy, iy+1, iz-1, iz and iz+1 are searched for contact and the neighbors are determined. In 2D to find the neighbors of a particle corresponding to (ix, iy) only the cells (ix-1, iy), (ix-1, iy-1), (ix, iy-1) and (ix+1, iy-1) need to be searched to avoid repeating calculations. Figure 2.9 shows the concept of integerization based on the particle coordinates and the neighbor search cells.

Figures 2.10, 2.11, 2.12 and 2.13 show the results of a study done to compare the various algorithms discussed above. Figures 2.10, 2.11 and 2.12 compare the N^2, quadtree, and NBS algorithms for a 2D case for particles numbering from 10 to 10^5. Figure 2.13 shows the comparison of N^2, octree and NBS algorithms for a 3D case for particles numbering from 10 to 10^5. It can be seen that octree, quadtree and NBS algorithms are orders of magnitude faster than the conventional N^2 search algorithm. The NBS algorithm appears to be faster than octree or quadtree because of the factor of log N. But since NBS is applicable only to systems of almost equal-sized particles, developers of general purpose DES implementations may wish to use quadtree or octree search algorithms. It can be seen that for systems of 10^3 particles or less, the N^2 search is faster than quadtree or octree searches. This is because of the absence of the data sorting step before neighbor searching.

2.4 Closure

In this chapter, we have described the basic physical model governing soft-sphere discrete element models. These are seen to consist of a spring/mass/dashpot model for the contact forces between particles. An explicit algorithm for the integration of Newton's law is used, with the forward step being limited by the spring time constant. Neighbor searching consumes a large percentage of the computational time. Three different search algorithms are compared, and the NBS and quadtree/octree techniques are found to perform best for large particle assemblies. In the next chapter, we apply DES to the simulation granular flows in vibrated beds.

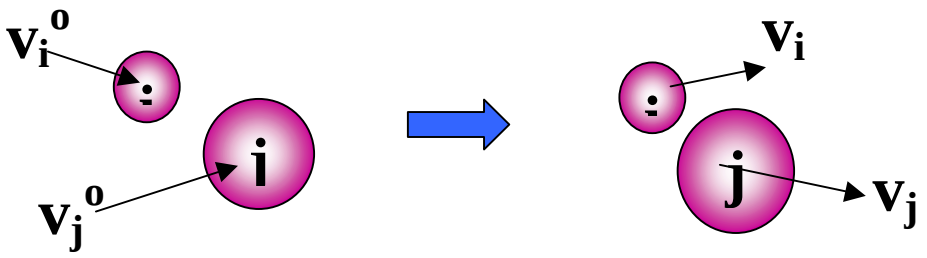

Figure 2.1. Particle-particle collision in a hard sphere model

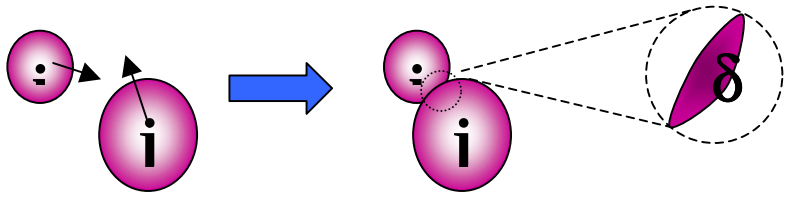

Figure 2.2. Particle-particle collision in a soft sphere model

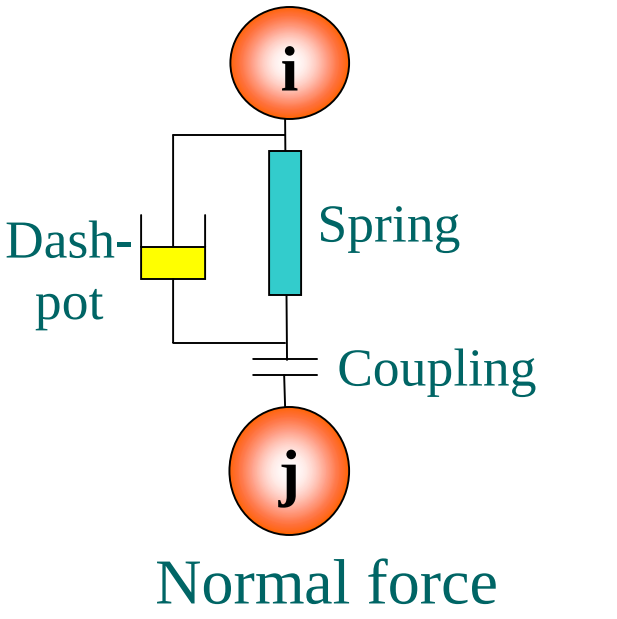

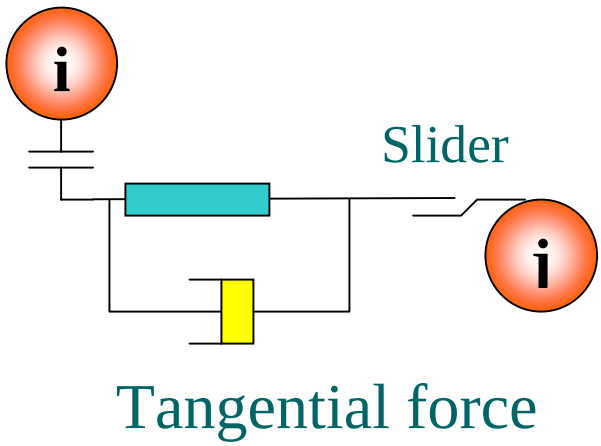

Figure 2.3. Spring-damper system to model contact forces

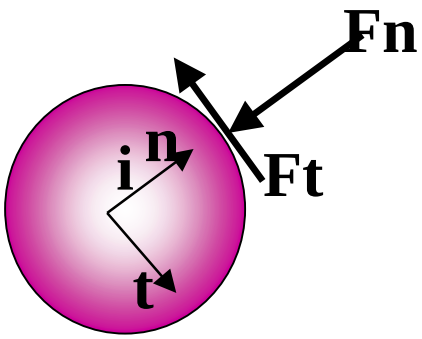

Figure 2.4. Sign convention for normal force F_n and tangential force F_t

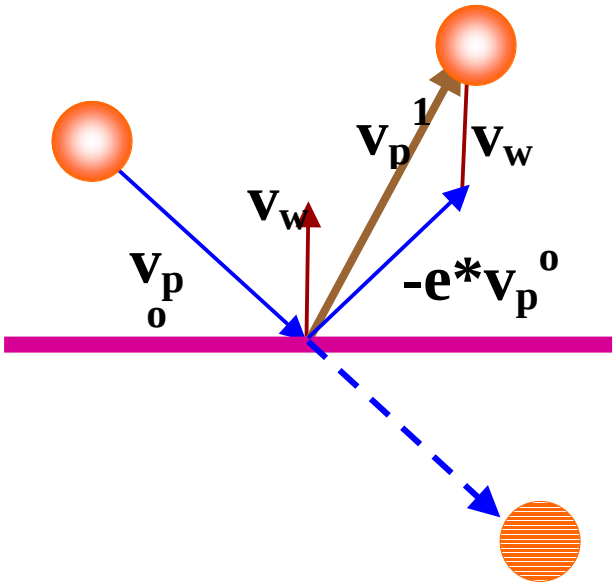

Figure 2.5. Particle-wall interaction: particle reflected on contact

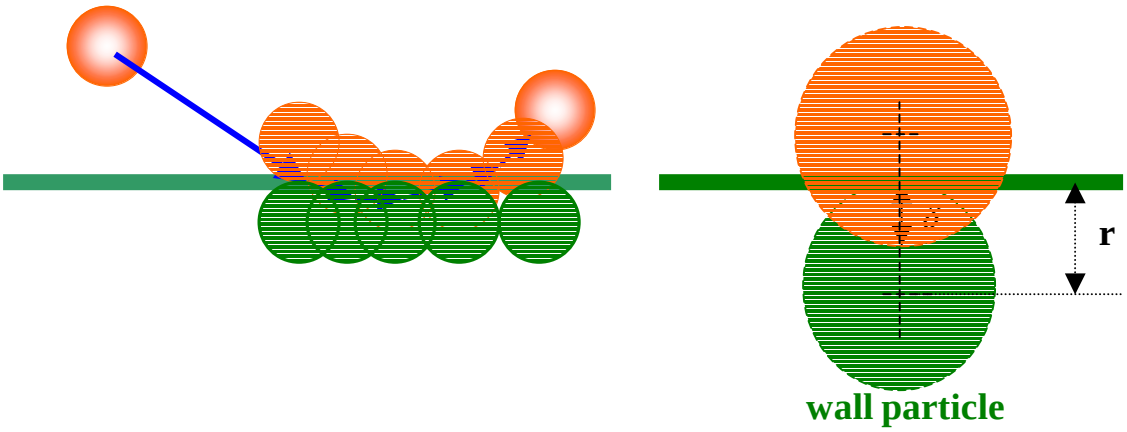

Figure 2.6. Particle-wall interaction; treating the wall as a particle of finite radius

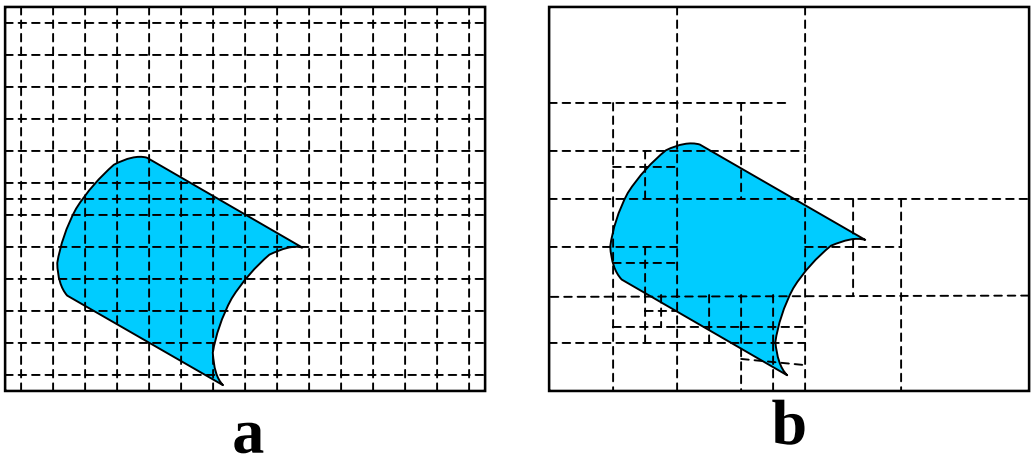

Figure 2.7. (a) Standard mesh versus (b) Quadtree

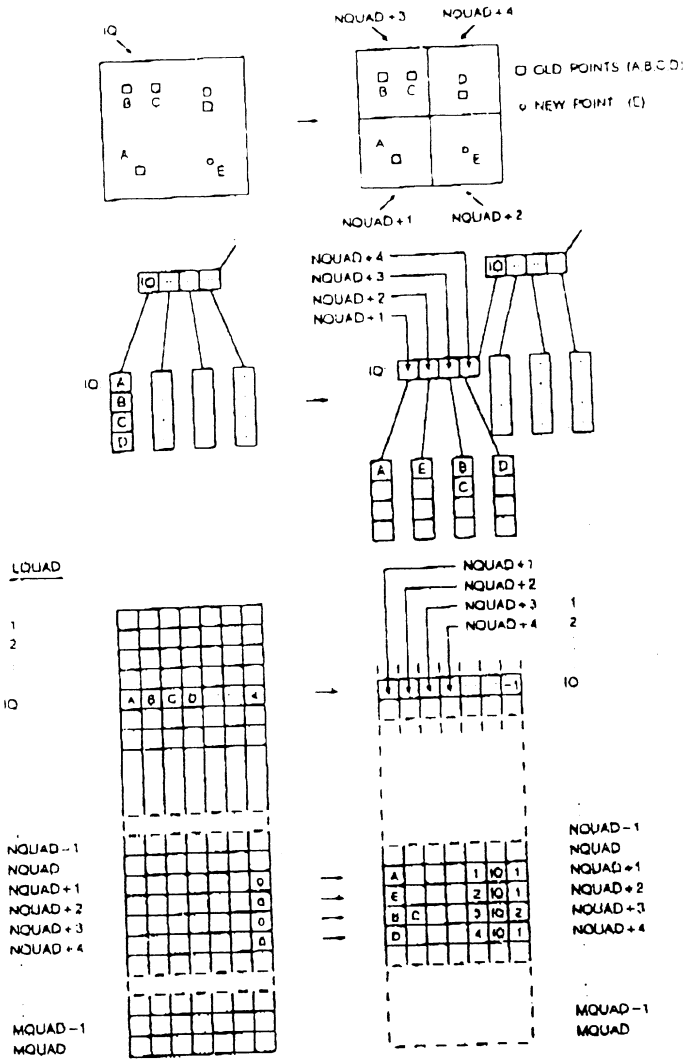

Figure 2.8. Schematic representation of the Quadtree algorithm (from Lohner, 1998)

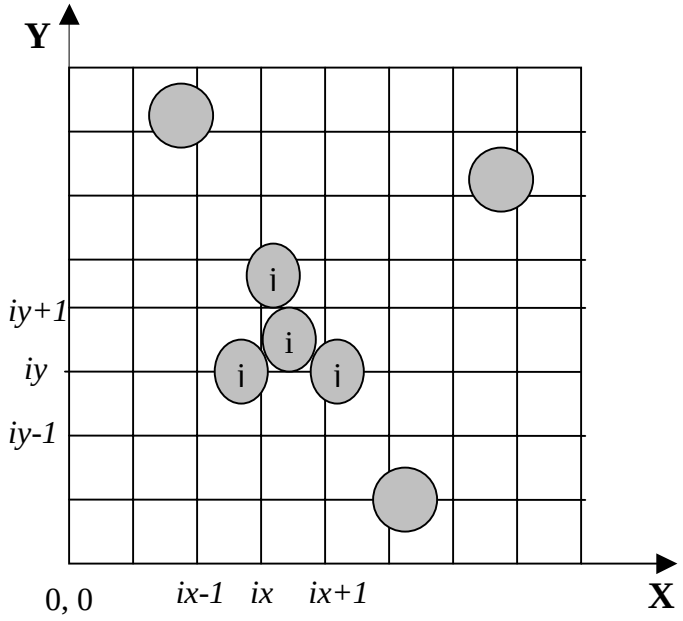

(a)

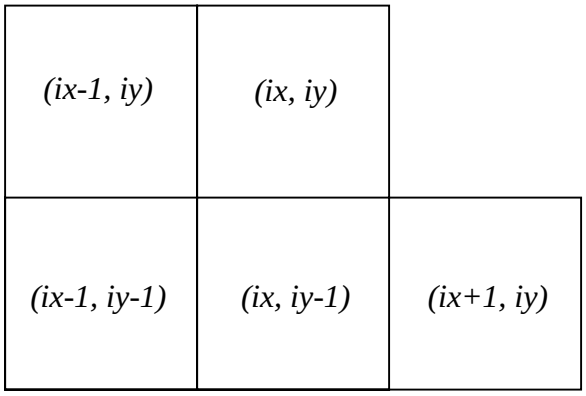

(b)

Figure 2.9. Representation of NBS algorithm for 2D case (a) Integerized coordinates and NBS mesh with each cell of size that of the particle (b) Cells for neighbor search

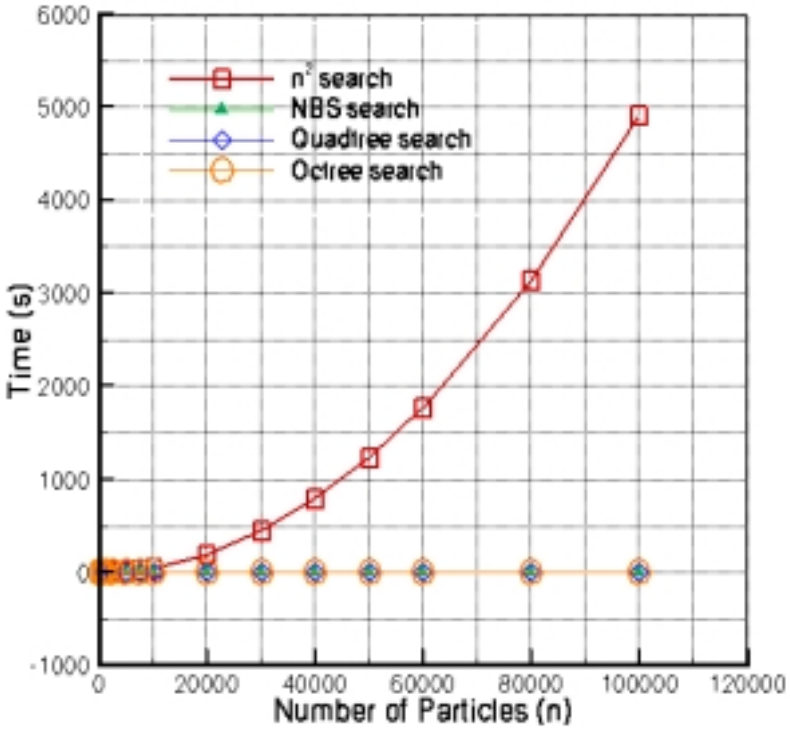

Figure 2.10. Comparison of various 2D search algorithms

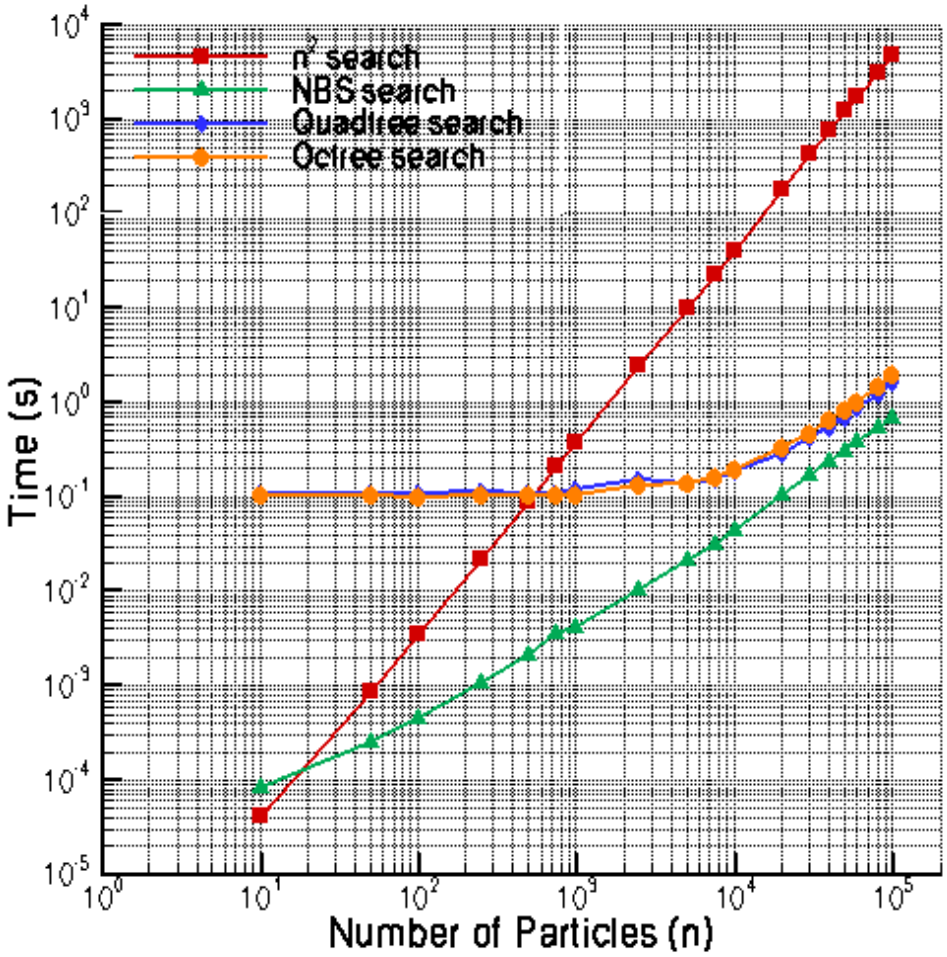

Figure. 2.11. Comparison of various 2D search algorithms on a logarithmic scale

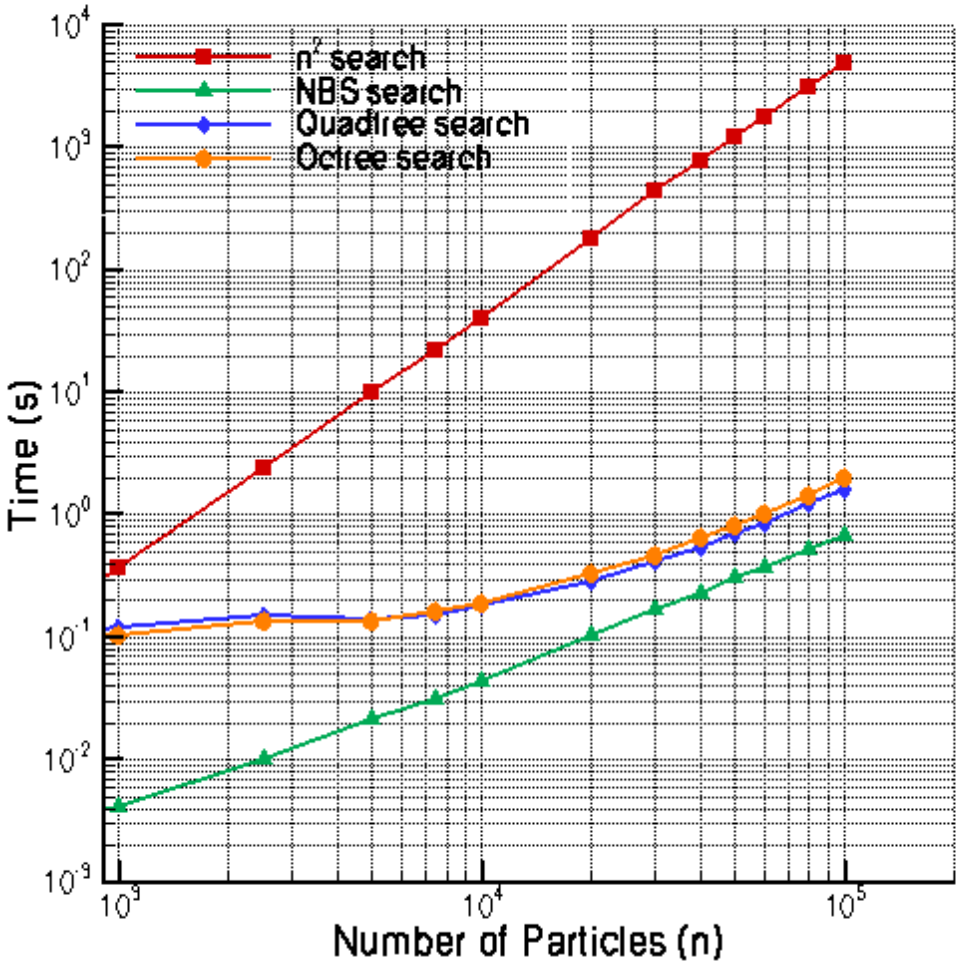

Figure 2.12. Comparison of various 2D search algorithms on a logarithmic scale for particle size over 1000

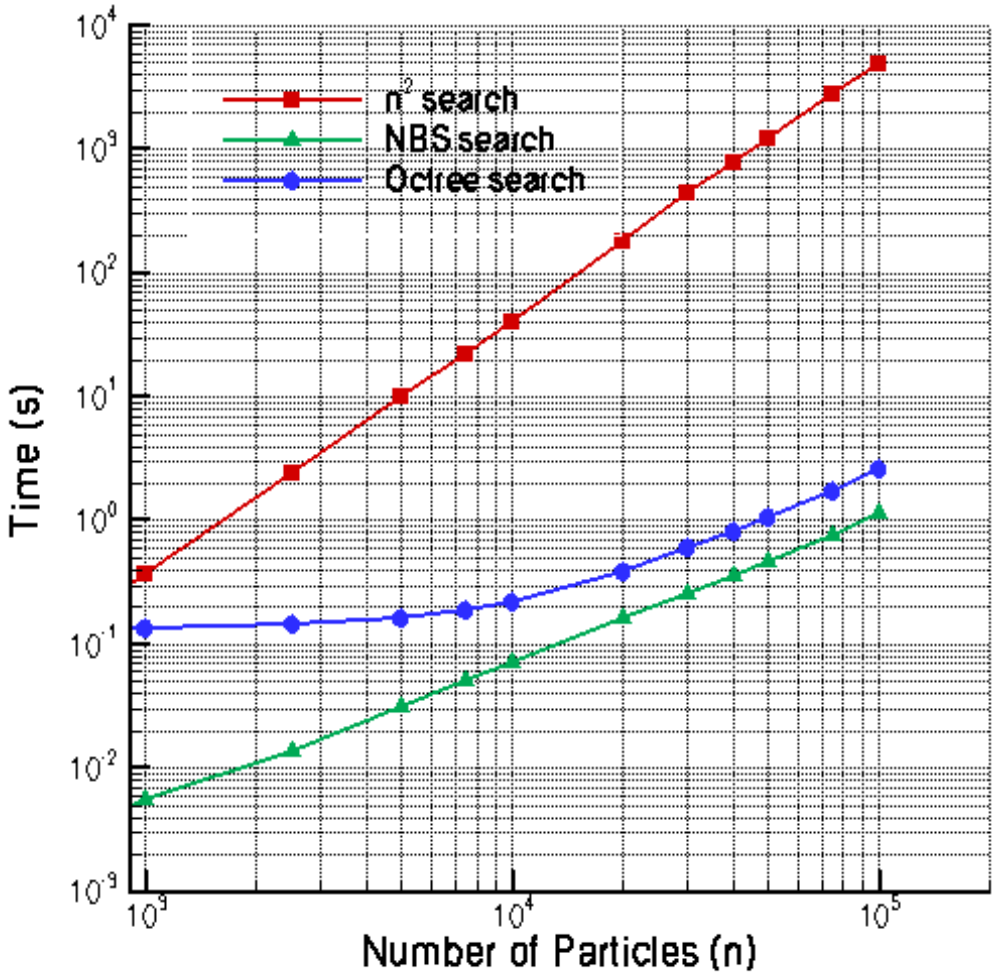

Figure 2.13. Comparison of various 3D search algorithms on a logarithmic scale for particle size over 1000

Chapter 3

Vibrated Granular Beds

Although granular materials are commonly found both in natural and industrial settings there is no general understanding of their behavior. Particulate systems are unique in the sense they exhibit gas-, liquid-, as well as solid-like properties. There are, however, important differences between each of these phases that make the behavior of granular materials even more unusual.

Single particle dynamics as well as beds of particles have been analyzed experimentally, and recently numerical studies are being done to reproduce existing work and to validate models. Experiments have been done on particle beds subjected to external vibrations and interesting patterns have been observed depending on certain parameters. Chladni (1787) is one of the earliest observers that sand scattered over a vibrating membrane collects into mounds corresponding to vibration anti-nodes. Faraday (1831) observed that particles in pile moving in circular convective patterns. Bachmann (1940) found that when the average depth of the bed is less than six particle diameters (known as a shallow bed) it exhibits random behavior similar to fluidized beds. A great deal of published work on granular beds has appeared in the last 20 years. Savage (1988, 1989) report noticing convective cells in a particle bed vibrated vertically from bottom with the maximum vibration amplitude in the center and the minimum near the side-walls. They observed two convective cells similar to vortices, with particles moving up at the center and down at the walls. They draw an analogy to acoustic streaming of air and explain the convective cell formation. Tanaka et al (1988) developed a mathematical

model to describe the particle motion in a hopper. Using their model they could successfully simulate hopper flows including formation of bridges, frictional wall effects and other flow phenomena. Evesque and Rajchenbach (1989) described the formation of inclined surface at the free surface of a particle bed subjected to vertical vibrations of low frequency and large amplitude. They noticed the convective transport of particles to the top on the upper side of the incline. Douady et al (1998) reported that when a particle bed in vibrated about a certain critical acceleration, the bed became unstable and defects were generated. Each defect separates solid-like regions oscillating out of phase. Gallas et al (1992) performed simulations based on molecular dynamics and have produced convection cells in vibrated particle beds. Pak and Behringer (1993) conducted experiments and observed that when the value of the acceleration amplitude is greater than 1g, convection cells appear. They reported internal convective transport of materials balanced by continuous surface avalanches leading to inclined surfaces. They noted the occurrence of surface waves on the free bed surface and reported that this happens after certain vibration acceleration and amplitude. Knight et al (1993) performed experiments to explain size separation in vibrated granular beds. They contradicted the accepted theory of size separation due to local rearrangements and proposed that size separation occurred due to particle convection cells. Particles move down at the walls and up at the center of the bed and the particles larger than the thin downward convecting stream at the walls are carried to the top and size segregation occurs. Melo et al (1994, 1995) and Metcalf (1996) examined wave patterns on the particle bed surface in detail. They reported that when viewed from the top the initially flat surface transitions into standing wave patterns at a critical bed acceleration. The surface appears to consist of stripes,

squares, pentagons and hexagonal and more complicated polygonal standing waves phase separated by kinks. The surface was observed to oscillate at half the bed frequency. Knight et al (1996) performed a detailed study of convective cells in a granular bed using magnetic resonance imaging. Brennen et al. (1996) studied experimentally the dynamics of the transition between the shallow bed and deep bed (h/d > 6) states. They noted that granular material subjected to vertical vibration exhibits at least one sudden expansion at critical acceleration amplitude. Hunt et al (1999) have experimentally studied the effect of horizontal vibrations on hopper flows. They have reported the funnel flows, inverted funnel flows and rat-hole formation phenomena and the associated acceleration values.

Meuth (1999) and Blair (2001) have studied the three-dimensional force distributions in a granular medium subjected to uniaxial compression. They studied the resulting normal force distribution on the bed walls and reported that the distribution is uniform for forces below the mean force and decays exponentially for forces above the mean force. An interesting phenomenon in granular material behavior is that they differ from fluids in the way they react to shear stresses. They develop shear bands which are narrow zones in the material which predominantly react to the applied shear and the adjacent regions behave as solids. Meuth et al (2000) have studied this phenomenon using magnetic resonance imaging and x-ray tomography and report that the granular microstructure is a key factor.

The behavior in deep beds varies based on the dimensionless vibration acceleration amplitude (Γ), defined as:

$$\Gamma = \frac{a\omega^2}{g}$$

Here a is the amplitude of oscillation, g the acceleration due to gravity, and $\omega = 2\pi f$; f is the oscillation frequency . Bed behavior also depends on the dimensionless bed depth defined as (h_o/d) where h_o is the initial particle bed depth and d is the equivalent particle diameter.

When the value of the acceleration amplitude is greater than one, convection cells appear. Particles move down in a boundary layer along the vertical walls of the container, circulate within the bulk of the granular bed to the free surface, and then avalanche toward the walls to repeat the cycle. Faraday (1831) was the earliest to report the behavior, which has been later reproduced and studied in detail by number of researchers including Evesque and Rajchenbach (1989), Ehrichs (1995), Wassgren et al (1996) among others. Convection results in a phenomenon known as *heaping*, which is characterized by a mound formed in the container (see Figure 3.1 (a)). For sufficiently large particles, the mound appears with the peak in the center of the container and the lowest particles at the walls.

A less-studied phenomenon is surface wave formation. Two regimes of standing waves appear in vibrated deep beds, for different values of the acceleration amplitude and they differ in both formation frequency and shape. The formation frequency is observed to be either half (f/2 waves) or one-fourth (f/4 waves) of the wall vibration frequency. The f/2 waves have smooth rounded peaks (Figure 3.1 (b)) and f/4 waves have sharper cusp-shaped waves (Figure 3.1.(c)). Fauve et al (1989), Pak and Behringer (1993), Melo et al. (1994, 1995), Miles and Henderson (1990) and Wassgren et al. (1996) have all reported these behaviors.

For much higher acceleration amplitudes kinks are formed (Figure 3.1 (d)). A kink is defined as a region of particle bed between two oscillations that oscillate out-of-phase with each other. The resulting bed motion appears as if arches form and collapse in time. Douady et al (1990), Melo (1994,1995) and Wassgren (1996) among others have published experimental and numerical studies of kink behavior.

3.1. Granular Beds with Single Particle Size

3.1.1. Theory

Wassgren (1996) describes in detail the underlying theory of surface wave formation using simple analysis of one ball or two balls bouncing on an oscillating floor, similar to published analysis of ball bouncing problems studying bifurcation (Holmes, 1982; Mehta and Luck, 1990; Luck and Mehta, 1993; as cited by Wassgren, 1996). The same analysis is reproduced here for ease of understanding the concepts and physics of surface wave formation.

The theory of a vibrated particle bed can be explained using a simple model consisting of a partially inelastic ball bouncing on a flat plate oscillating sinusoidally. Agglomerations of particles move coherently thus justifying the representation using a single ball and since the particle-wall collisions are assumed inelastic, the inelastic ball assumption is valid. The bouncing ball problem explains issues like bifurcation and provides a good insight into granular bed behavior.

The bottom wall moves sinusoidally as

$$b(t) = a\sin(\omega t)$$

where b is the vertical position of the bottom wall, a is the vibration amplitude, ω the vibration frequency in radians, and t the time.

The trajectory of the ball when not in contact with the base is

$$p(t) = -\frac{1}{2} g (t - t_{n-1})^2 + v_{n-1}^1 (t - t_{n-1}) + p_{n-1}$$

where p is the vertical position of the particle, g the acceleration due to gravity, t_{n-1} the time of the last contact with the base, v_{n-1}^1 the particle velocity immediately following the last contact with the base at time t_{n-1} and p_{n-1} the particle position at t_{n-1}.

The coefficient of restitution e is defined as the ratio of relative velocity between particle and base after the collision to the relative velocity prior to collision.

$$e = -\frac{v\left(t_{n-1}^1\right) - \dot{b}\left(t_n^0\right)}{v\left(t_n^0\right) - \dot{b}\left(t_n^0\right)}$$

and $0 \le e \le 1$

Using non-dimensional parameters defined as follows in the trajectory equation:

$$B = \frac{b\omega^2}{g}; P = \frac{p\omega^2}{g}; \Gamma = \frac{a\omega^2}{g}; \dot{B} = \frac{\dot{b}\,\omega}{g}; V = \frac{v\omega^2}{g}; \phi = \omega t \text{ , we get}$$

$$-\frac{1}{2}(\phi - \phi_{n-1})^2 + V_{n-1}^1 (\phi - \phi_{n-1}) + \Gamma \sin\phi_{n-1} - \Gamma \sin\phi_n = 0 \qquad 3.1(a)$$

$$V_n^1 = -eV_{n-1}^1 + e(\phi - \phi_{n-1}) + (1+e)\Gamma \cos\phi_n \qquad 3.1\ (b)$$

The periodic conditions are

$$\phi_n = \phi_{n-1} + 2\pi m$$

where m>0;

$$V_n^1 = V_{n-1}^1$$

The solution (ϕ^*, V^*) is given by

$$\Gamma \cos\phi^* = \frac{m\pi(1-e)}{(1+e)}$$

$$V^* = m\pi$$

where (ϕ^*, V^*) are the fixed points. The stability of the solutions is determined by analyzing the eigenvalues of the linearized Jacobian of equations (3.1.a) and (3.1.b). The critical values of Γ are,

$$\Gamma_m = \frac{m\pi(1-e)}{(1+e)}$$

$$\Gamma_m' = \left\{ \left(\frac{m\pi(1-e)}{(1+e)}\right)^2 + \left(\frac{2(1-e)^2}{(1+e)^2}\right)^2 \right\}^{1/2}$$

These Γ are the bifurcation values. At the first value, in a saddle-node bifurcation, two fixed point trajectories appear only one of which is stable. At the second value a change of stability occurs and the solution becomes unstable. For $\Gamma \le \Gamma_m$ the particle flight time is less than the oscillation period and the particle bounces several times before coming to rest on the base. This motion is repeated every oscillation cycle. For $\Gamma_m \le \Gamma \le \Gamma_{m,stable}'$, a periodic fixed point trajectory exists and the particle motion repeats

after every collision. For $\Gamma \geq \Gamma_m^{'}$ the particle exhibits a period two motion. Thus the transition of bed behavior from heaping to surface waves can be explained.

In case of kinks the same analysis is repeated with two bouncing balls considered extremely inelastic. Then the equations 3.1.a and 3.1.b would be

$$-\frac{1}{2}(\phi-\phi_{n-1})^2 + V_{n-1}^1(\phi-\phi_{n-1}) + \Gamma\sin\phi_{n-1} - \Gamma\sin\phi_n = 0$$

$$V_n^1 = \Gamma\cos\phi_n$$

The saddle node bifurcation occurs at

$\Gamma_m = m\pi$ (for m>0)

and the stability bifurcation occurs at $\Gamma_m^{'} = \sqrt{m^2\pi^2+4}$

For $\Gamma<\Gamma_1$, the two particles move identically and synchronously. When $\Gamma_1 \leq \Gamma \leq \Gamma_1^{'}$, only one of the two trajectories that are 180^o out of phase, is stable. For $\Gamma_1^{'} \leq \Gamma \leq \Gamma_2$, the ball has a single trajectory but two flight times and thus the ball motions can be out of phase resulting in kinks.

3.1.2. Heaping

Side wall convection and heaping have been the most extensively studied vibrated bed behaviors. A number of experiments, simulations and theoretical works have been reported in literature. Heaping or formation of a mound (see Figure 3.1(a)) occurs primarily because of side-wall convection for acceleration amplitude values of $1.2 \leq \Gamma \leq 2.0$ for a non-dimensionalized bed depth of 20. The convection cell pattern is such that the particles move down at the walls and move upwards in the center of the bed.

It should be noted that the downward motion mentioned is not the instantaneous motion, but are long-term motions of the particles. For acceleration amplitude values in the mentioned range, the granular bed deforms near the walls and the disturbances slowly propagate toward the center of the container. The mounds have a rounded free surface with the lowest points at the walls and the highest points near the center. The mounding behavior is not influenced by perturbation. Of the factors influencing heaping, friction of the lateral walls and the friction between the particles are the most important. As the friction increases side wall convection increases. We performed two-dimensional simulations to observe heaping. The simulation parameters are shown in Table 3.1. Heaping has been observed and is shown in Figure 3.6.

3.1.3. Surface Waves

When a particle bed is vibrated vertically with an acceleration amplitude greater than the range for heaping, standing surface waves are observed. Surface wave formation in a vibrated particle bed has been analyzed both experimentally and by simulation. Some of the salient features as reported (Miles and Henderson, 1990; Pak and Behringer, 1993; Melo, 1994-95; Wassgren, 1996 among others)

- The particles in the bed are in a fluidized state during the surface wave formation.
- Surface waves appear for two separate regions of Γ. For a given bed depth of $h_o/d = 10$, the first set occurs when $2.2 \leq \Gamma \leq 4.2$ and the second set occurs when $5.8 \leq \Gamma \lhd\approx 7.8$. The ranges narrow down as the bed depth increases.
- The two sets of waves are referred to as *f/2* waves, which appear at the lower range of the acceleration amplitude and *f/4* waves, which appear at the higher

range of the acceleration amplitude. The reason for a gap in the ranges is that during these regimes the flight motion undergoes period doubling bifurcation resulting in kink formation.

- *f/2* waves have a flight time less than the oscillation period of the forcing vibrations and the *f/4* waves have a flight time greater than the oscillation period of the forcing vibrations.
- *f/2* waves take two wall cycles for one surface wave cycle. Figure 3.2 is an illustration to explain the *f/2* wave cycle. *f/4* waves take four wall cycles for one surface wave cycle . The *f/4* wave cycle is explained in Figure 3.3.
- In the *f/2* wave regime two kinds of waves exist: round waves and cusp waves. In the *f/4* regime only the cusp waves exist.
- Round waves are characterized by a surface with smooth rounded crests and troughs as shown in Figure 3.1 (b). Cusp waves are characterized by a surface with extremely sharp peaks as shown in Figure 3.1 (c).
- In the case of round waves only the top few layers of particles are fluidized and involved in wave formation while the bottom layers of particles move in a consolidated manner. In the case of cusp waves the whole bed is fluidized and influence the motion of particles within the entire bed.
- In the cusp wave formation process, when a wave peak forms, the particles below it move up leaving dents with large radii of curvature along the bottom surface of the bed. Also the particles are ejected from the peaks of the cusp waves resulting in a significant amount of particle mixing.

- The wave amplitude (defined as twice the maximum distance between a peak and the neighboring trough) of all surface waves is proportional to the oscillation amplitude. The wavelength also increases with increasing wall acceleration amplitude.
- The effect of inter-particle friction on the bed behavior is similar to the effect of viscosity on fluid behavior.

Two-dimensional discrete element simulations have been performed to observe surface waves. The simulation parameters are shown in Tables 3.1 and 3.2. Simulations have been performed only in the *f/2* wave range of Γ. Round waves and cusp waves have been observed. A snapshot of the simulated round waves is shown in Figure 3. 7. The round waves were simulated with 8000 particles, Γ=2.0; the remainder of parameters are shown in Table 3.1. Cusp waves obtained from simulations are shown in Figure 3.8. Cusp waves have been simulated for a variety of cases: (i) for 8000 particles with Γ=2.0 and the remainder of parameters as shown in Table 3.1, and (ii) for 3000 particles and varying Γ (=2.5 to 4.0) keeping *f* fixed at 20 Hz. Qualitatively the trends observed are same as those reported in existing literature. The wave amplitude increases with increasing Γ for a fixed *f*. The surface wave wavelength has a weak dependence on the oscillation acceleration amplitude.

Both round and cusp waves form as a result of the coupling between the base oscillations and the particle motion. The two relevant time scales in the formation of the waves are the forcing oscillation (the wall oscillation) period and the free fall time of the

particles. The resonance condition selects the wavelength and the wave amplitude since the particles must alternate between a wave and the neighboring wave.

Figure 3.8 shows the particle bed shape at two intervals in the bed oscillation cycle. For each wall oscillation cycle eight snapshots have been stored at equal intervals of time. Figure 3.9 shows 16 such continuous snapshots. In the figure, the particle bed goes gradually from an almost flat bed to a bed with cusp waves. Then it falls back to a flat bed and the process repeats. Let us call the first rise of the flat bed to form cusp waves and back to a flat bed as phase X of the bed motion and the following repetition of the process as Phase Y of the bed motion. Though both phases X and Y result in cusp formation, they are different from each other. In the regions of the bed where crests are observed in phase X of the bed motion host troughs in phase Y of the bed motion and the troughs change to crests. Thus standing waves are formed. This can be seen by following the line AA in Figure 3.9. One can observe the trough changing to crest. In Figure 3.9 the first eight bed shapes correspond to phase X and the next eight correspond to phase Y. Phases X and Y together constitute a wave of the bed particles. Since eight snapshots equal one wall oscillation cycle, sixteen snapshots mean two wall oscillation cycles. Thus the time taken for one oscillation of the cusp wave shown in Figure 3.9 is twice the time taken for one oscillation of the bottom wall. Hence the frequency is *f/2*. In Figure 3.8 the two bed positions are chosen one each from the two phases X and Y. Standing wave formation can be understood by following AA and BB. Figure 3.10 shows four bed shapes in the whole bed wave cycle and their corresponding particle velocities. One can see that it agrees with the Figure 3.3.

3.1.4. Kinks

Of the many interesting behaviors exhibited by vibrated particle beds, an interesting phenomenon is that of kink formation. For deep beds vibrated with acceleration amplitudes greater than $\Gamma = 4.2$, kinks are observed. A kink is defined as a region of the particle bed between two sections that oscillate out-of-phase with each other. The resulting bed motion appears as if it forms arches and collapse in time. Figure 1(d) shows an illustration of a section of a bed with three kinks. The particle bed can be visualized as consisting of sections of solid bodies and each section moves up and down out of phase with its immediate neighbors. Thus when a section lifts off the bed floor, its immediate neighbors hit the bed floor forming an arch. The points of deflection are called kinks.

Various experiments and observations studying kink formation in vibrated particle beds have been reported in the available literature. Some important features describing kink behavior may be found in Douady (1989, Melo(1994,1995) and Wassgren, (1996):

- Kinks only appear after the flight time of the bed undergoes period bifurcation. This bifurcation occurs after a critical Γ, which decreases with increasing bed depth.
- The number of kinks that can exist for a given bed depth and vibration parameters is not unique. Perturbation can cause a change in the kink number, which can either increase or decrease.
- For a given bed depth and acceleration amplitude there exists a minimum distance between kinks.

- The above two points indicate that though different number of kinks can exist for the same bed there is a maximum limit on this number.
- Kinks never occur at the walls.
- On either sides of a kink there exist counter-rotating convection cells. The particles move down at the kinks and move up on either sides of it.
- When kinks occur near the walls the particles move upward indicating that the kink convection is stronger than side-wall convection. When kinks occur far from the walls side wall convection dominates kink convection and the particles at the wall move downwards.

Two-dimensional DES simulations have been performed in the reported range of the parameters which influence kink behavior. The simulation parameters used are shown in Table 3.3. Kinks have been produced, as shown in Figure 3.11, and the kink behavior reported in the literature has been observed. Figure 3.11 shows a bed with two kinks. Three distinct sections in the bed can be seen, with the middle section moving up and down out of phase with the corner sections. Figure 3.12 shows the gradual oscillation of the simulated bed. Starting from a flat state a rise in the middle section can be noticed. It reaches a maximum, lifting off from the bed floor while the other two sections are in contact with the floor, forming an arch. It then moves down and the bed comes back to the flat state. The middle section moves further down pressing into the floor while the corner sections lift off forming an inverted of the arch. The corner sections move down after reaching a maximum height and the bed returns to the flat state. This whole process is one bed oscillation cycle. Sixteen snapshots of the bed for required for one cycle. As

eight snapshots constitute one wall oscillation cycle, we may conclude that one kink oscillation in this case takes 2 wall oscillation cycles and hence is an f/2 wave.

The mechanism of kink formation can be explained thus (Douady at al 1989). When a section of the bed hits the bottom wall, the particles in that section consolidate and in effect "solidify". The particles still in flight avalanche down over this solid-like region and away from it. This results in consolidation and hence an effective solid-like sections in the neighboring region. The out of phase motion of sections of the bed and dilation of the bed during flight results in kink associated convection cells. This phenomenon explained by Douady et al (1989) is represented as a schematic in Figures 3.4 and 3.5. This phenomenon has been observed in simulations. The particle bed shape at 4 intervals covering the bed oscillation cycle and the corresponding particle velocities are shown in Figure 3.13. One can see the particle motion and the resulting kinks in Figure 3.5.

3.2 Granular Beds with Two Particle Sizes

Industrial applications seldom have granular mixtures with particles of a single size. Often there are mixtures with a distribution of particle sizes and the behavior in such systems differs from single size particle systems. In particular, since bed vibration is used as a mechanism for both segregation as well as mixing, it is critical to understand the segregation behavior of binary beds. It is observed that when particles of different sizes are heaped in a bottom-wall vibrated box and when the acceleration amplitudes are in the heaping regimes, there is percolation effect and the bigger particles rise to the top. Knight et al (1993) have performed experiments to explain size separation in vibrated granular

beds. They contradicted the accepted theory of size separation due to local rearrangements and proposed that size separation occurred due to particle convection cells. Particles move down at the walls and up at the center of the bed and the particles larger than the thin downward convecting stream at the walls stay at the top and size segregation occurs. This behavior occurs in laterally confined beds for low values of the acceleration parameter.

In the present study, the behavior of binary mixture systems vibrated in the surface waves and kink regimes is studied. A mixture of two particle sizes is studied in the diameter ratio range of 2-4. All other relevant parameters are given in Table 3.4. Our simulations exhibit kinks when acceleration amplitude is in the kink forming range (>4.5) for the given bed height (h/d=20). A variety of interesting behaviors is observed depending on the diameter ratio d_1/d_2. For a size ratio of 2, when the bed is vibrated in the kink regime, kinks do form but over a period of time the particles segregate to form alternate sections of bigger and smaller particles, called horizontal segregation. The pattern is preserved in space and time. This is illustrated in Fig. 3.14. This behavior may be contrasted with that observed in the heaping regime where larger particles rise to the top, causing vertical segregation.

The horizontal segregation phenomenon is initial condition independent. Three different initial conditions were considered: (i) the bigger (red) particles are initially sandwiched between two layers of smaller (blue) particles. (ii) the bigger (red) particles are initially on top of the smaller (blue) particles, and (iii) the bigger(red) particles are placed initially below the smaller particles. The end result shows clear horizontal segregation as in Fig. 3.15. The volume fraction of big and small particles in the

computational domain is plotted in Fig 3.16, corresponding to the initial setup shown in Fig 3.15. We see that there exist regions where the volume fraction of big particles is almost negligible compared to that of smaller particles. Such sections alternate with regions where the volume fractions of particles of both sizes are comparable. This clearly illustrates the concept of horizontal segregation. Horizontal segregation can be explained based on the convection cell formation in kinks. Bigger particles accumulate where the kinks are formed. The sections that hit the floor periodically forming the kinks are regions of high mixing. The regions in between have low mixing and such regions can be called as dead zones. The bigger particles steer away from dead zones and group into the kink regions of high mixing. Once they enter a convection cell they get trapped in the kink convection cell and do not enter the dead zones. Thus we get alternate sections of big and small particles and horizontal segregation results.

This effect is not seen in beds with a single particle size. Fig. 3.17 shows a kink formed in a vibrated granular bed of a single particle size. The simulation parameters are given in Table 3.3. Particles have been colored red and blue to observe segregation. The red particle layer is initially sandwiched between layers of blue particles. Thorough mixing can be observed and no segregation is seen to occur.

Binary mixtures of diameter ratios up to 4 have also been studied. Tanaka et al (1996) have reported conditions for mixing and segregation and formulated the segregation criterion as

$$0.5 < \left(\frac{d_2}{d_1}\right)\left(\frac{\rho_2}{\rho_1}\right)^2 < 2$$

where the subscripts 2 and 1 stand for bigger and smaller particles respectively. Simulations have been performed keeping the above criterion in consideration. Particle

size ratios were increased from 1 to 4 in steps of 0.25. Horizontal segregation is dominant when the particle size ratio is less than 3. Though some horizontal segregation seems to take place for a size ratio of 3, the bigger particles sediment to the bottom and do not segregate much for higher size ratios. Fig 3. 18 shows that for size ratios of three and above, horizontal segregation is not observed. The mass of the particle increases as the cube of the diameter, so that for larger size ratios, particle weight effects dominate.

The effect of density on segregation has also been studied, keeping the particle size constant. The segregation criterion proposed by Tanaka et al (1996) has been kept in mind in choosing parameters. Density ratios ranging from 1 to 3 have been studied keeping the particle sizes constant. The bed height and other simulation parameters are given in Table 3.3. It has been observed that irrespective of the initial placement of the denser particles, segregation does not occur based on density differences (Figure 3.19.). Weight effects are observed when the density ratios reach around 3 and the denser particles appear to sediment at intervals, but get pulled into the convection cell and mix thoroughly. Size variation plays a more important role than density differences in horizontal segregation in binary mixtures vibrated in the kink regime.

Some interesting observations made in the study of binary mixtures vibrated in kink regimes are:

- Horizontal segregation occurs as opposed to vertical segregation for size ratios less than three.
- The segregation behavior is initial condition independent.
- Bigger particles cluster at the kink regions and away from the dead zones and get trapped in the convection cells.

- For the kinks formed, cusp waves are also observed on the surface.
- Horizontal segregation seems to be predominant when the particle ratios are below 3, above which sedimentation dominates.
- Particle size variation contributes more to segregation than particle density variation.

3.3. Computational Time

DES is a computationally expensive methodology. The computational time required depends on the regime being simulated. For the kink regime with about 8000 particles, about 5 days of elapsed time were required to simulate 10 seconds. The computer used was a PC with a 1.7 GHz Pentium 4 processor with 2 Gb RAM. The computational time required for the surface wave regimes was approximately 3-4 days on the same machine. Heaping regimes take longer to develop and even longer computational times are required.

3.4. Closure

In this chapter, we have used the discrete element method to simulate particle transport in vibrated beds for a range of bed acceleration parameters. The results obtained agree well with previously published observations and simulations and capture a range of important bed behaviors. The results in this chapter demonstrate that the DES implementation is working well, and integration with a gas-phase simulation can be undertaken with confidence.

Segregation behavior in the kink regime has been studied for binary particle mixtures in the diameter ratio range of 1-4. For size ratios less than three, horizontal segregation has been observed and explained. This can be used for particle separation and sorting, size characterization, and other important phenomena in industry. Density differences were found not to influence segregation.

Table 3.1. Simulations parameters used to simulate heaping

Γ	1 to 2
F	20 Hz
W/d	100
h_o/d	20
N	2000
ε_{pp}	0.80
$k_{n,pp}$	$5289* 10^3$ N/m
$v_{n,pp}$	$8.337 * 10^{-2}$ (N.s)/m
$k_{s,pp}$	$5289* 10^3$ N/m
μ_{pp}	1.0
Lateral boundaries	Walls
ε_{pp}	0.70
$k_{n,pw}$	$1.058 * 10^3$ N/m
$v_{n,pw}$	$1.667 * 10^{-2}$ (N.s)/m
$k_{s,pw}$	$1.058 * 10^3$ N/m
μ_{pw}	1.0
d	1.0 mm
ρ	2500 kg/m^3
Δt	$3.504 * 10^{-6}$ s

Table 3.2. Simulations parameters used to simulate surface waves

Γ	2.5 to 4
F	20 Hz
W/d	200
h_o/d	15
N	3000
ε_{pp}	0.50
$k_{n,pp}$	$3.602 * 10^{3}$ N/m
$\nu_{n,pp}$	$2.092 * 10^{-2}$ (N.s)/m
$k_{s,pp}$	0.0 N/m
μ_{pp}	0.0
Lateral boundaries	Periodic
ε_{pp}	0.70
$k_{n,pw}$	$7.203 * 10^{3}$ N/m
$\nu_{n,pw}$	$4.184 * 10^{-2}$ (N.s)/m
$k_{s,pw}$	0.0 N/m
μ_{pw}	0.0
d	1.0 mm
ρ	2500 kg/m^3
Δt	$4.337 * 10^{-6}$ s

Table 3.3. Simulations parameters used to simulate kinks

Γ	6.0
F	25 Hz
W/d	200
h_o/d	40
N	8000
ε_{pp}	0.70
$k_{n,pp}$	$4.701 * 10^3$ N/m
$\nu_{n,pp}$	$1.251 * 10^{-2}$ (N.s)/m
$k_{s,pp}$	0.0 N/m
μ_{pp}	0.0
Lateral boundaries	Periodic
ε_{pp}	0.70
$k_{n,pw}$	$9.402 * 10^3$ N/m
$\nu_{n,pw}$	$2.502 * 10^{-2}$ (N.s)/m
$k_{s,pw}$	0.0 N/m
μ_{pw}	0.0
d	1.0 mm
ρ	2500 kg/m^3
Δt	$4.337 * 10^{-6}$ s

Table 3.4. Simulations parameters used to simulate kinks in binary mixtures

Γ	5.5
F	25 Hz
d_2/d_1 *(big dia/small dia)*	2 (ratios of 3, 4 also studied)
W/d_1	200
h_o/d_1	36
N	4500 (N_1/N_2 = 4000/500)
ε_{pp}	0.70
$k_{n,pp}$	$4.701 * 10^3$ N/m
$\nu_{n,pp}$	$1.251 * 10^{-2}$ (N.s)/m
$k_{s,pp}$	0.0 N/m
μ_{pp}	0.0
Lateral boundaries	Periodic
ε_{pp}	0.70
$k_{n,pw}$	$9.402 * 10^3$ N/m
$\nu_{n,pw}$	$2.502 * 10^{-2}$ (N.s)/m
$k_{s,pw}$	0.0 N/m
μ_{pw}	0.0
d	1.0 mm
ρ	2500 kg/m^3
Δt	$4.337 * 10^{-6}$ s

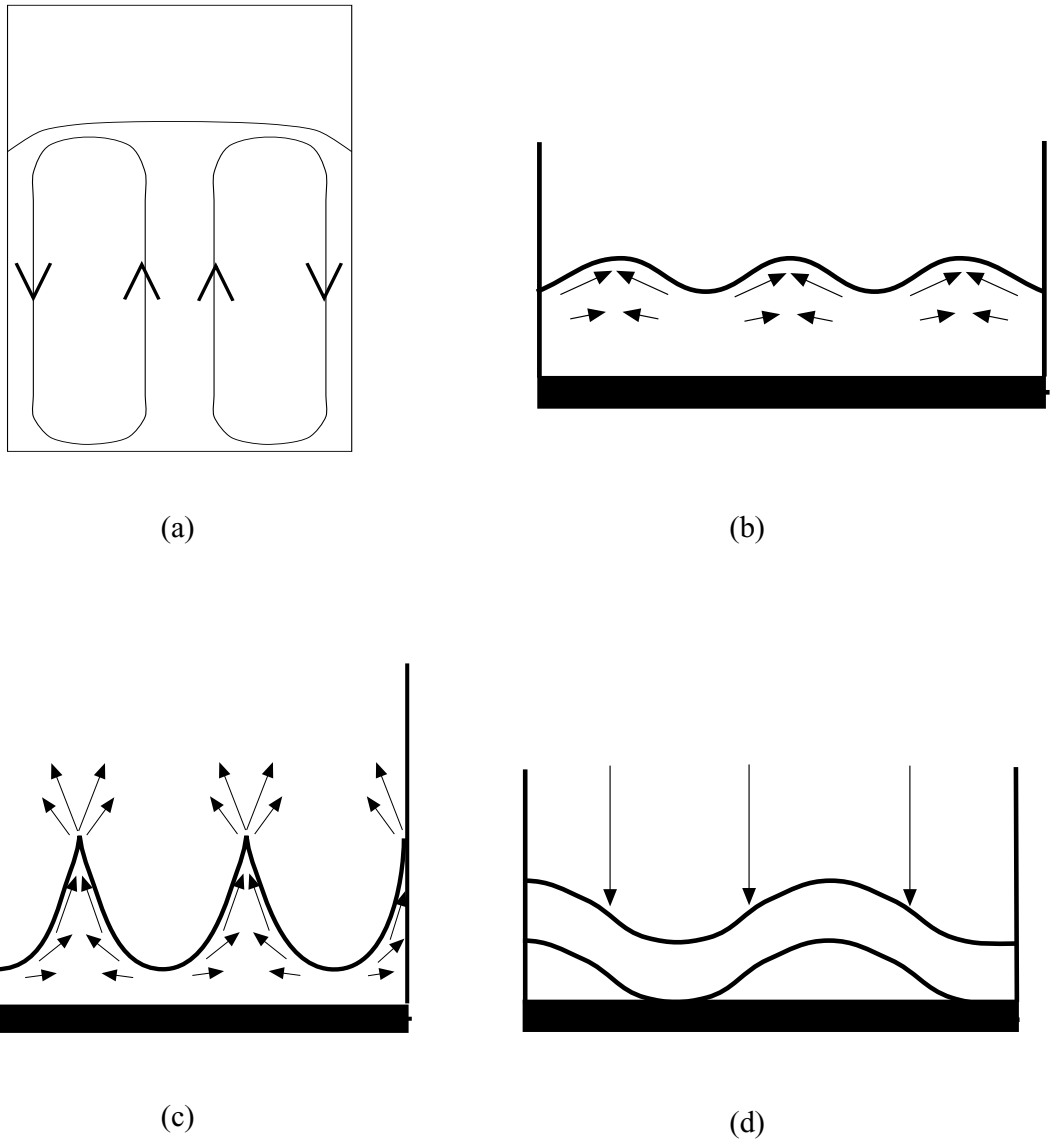

Figure 3.1. Illustrations of particle bed behavior (a) Heaping (b) Round surface waves (c) Cusp surface waves (d) Kinks (from Wassgren, 1996)

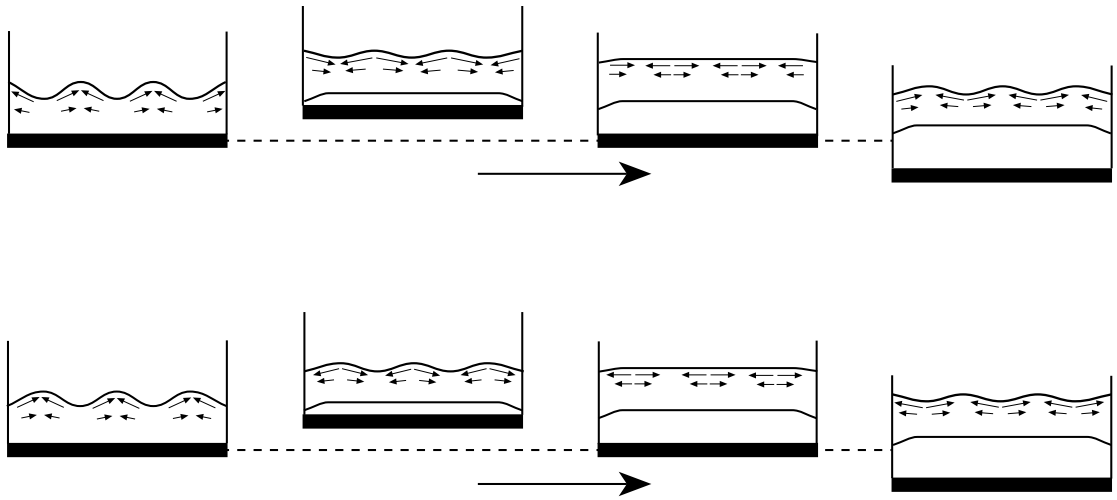

Figure 3.2. An illustration showing the motion of particles (round surface waves are shown) for f/2 waves over two oscillations. (from Wassgren, 1996)

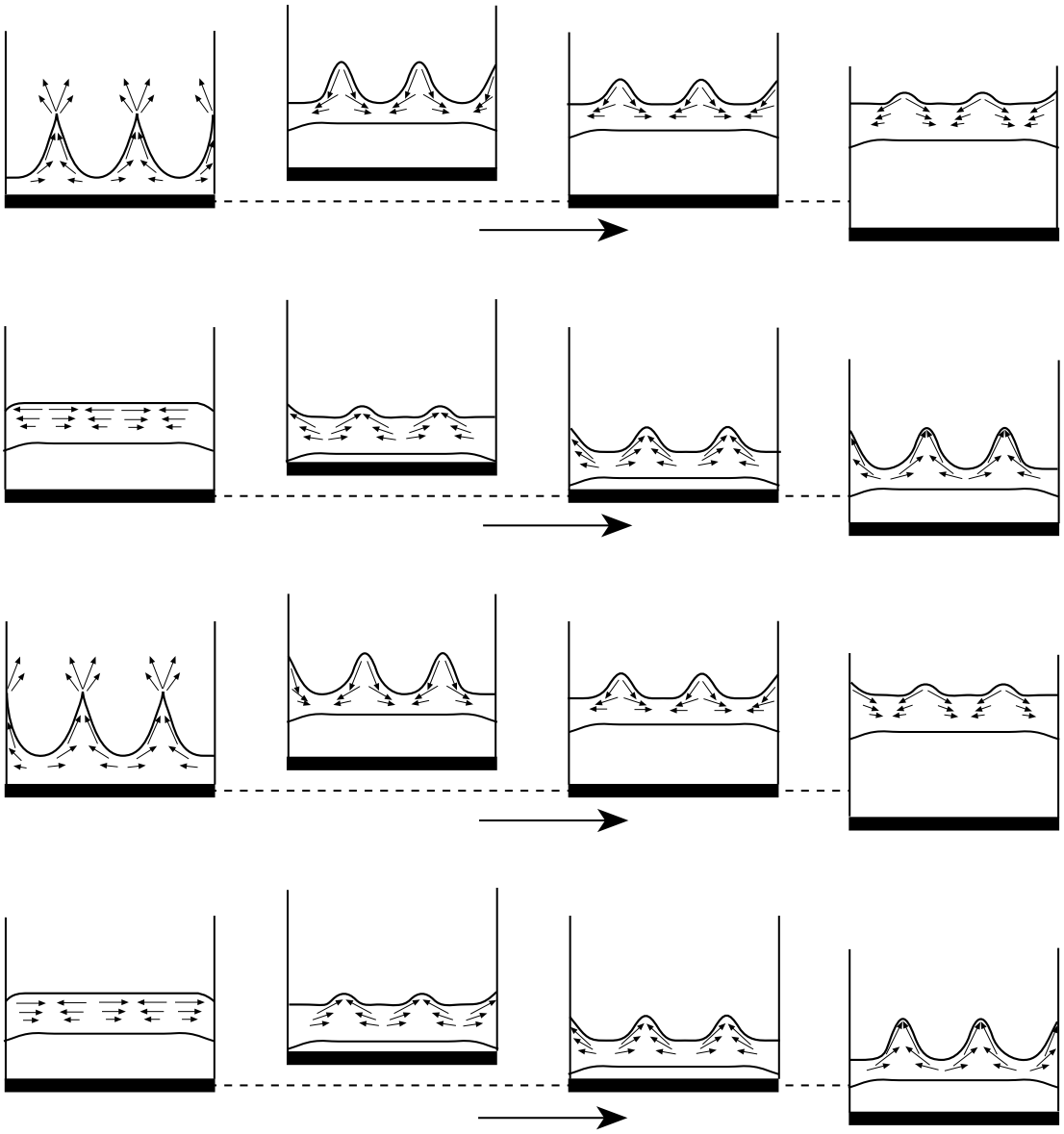

Figure 3.3. An illustration showing the motion of particles (cusp surface waves are shown) for f/4 waves over two oscillations. (from Wassgren, 1996)

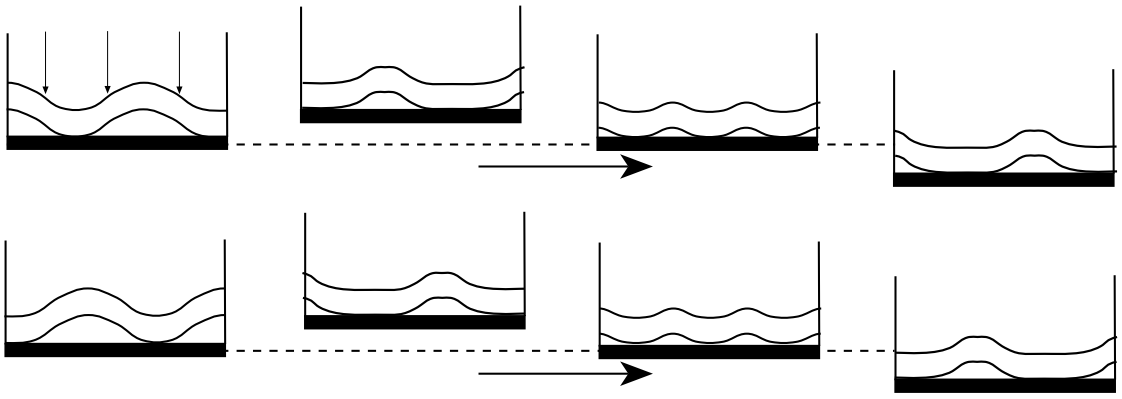

Figure 3.4 An illustration showing the particle bed motion with 3 kinks (indicated by arrows) over two oscillation cycles. (from Wassgren, 1996)

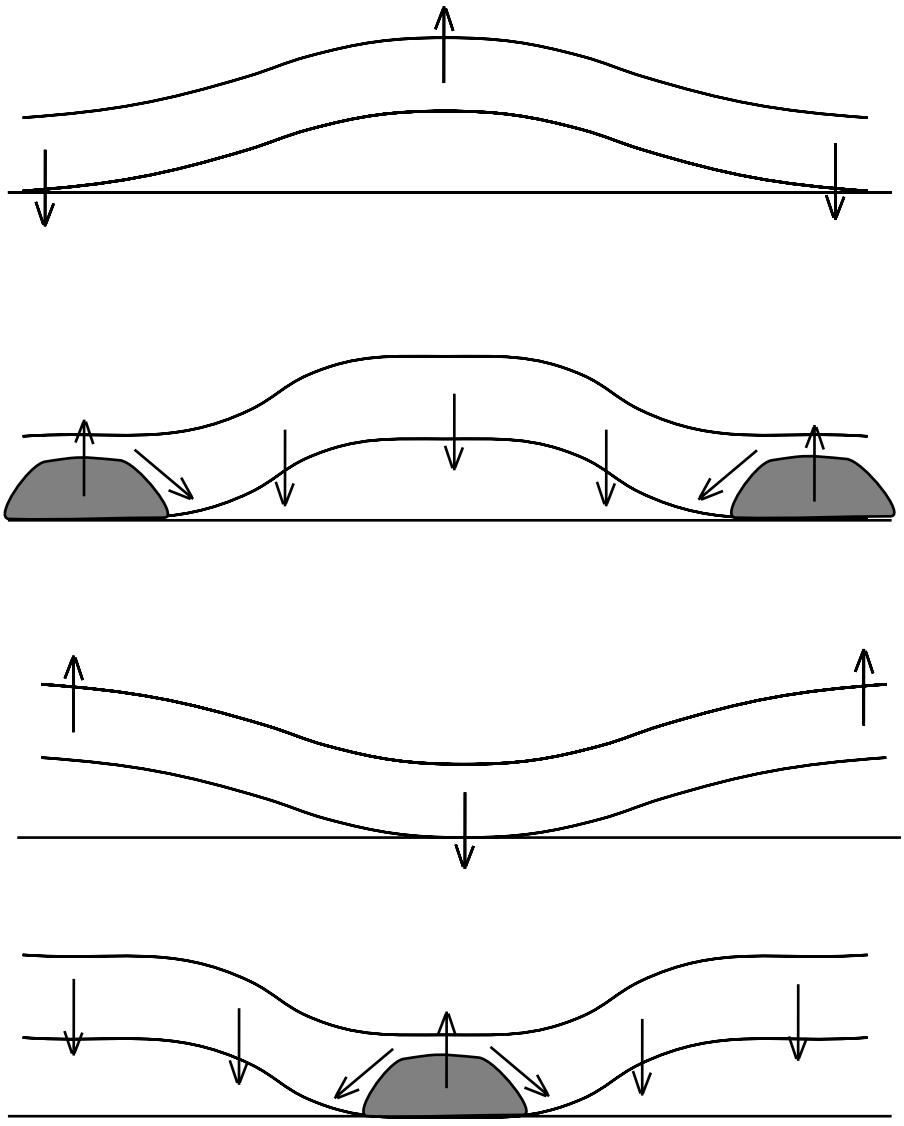

Figure 3.5. Illustrations showing the mechanism proposed by Douady *et al*. (1989) to explain the minimum kink separation distance and the convection cells associated with kinks.

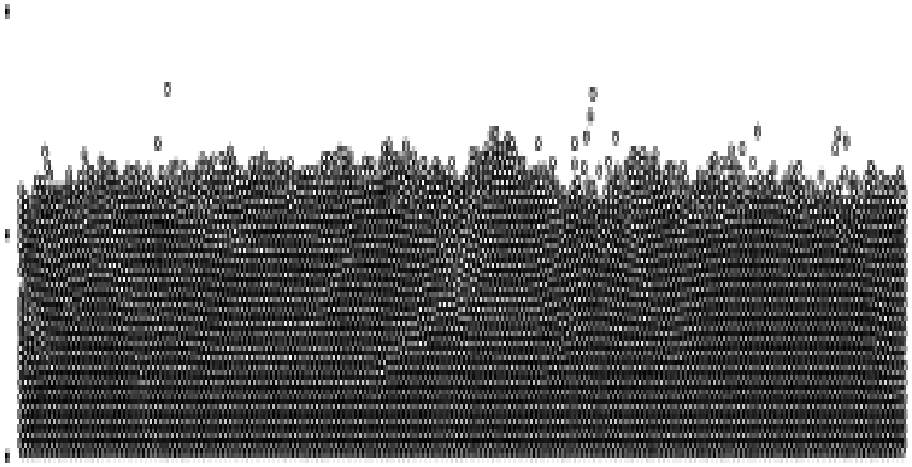

Figure 3.6. Illustration showing the simulation results for heaping formation. Simulation is done for 2000 particles, Γ=1.5, f= 20; the remainder of simulation parameters are given in Table 3.1.

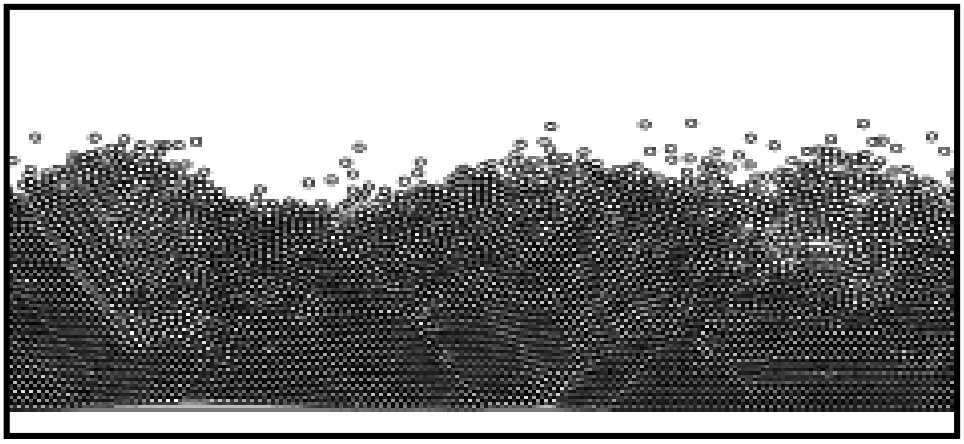

Figure 3.7. Illustration showing the simulation results for the formation of the round surface waves. Simulation is done for 8000 particles, Γ=2.0, f= 25; the remainder of simulation parameters are given in Table 3.1.

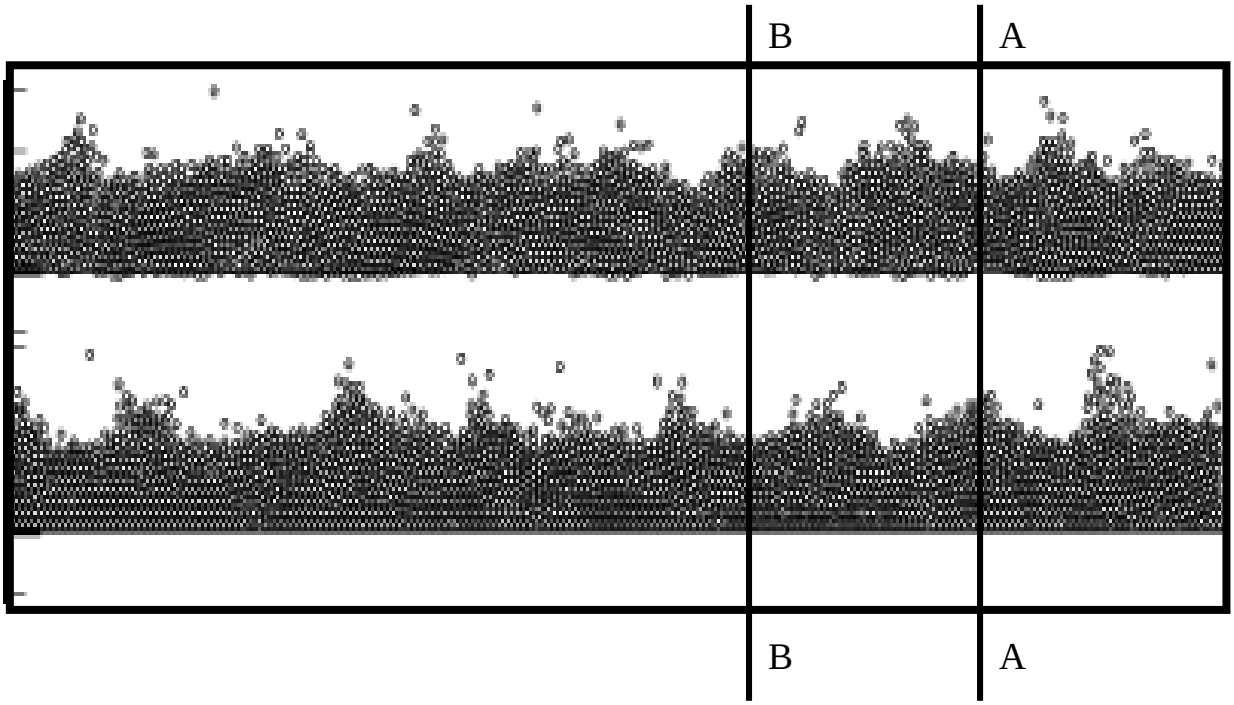

Figure 3.8. Illustration showing the simulation results for cusp wave formation. Snapshots of two positions during the oscillations are shown to highlight the alternating crests and troughs of the standing wave. See AA, BB. Simulation parameters are given in Table 3.2.

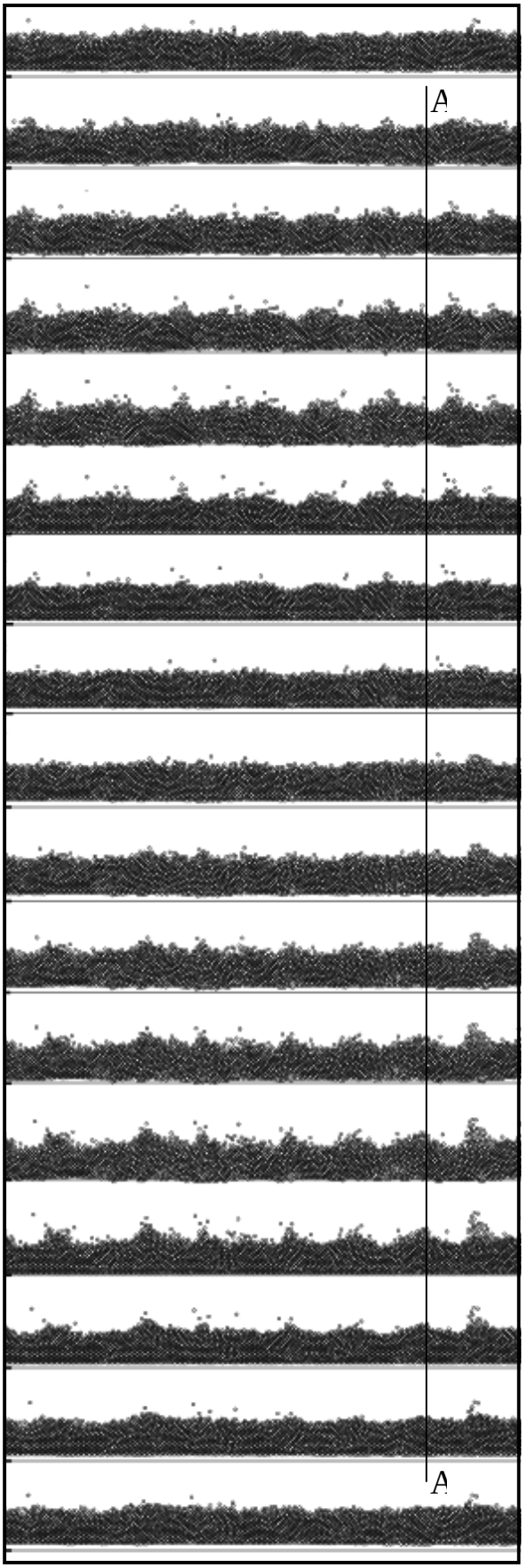

Figure 3.9. Illustration demonstrating the *f/2* cusp waves simulated. The simulation parameters are given in Table 3.2.

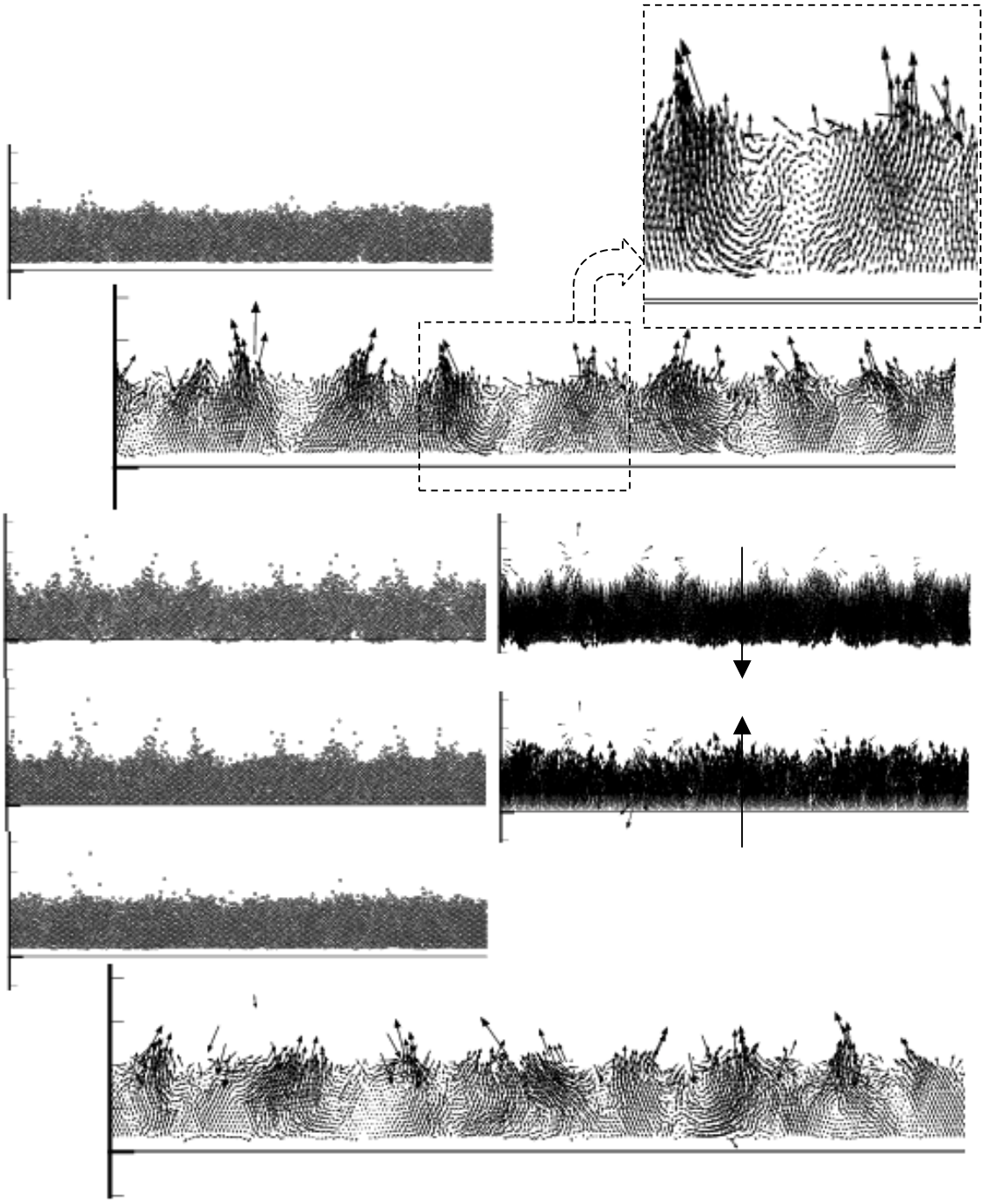

Figure 3.10. Illustration showing the cusp waves and the particle velocities at four different instances in a half-cycle of the bed oscillation.

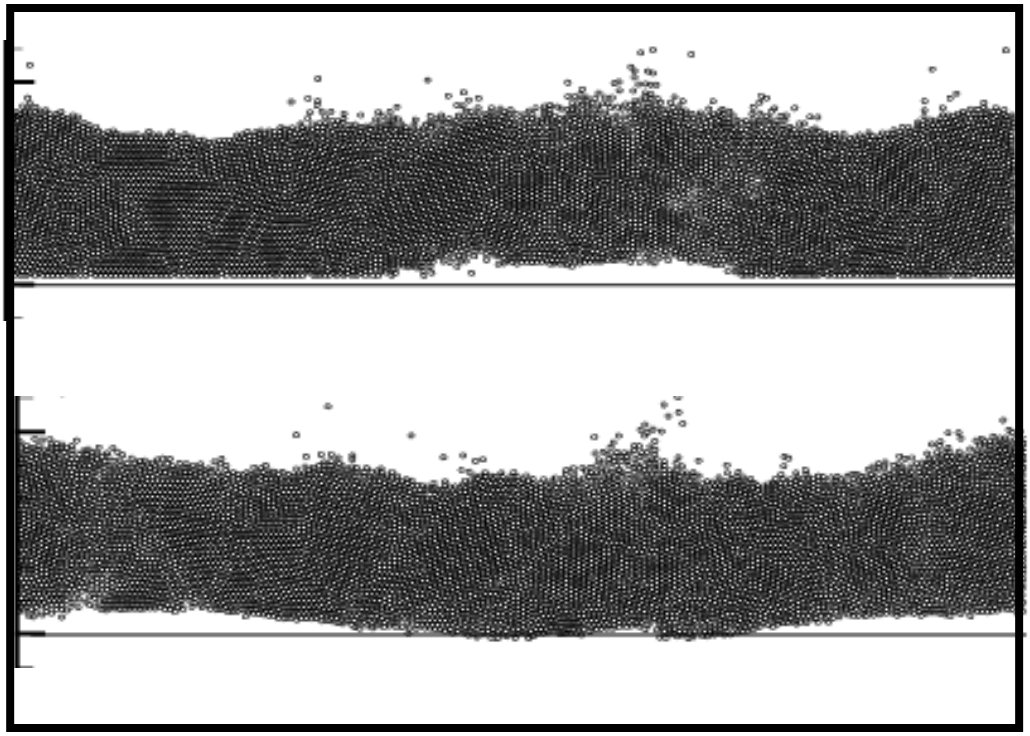

Figure 3.11. Illustrations showing the simulation results for kink formation. Two snapshots in the motion are shown. Simulation parameters are given in Table 3.3.

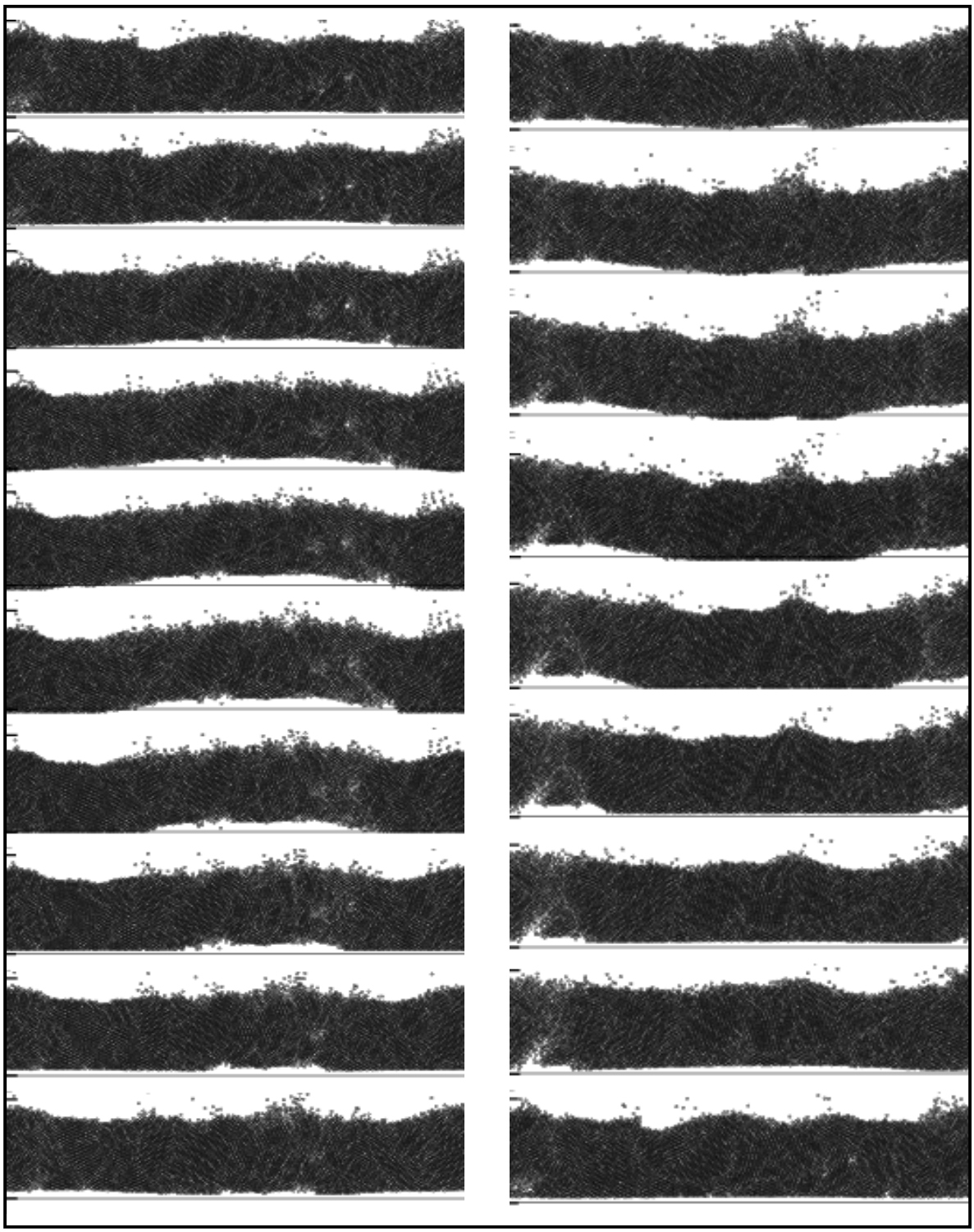

Figure 3.12. Kink cycle: In one wall cycle 8 kink shots are shown. The whole kink cycle takes 16 shots corresponding to an f/2 wave. Simulation parameters are as shown in Table 3.3.

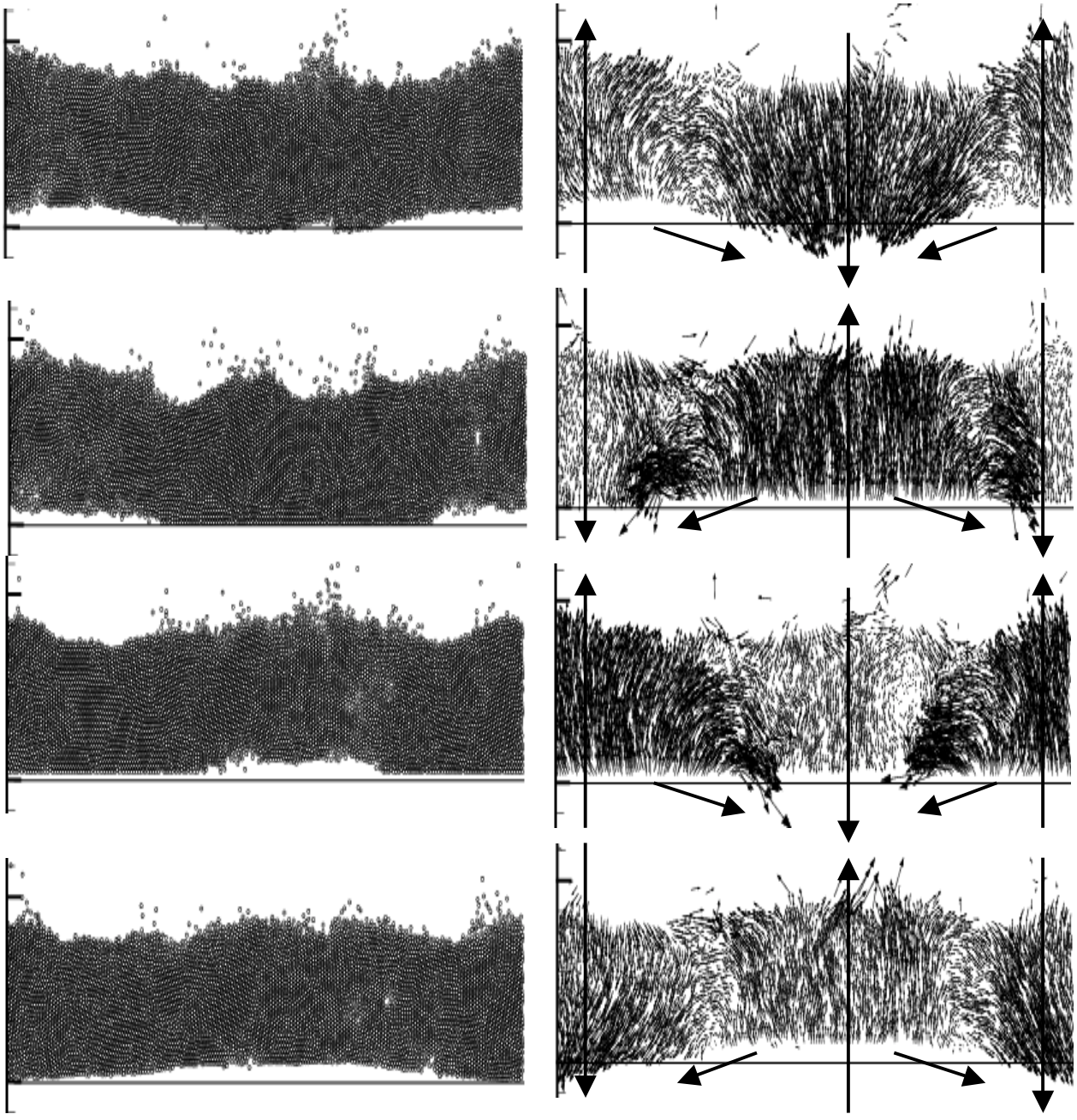

Figure 3.13. Illustration showing the kink shape and particle velocities at four different instances in a cycle. The velocity vectors and kink shapes are in accordance with the mechanism proposed by Douady *et al*., shown in Figure 3.5.

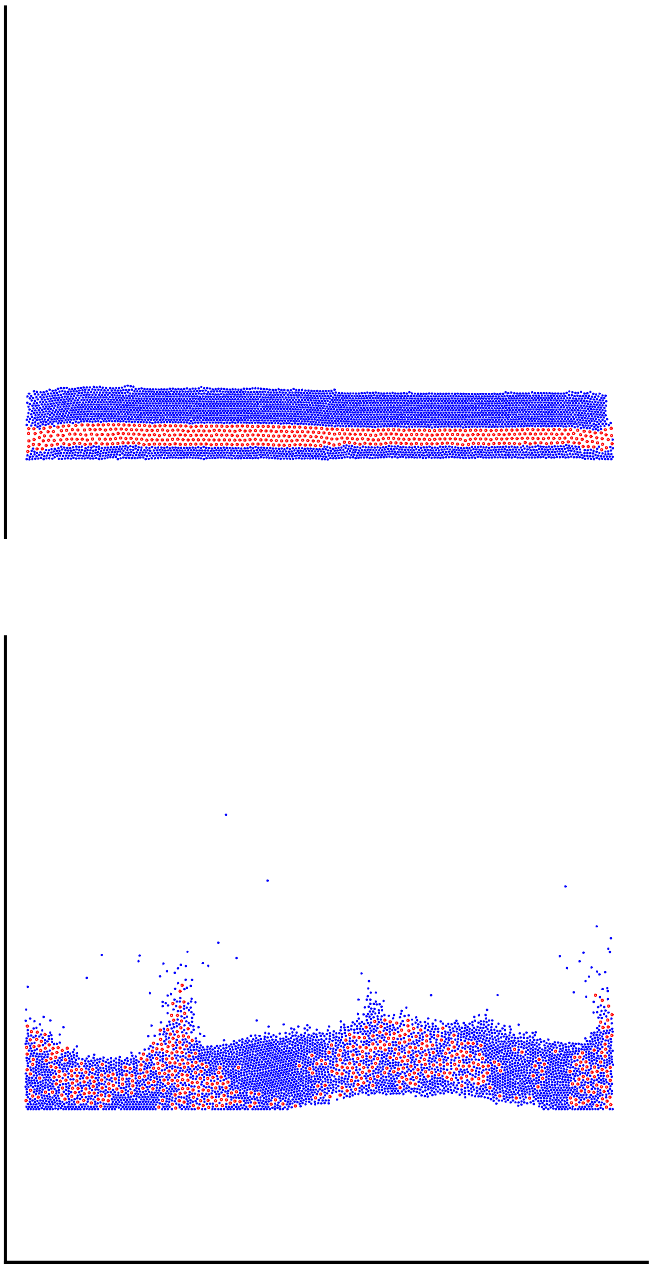

Figure 3.14. Illustrations showing the simulation results for kink formation in a binary mixture of size ratio 2. The two snapshots show initial setup and the segregated bed. Simulation parameters are given in Table 3.4.

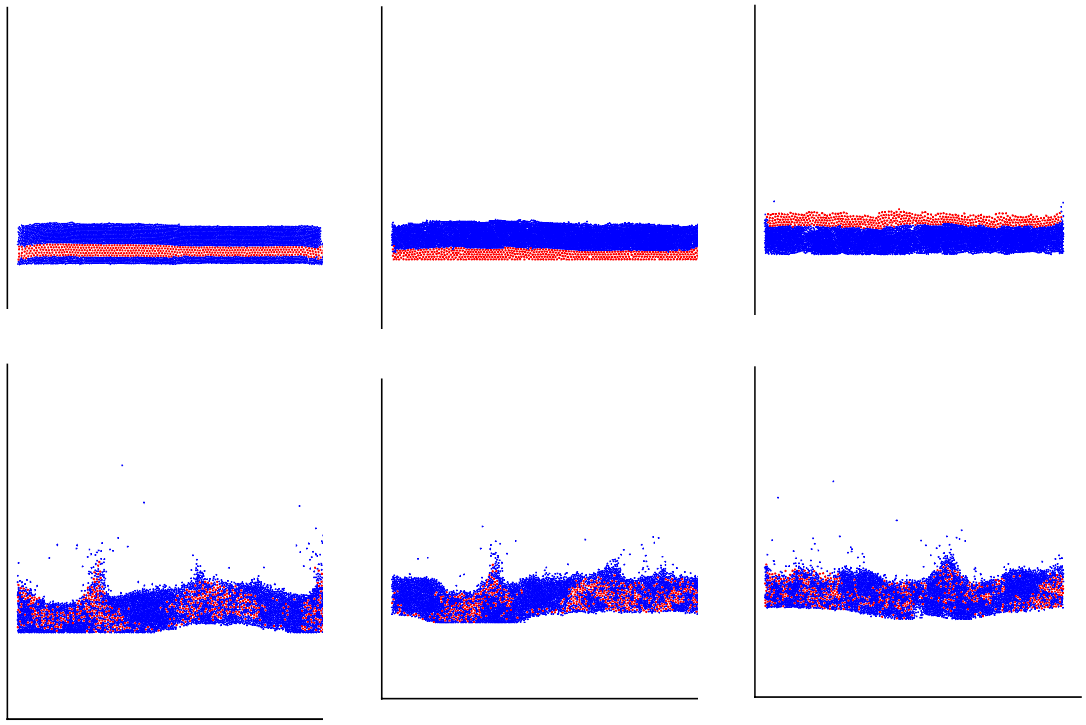

(a) (b) (c)

Figure 3.15. Illustrations showing the simulation results for kink formation in a binary mixture of size ratio 2. The two snapshots in (a), (b) and (c) show initial setup and the segregated bed. Simulation parameters are given in Table 3.4.

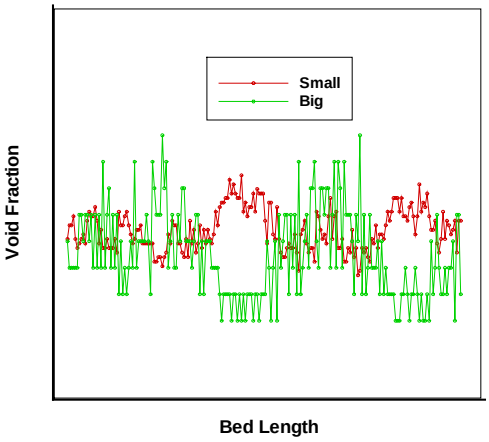

(a) Big particle layer sandwiched between small particle layers

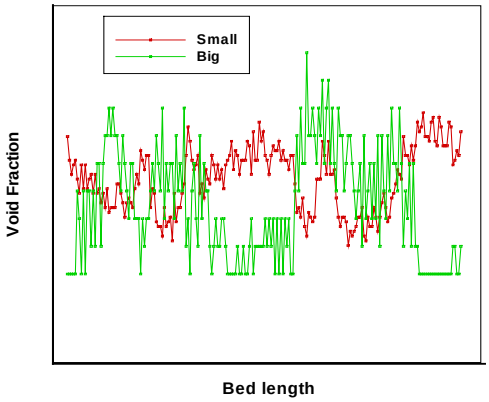

(b) Big particle layer below the small particle layer

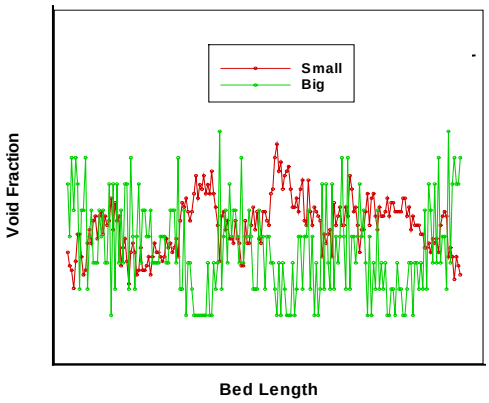

(c) Big particle layer on top of the small particle layer

Figure 3.16. Illustrations showing the volume fraction in the binary mixture (size ratio of 2) bed in kink regime.

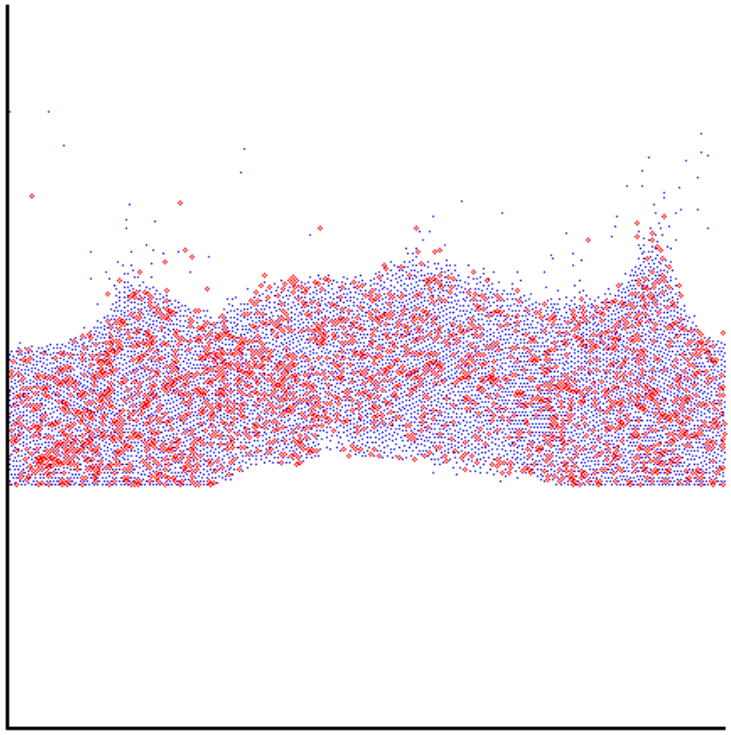

Figure 3.17. Illustrations showing the simulation results for kink formation in a vibrated granular bed of single sized particles. Thorough mixing of the particles can be seen.

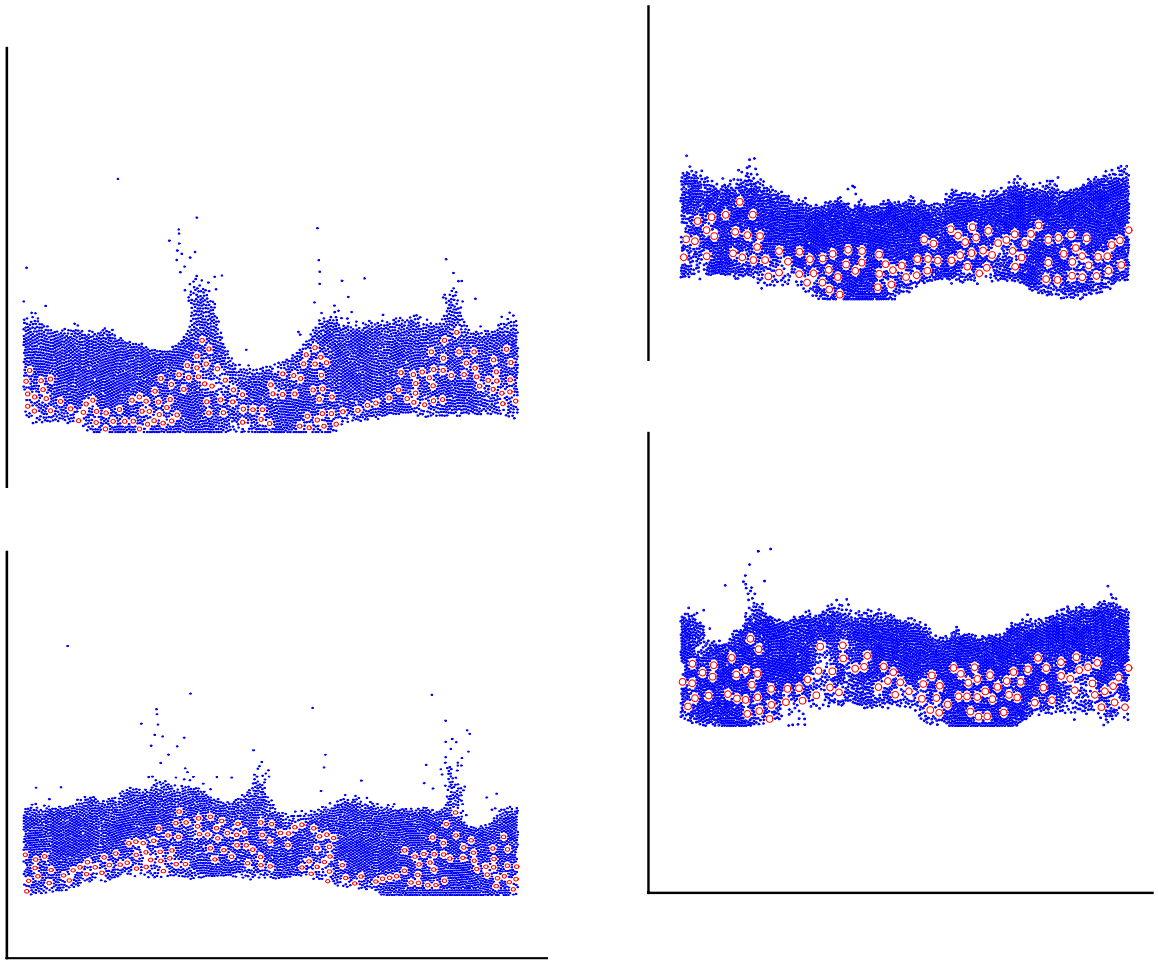

Figure 3.18. Illustrations showing the simulation results for kink formation in a binary mixture of size ratios (a) 3 and (b) 4. The two snapshots show initial setup and the segregated bed. Simulation parameters are given in Table 3.4.

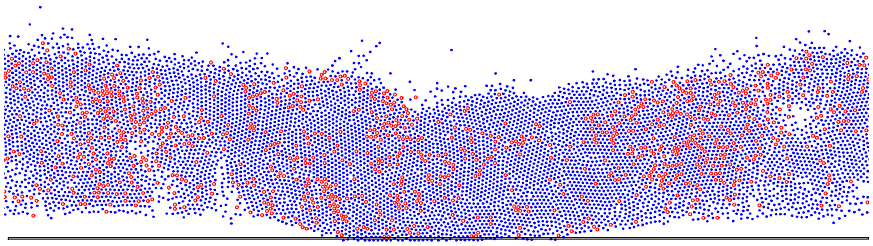

Figure 3.19. Illustrations showing the simulation results for kink formation in a vibrated binary mixture granular bed with same particle sizes but two different densities of ratio 1.75. Other simulation parameters are shown in Table 3.3. Thorough mixing of the particles can be seen.

Chapter 4

Gas-Solid Flows

Gas-solid flows have a number of applications in industry including fluidized bed transport, pneumatic transport of pharmaceutical powders and pellets, as well as in pulverized coal transport. The study of the dynamics of such a flow aids in better design of gas-particle systems. The analysis of gas-solid flows is complex because of the strong coupling between the solid and gas phases. The gas flows through the interstitial spaces or voids created by the particles, moving the particles and re-arranging the gas flow paths. The gas phase exerts a drag force on the solids; the solids exert an equal and opposite force drag on the gas. Furthermore, the pressure gradients created in the gas flow give rise to pressure forces on the particulate phase. Density differences between the two phases cause buoyancy driven flows. Thus the two phases exchange momentum and energy.

Coupling DES with computational fluid dynamics (CFD) offers a powerful way to understand gas-solid flow dynamics by accounting accurately for the interactions between the two phases. Each particle trajectory in the solid phase is computed using the discrete element method while the gas phase as a continuum. The inter-particle collision forces are computed using DES as explained and demonstrated in Chapters 2 and 3. The present chapter deals with the calculation of drag and pressure forces on each particle and the implementation of DES and gas-phase coupling. In the present formulation, we make no attempt to accurately resolve the flow around each particle because of the cost involved; the current formulation assumes that there are many solid particles in each fluid

cell. Instead, empirical drag correlations available in the literature are used. These correlations compute the drag based on the void fraction and gas-solid relative velocities and other governing parameters. Though a number of techniques for coupling the two phases have been published in the literature (Tsuji 1993, 2003; Xu and Yu 1997; Kuipers 2003), not all ensure that interaction forces are equal and opposite between the phases. When mass and energy are exchanged, these must be reciprocal as well, as shown in Fig. 4.1.

4.1. Governing Equations: Treatment of the Two Phases

The gas phase calculations are done using a continuum approach. In the present work the software MFIX (Multiphase Flow with Interphase eXchanges) which is a general-purpose computer program developed at NETL by Syamlal et al (Syamlal et al 1994a; Syamlal, 1994b; Syamlal, 1998) is used for the gas side continuum calculations. MFIX uses the kinetic theory approach (Lun et al. 1984; Syamlal et al 1988; Ding et al 1990) to solve for the solid phase. We first describe the governing equations in MFIX and then describe the changes due to the inclusion of DES. The governing continuity and momentum equations for the two phases are given below. Procedures for their numerical solution are given in Appendix A.

4.1.1 Continuity Equation

Gas Continuity Equation:

$$\frac{\partial}{\partial t}(\varepsilon_g \rho_g) + \nabla \cdot (\varepsilon_g \rho_g \vec{v}_g) = \sum_{n=1}^{N_g} R_{gn} \tag{4.1}$$

Solids Continuity Equation (m^{th} solids-phase):

$$\frac{\partial}{\partial t}(\varepsilon_{sm}\rho_{sm}) + \nabla\cdot(\varepsilon_{sm}\rho_{sm}\vec{v}_{sm}) = \sum_{n=1}^{N_{sm}} R_{smn} \tag{4.2}$$

The first term on the left in equation (4.1) and (4.2) accounts for the rate of mass accumulation per unit volume, and the second term is the net rate of convective mass flux. The term on the right accounts for interphase mass transfer because of chemical reactions or physical processes such as evaporation.

4.1.2 Momentum Equation

Gas Momentum Equation:

$$\frac{\partial}{\partial t}(\varepsilon_g\rho_g\vec{v}_g) + \nabla\cdot(\varepsilon_g\rho_g\vec{v}_g\vec{v}_g) = \nabla\cdot\bar{\bar{S}}_g + \varepsilon_g\rho_g\vec{g} - \sum_{m=1}^{M}\vec{I}_{gm} + \vec{f}_g \tag{4.3}$$

Here $\bar{\bar{S}}_g$ is the gas-phase stress tensor, $\vec{I}_{gm}$ is an interaction force representing the momentum transfer between the gas phase and mth solids phase, and $\vec{f}_g$ is the flow resistance offered by internal porous surface.

Solids Momentum Equation (mth solids-phase):

$$\frac{\partial}{\partial t}(\varepsilon_{sm}\rho_{sm}\vec{v}_{sm}) + \nabla\cdot(\varepsilon_{sm}\rho_{sm}\vec{v}_{sm}\vec{v}_{sm}) = \nabla\cdot\bar{\bar{S}}_{sm} + \varepsilon_{smg}\rho_{sm}\vec{g} + \vec{I}_{gm} + \sum_{\substack{l=0 \\ l\neq m}}^{M}\vec{I}_{ml} \tag{4.4}$$

Here $\bar{\bar{S}}_{sm}$ is the stress tensor for mth solids phase. The term $\vec{I}_{ml}$ is the interaction force between the mth and lth solids phases. The first term on the left represents the net rate of momentum increase and the second the usual convective term. The first term on the right represents forces due to the stress tensor, while the second term represents body forces (gravity in this case). The last two terms in equation (4.4) represent the momentum

exchange between the fluid and solids phases and between the different solids phase, from left to right.

The interaction forces considered are the buoyancy and drag forces and momentum transfer due to mass transfer, since those are the most significant forces for fluidized bed applications. Thus, the fluid-solids interaction force is written as

$$\vec{I}_{gm} = -\varepsilon_g \nabla P_g - F_{gm}(\vec{v}_{sm} - \vec{v}_g) - R_{0m}[\xi_{0m}\vec{v}_{sm} + \bar{\xi}_{0m}\vec{v}_g]$$

where the first term on the right side describes the buoyancy force, the second term describes the drag force, and the third term describes the momentum transfer due to mass transfer. R_{0m} is the mass transfer from the gas phase to solids phase-m where

$$\xi_{0m} = \begin{cases} 1 & for\ R_{0m} < 0 \\ 0 & for\ R_{0m} \geq 0 \end{cases}$$

and $\bar{\xi}_{0m} = 1 - \xi_{0m}$

The solids-solids momentum transfer $\vec{I}_{ml}$, is represented as

$$\vec{I}_{ml} = -F_{sml}(\vec{v}_{sl} - \vec{v}_{sm}) + R_{ml}[\xi_{ml}\vec{v}_{sl} + \bar{\xi}_{ml}\vec{v}_{sm}]$$

where R_{ml} is the mass transfer from the solids phase-m to solids phase-l,

$$\xi_{ml} = \begin{cases} 1 & for\ R_{ml} < 0 \\ 0 & for\ R_{ml} \geq 0 \end{cases}$$

and $\bar{\xi}_{ml} = 1 - \xi_{ml}$

The gas-solid drag correlation for F_{sml} is derived from correlations relating the terminal velocity in fluidized or settling beds with void fraction and Reynolds number. Details may be found in (Syamlal et al 1994a).

The solids stress tensor is required to close the above equation set. The kinetic theory relations used in MFIX for computing the solids stress, including expressions for

the solids pressure and the granular temperature, may be found in (Syamlal et al 1994a). The solids stress tensor calculations are not required in the present work as the kinetic theory for solid phase calculations is replaced by DES. In the present work Eqns. (4.2) and (4.4) are also eliminated in favor of a discrete element formulation. Thus, the solids volume fraction and solids velocity are directly computed by using DES to find particle velocities and positions, and locating the particles in the computational cells for the gas. The procedures for doing this are described below.

4.2. Coupling DES with Continuum Simulations

4.2.1. Interphase Drag Force Calculation

Though a variety of interaction forces couple the gas and solid (Basset force, Magnus lift force, drag force etc.) the focus of the present work is on the simulation of gas-particle flows for fluidized bed applications. Two primary interaction forces which are dominant for this application, interphase drag, and pressure force/buoyancy, are considered. The calculation domain is discretized into cells suitable for the fluid calculation. Typically, a fluid cell must contain many particles so as to be consistent with the volume averaging concept used in the gas phase. Since the gas-phase mesh is much larger than the individual particle, it is not possible to resolve the drag numerically. The interphase drag is computed from experimental correlations for fluidized beds.

The drag force is expressed in the form:

$$F_D = F_{gs}(V_s - V_g)$$

as a product of a gas-solid drag coefficient and the interphase velocity difference, where V_s is the solid velocity and V_g is the gas velocity. Various researchers have given

empirical formulae to calculate the drag coefficient F_{gs}. We consider a few important contributions in turn.

The Ergun equation (1952) is a widely know gas-solid drag formula which is typically applied to packed beds as the correlation is generated using packed bed pressure drop data. But for low volume fraction calculations the Ergun equation is inadequate. An alternative drag correlation is then required.

Terminal velocity analysis in a fluidized bed or a settling bed is an alternative for the inadequacy of Ergun equation. The terminal velocity is expressed as a function of void fraction and Reynolds number (Richardson and Zaki 1954, cited by Syamlal et al 1994a). Syamlal and O'Brien (1994a) derived a following formula for converting terminal velocity correlations to drag correlations and have implemented it in MFIX. The drag correlation MFIX uses is:

$$F_{gs} = \frac{3}{4}\frac{\varepsilon_s \varepsilon_g \rho_g}{V_{rm}^2 d_{pm}} C_{DS}\left(\frac{\mathrm{Re}_m}{V_{rm}}\right)\left|V_{sm} - V_g\right| \qquad (4.5)$$

where V_{rm} is the terminal velocity correlation for the mth solid phase. It cannot be derived an explicit formula and can only numerically be calculated from the Richardson and Zaki correlation. Garside and Al-Dibouni[(1977) developed a correlation which can be used to calculate V_{rm}.

$$V_{rm} = 0.5(A - 0.06\,\mathrm{Re}_m + \sqrt{0.06\,\mathrm{Re}_m)^2 + 0.12\,\mathrm{Re}_m(2B - A) + A^2})$$

where

$$A = \varepsilon_g^{4.14}$$

$$B = \begin{cases} 0.8\varepsilon_g^{1.28} & \text{if } \varepsilon_g \le 0.85 \\ \varepsilon_g^{2.65} & \text{if } \varepsilon_g > 0.85 \end{cases}$$

and the Reynolds number of the mth solids phase is given by,

$$\mathrm{Re}_m = \frac{d_{pm}\left|\vec{v}_{sm} - \vec{v}_g\right|\rho_g}{\mu_g}$$

Here, $C_{DS}(\frac{\mathrm{Re}_m}{V_{rm}})$ is the single-sphere drag function. Of the numerous expressions available for CDS, MFIX chose the following simple formula proposed by Dalla Valle (1948),

$$C_{DS}(\mathrm{Re}) = (0.63 + \frac{4.8}{\sqrt{\mathrm{Re}}})^2$$

Tsuji et al (1993, 2003) have used

$$F_{gs} = \frac{\mu(1-\varepsilon)}{d_p^2 \varepsilon}\left[150(1-\varepsilon) + 1.75\,\mathrm{Re}\right] \quad \text{when } \varepsilon \le 0.8 \text{ and}$$

$$F_{gs} = \frac{3}{4} C_D \frac{\mu(1-\varepsilon)}{d_p^2}\varepsilon^{-2.7}\,\mathrm{Re} \quad \text{when } \varepsilon \rhd 0.8$$

where ε is the void fraction and Re the Reynolds number.

$$C_D = 24(1 + 0.15\,\mathrm{Re}^{0.687})/\mathrm{Re} \quad \text{when } \mathrm{Re} \le 1000 \text{ and}$$

$$C_D = 0.43 \text{ when } \mathrm{Re} \rhd 1000$$

$$\mathrm{Re} = \frac{\left|\vec{u}_s - \vec{u}_g\right|\rho\varepsilon d_p}{\mu}$$

Kuipers et al (2003) have summarized a number of drag correlations which are now described. The drag force on a single particle in an infinite flow is given by

$$F_s = C_d \frac{1}{8}\pi d_p^2 \rho_f \left|\vec{v}_s\right| \vec{v}_s$$

The drag force on a single particle in a particulate flow is given by

$$F_s = C_d \frac{1}{8}\pi d_p^2 \rho_f \left|\vec{u}_s - \vec{u}_g\right| \left(\vec{u}_s - \vec{u}_g\right) f(\varepsilon)$$

where $C_D = 24(1+0.15\,\mathrm{Re}^{0.687})/\mathrm{Re}$ when $\mathrm{Re} \le 1000$ and

$$C_D = 0.43 \text{ when } \mathrm{Re} \rhd 1000 \text{; here } \mathrm{Re} = \frac{\left|\vec{u}_s - \vec{u}_g\right| \rho \varepsilon d_p}{\mu}$$

Different forms of the function $f(\varepsilon)$ have been used by different researchers. These are given below.

<u>Wen and Yu (1996):</u>

$$f(\varepsilon) = \varepsilon^{-4.7}$$

<u>Felice (1994):</u>

$$f(\varepsilon) = \varepsilon^{-\alpha}$$

$$\alpha = 4.7 - 0.65 \exp\left[-\frac{(1.5 - \log \mathrm{Re})^2}{2}\right] \text{ when } 2 \lhd \mathrm{Re} \lhd 500$$

<u>Happel (1958):</u>

$$f(\varepsilon) = \frac{3 + 2(1-\varepsilon)^{5/3}}{3 - 4.5(1-\varepsilon)^{1/3} + 4.5(1-\varepsilon)^{5/3} - 3(1-\varepsilon)^2}$$

In all the above mentioned formulae, ε is the void fraction, Re is the Reynolds number, $\vec{u}$ is the velocity vector, ρ_f is the gas density and d_p is the particle diameter.

Many DES time steps are done during a fluid time step. After the completion of the DES time stepping, the solid particles are located on the fluid background mesh. The void fraction and the averaged solid velocities in each fluid cell are computed. This information is used to calculate the gas-solid drag force in each cell using any of the above mentioned drag correlations. The net drag on the solid phase in each cell is equal to the net drag on the gas phase in the cell. The net solids drag is distributed to each particle in the cell based on the ratio of the particle volume to total solid volume in the cell. If V_{ijm} is the volume of a particle *i* of solid phase *m* in the cell *j*, and F_{Dj} is the total drag force on the solid mass of volume V_s in the cell, the drag F_{Dijm} on the particle is given by

$$F_{Dij} = F_{Dj}\left(\frac{\sum V_{pijm}}{V_s}\right)\left(\frac{V_{pijm}}{\sum V_{pijm}}\right)$$

For a single solid phase and same sized particles,

$$F_{Dij} = F_{Dj}\left(\frac{1}{N}\right)$$

where N is the number of particles in the cell.

4.2.2. Void Fraction Calculation

To calculate the drag force on the solid mass in each cell, the value of the void fraction in the cell must be known. The domain is meshed into computational cells for the fluid continuum calculations. In the flow at every time step particles enter and leave a cell. Each particle from the DES simulation must be located within the fluid control volume; the sum of all particle volumes in the cell yields the solid volume fraction. It is useful to

find the cell values of solids volume fraction and velocity classified by particle size. This requires the computation of several solids volume fractions per cell.

If V_{pimj} is the volume of a particle of index *i* of a size representing phase *m* in a fluid cell *j*, then the total solid volume V_{smj} of the phase *m* in the cell *j* is

$$V_{smj} = \sum_i V_{pimj}$$

The corresponding volume fraction is then given by

$$\varepsilon_{smj} = \frac{V_{smj}}{V_j} \text{ where the cell volume } V_j = \Delta x \Delta y \Delta z$$

where Δx is the length of the cell in x-direction, Δy is the length of the cell in y-direction and Δz is the depth of the cell in Z-direction. For 2-dimensional simulations, Δz is taken as one particle diameter in Cartesian coordinates and as one radian in cylindrical coordinates.

The total solids volume fraction in the cell is given by the sum of the solids volume fractions of each phase in the cell

$$\varepsilon_{sj} = \sum_m \varepsilon_{smj}$$

Since the sum of the various solids volume fractions and the fluid volume fraction must be equal to unity, the j^{th} cell void fraction ε_j can then be obtained from the solids volume fraction as:

$$\varepsilon_j = 1 - \varepsilon_{sj}$$

Once the volume fraction is made available to MFIX, blockage effects are automatically taken care of.

4.2.3. Solids Velocity Calculation

Another variable required in the drag force calculation is the solid velocity of each particle size group in each fluid cell. DES gives the velocity of each individual particle at the end of every solid time step. The particle velocities must be averaged in each cell to obtain a representative cell solid velocity. In the present work, the volume-averaged solid velocity is computed and stored at the cell centers.

If U_{pimj} is the velocity of particle *i* of solid phase *m* in cell *j*, then the volume averaged solid velocity U_{smj} of phase *m* in the cell is given by

$$U_{smj} = \frac{\sum_i V_{pimj} U_{pimj}}{V_{smj}}$$

This value is used in the calculation of the drag force. It should be noted that the value thus obtained is a cell-center value where as the numerical scheme follows the convention of velocities stored at the face center. To obtain the face center value the corresponding neighbor cell center values are weighted averaged across the face.

4.2.4 Pressure Force Calculation

The other important force that is exerted by the gas on the solid particles is the pressure force/buoyancy. At every fluid time step the gas side continuum equations are solved and the gas side quantities like gas velocity and pressure are obtained. Pressure is stored at the cell center. Thus the pressure exerted by the gas in each cell is obtained and stored at its center. Correspondingly, a pressure force is exerted by the gas on all the solid particles in that cell. The pressure force on the cell in a given direction is the difference of the pressure on the faces of the cell normal to the direction, times the average cross

sectional area of the cell normal to the direction. Consider a cell and the pressure force on the cell in one dimension (in y-direction) as shown in Figure 4.3. Let the cell dimensions be Δx, Δy, Δz in the x, y and z directions respectively. The pressure in the cell is P_p. The pressures in the north and south cells are P_n and P_s respectively. Then the pressure on the north face would be $P_1 = \frac{P_n + P_p}{2}$ and the pressure on the south face would be $P_2 = \frac{P_s + P_p}{2}$. The y-direction pressure force on the cell would be $P_c = (P_2 - P_1)\Delta x \Delta z$ (Δz for a Cartesian analysis is the diameter of the particle itself). It should be noted that the pressure averaging across the cells done so far is done assuming structured uniform mesh for simplicity of explanation. For non-uniform meshes weighted averaging should be done based on the cell dimensions. This pressure force should be distributed to all the particles in the cell. For a particle *j* of solid phase *m* in the cell, the pressure force P_{jm} is given by

$$P_{jm} = \varepsilon_m P_c \frac{V_j}{V_m}$$

where $\varepsilon_m = \frac{V_m}{\Delta x \Delta y \Delta z}$ is the solid volume fraction of the phase, V_j is the volume of the particle and V_m is the total volume of the solid phase in the cell.

It can be seen that for a static fluid, if the north and south cells considered were at heights h_1 and h_2, $h_2 - h_1 = \Delta y$, then P_{jm} would be

$$P_{jm} = \varepsilon_m P_c \frac{V_j}{V_m} = \frac{V_m}{\Delta x \Delta y \Delta z}\left(P_2 - P_1\right)\Delta x \Delta z \frac{V_j}{V_m}$$

$$P_{jm} = \frac{V_m}{\Delta x \Delta y \Delta z}\rho g\left(h_2 - h_1\right)\Delta x \Delta z \frac{V_j}{V_m} = \frac{V_m}{\Delta x \Delta y \Delta z}\rho g \Delta x \Delta y \Delta z \frac{V_j}{V_m}$$

$$P_{jm} = \rho g V_j$$

Here, ρ is the gas density. Combined with the $-\rho_s g$ term in the particle equation of motion, the buoyant force on the particle is obtained.

4.2.5 Coupling Algorithm for Gas-Solid Flows: Time Step

The intent of the present work is to use a sequential and iterative procedure for coupling the two calculations. Due to the limitations in the soft sphere model the solid time steps typically are very small because of the high stiffness constants. We wish to use far larger time-steps for the gas than for the solid, since the gas has no explicit time-stepping limitations. At every gas-phase time-step, several DES sub-steps are taken. The volume fraction and averaged solid velocity are computed at the end of the sub-steps. The gas flow is assumed stationary at the old values during this sub-stepping. Then the gas flow is iterated to convergence within the time step. The procedure is repeated until the desired time interval is covered.

Figure 4.2 shows a flow chart of the coupling procedure described thus far.

4.3. Validation of DES-Gas Phase Coupling

4.3.1. Fluidized Bed Validation

The method developed has been validated for a few simple cases using analytical solutions. These simple tests ensured that momentum was being conserved and that particle buoyancy and terminal velocity were being correctly computed; the results are not presented here. We also computed gas-particle flows in a fluidized bed for comparison with the published results of Tsuji et al (1993, 2003) and Xu and Yu (1997). The results compared satisfactorily; details are presented below.

A fluidized bed is a gas-particle system used for large-scale chemical reactions. Typically it is a cylinder containing particles, which act as chemical catalysts. Gas is injected from the bottom of the chamber. The particles float freely and move in the flow thus mixing well and aiding the necessary chemical reactions. A good understanding of the behavior of the system is important for better design of the fluidized bed.

For validating the DES-MFIX coupled code, two-dimensional simulations have been performed with the intention of reproducing the work of Tsuji et al (1993) and Xu and Yu (1997). Tsuji et al (1993) had experimentally validated their simulations. In order to accurately perform a two-dimensional experiment they confined the gas flow between two parallel plates with a gap to fit one layer of particles. The walls in contact with the particles have been made with negligible friction. Bubble formation frequency, pressure drop across the bed and bed dynamics were recorded. Simulations were performed to reproduce the experiment and satisfactory comparisons between the two were reported.

4.3.1.1. Fluidized Bed Simulation Parameters

Two-dimensional simulations have been performed. All the simulation parameters are taken from Tsuji (1993). A chamber of 15 cm width and 90 cm height has been simulated. The particle bed height at rest is 22 cm. A single central jet of air is injected from the bottom wall. 2400 spherical particles of 4 mm diameter each have been used. The minimum fluidization velocity of this system is about 1.85 m/s. Simulations have been performed for various superficial gas velocities ranging from 2 m/s to 2.6 m/s. Other simulation parameters are listed in Table 4.1. The flow field was divided into 15X50 rectangular cells of 10X20 mm (width and height) each. In a packed condition roughly about 9 particles would fit in each cell. MFIX drag correlation is used for the purpose.

It is important to correctly resolve the depth dimension when doing two-dimensional gas-solid computations. In the present work, the drag correlations used for gas-particle interaction assume spherical particles rather than cylinders. The depth of the computational domain is taken to be equal to the diameter of the particle. Both gas and particles are confined to move only in the plane of the calculation.

4.3.1.2. Fluidized Bed Simulation Results

At low inlet jet velocities the bed expands but no circulation is observed. As the inlet jet velocity increases the particles in the center rise and slug formation can be noticed. At higher inlet jet velocities, formation of a bubble takes place pushing down the particles at the walls and rising in the center. Thus we get two circulation zones on either side of the bubble path in the center. At much higher inlet jet velocities, the center particles rise fast and almost burst out of the top surface, falling on either side and

moving down along the walls. This is known as the spouting phenomenon. Substantial mixing occurs in the higher inlet jet velocity cases. The above mentioned dependence on the inlet jet velocity has been observed in the simulations for superficial gas velocity ranging from 2 to 2.6 m/s. The bubbling phenomenon can be seen at superficial gas velocity of 2.6 m/s and is shown in Figures 4.4. (a), (b) and (c). The particle motion as well as the corresponding velocity vectors are shown. The particles have been colored in layers of red and blue to show mixing and particle paths. Pressures values and pressure drops across the bed at various heights from the bed floor have been computed and are shown in Figures 4.7. and 4.8. Tsuji et al (1993) reported a pressure drop range of roughly 2000 Pa across the bed (Figure 4.9). It can be seen in Figures 4.7 and 4.8 that the present simulations also report a pressure drop range of 2000 Pa across the bed. The large pressure fluctuations in a fluidized bed are caused by bubbles and slugs that form and collapse at regular intervals. From the various pictures and times shown in Figures 4.5 (a) and (b) it can be seen that bubble forms at roughly a frequency of 2 per second, *i.e.*, a bubble forms and collapses every half a second. Ten snapshots of the fluidized bed between the third and fourth second show the rise an fall of two bubbles. The ten snap shots are equi-spaced at 0.1 seconds. This shows that the bubbling frequency is roughly 2 per second. From Figures 4.7. and 4.8 also, it can be seen that the pressure fluctuation frequency is again about 2 per second thus supporting the idea that bubbles are a major cause for the large pressure fluctuations in a fluidized bed. It has been reported from experiments that the bubble does not rise upward along the central axis of the column. It sways laterally, leaving an “S” shaped wake. This has also been captured in the present simulations as can be seen in Figures 4.4., 4.5 and 4.6. In Figures 4.6 (a) and (b) the local

velocity vectors are shown along with the particles. An insight into the particle motion and the velocity change can be obtained from Figures 4.6. (a) and (b) which show the collapse of a bubble and its re-formation. Most of the mixing occurs away from the base where there is more fluidization and hence more circulation. Near the base and the walls the particles become consolidated and do not mix with the flow. Overall, the predicted flow patterns, time scales and velocities match those of Tsuji et al (1993) relatively well.

4.3.1.3. Computational Time

Simulations of fluidized beds with about 2400 particles, took about 1-2 days elapsed time t simulate 10 seconds. The computer used was a PC with a 1.7 GHz Pentium 4 processor with 2 Gb RAM. The time required in the case of a fluidized bed is smaller than the time required for pure DES simulations shown in Chapter 3. This is primarily because (i) fewer particles are simulated in a fluidized bed case (ii) the particle size is 4mm as opposed to 1mm in vibrated beds (the particle mass scales as d^3) (iii) the spring constants used are roughly $1/5^{th}$ those used in vibrated bed cases. The above reasons contribute to the solid time step for the fluidized bed case, which is bigger by about two orders of magnitude than the one for vibrated beds.

4.3.2. Fluid-Solid Driven Cavity Validation

A fluid-solid top wall driven cavity has been simulated for 40 seconds of flow The simulation parameters are shown in Table 4.2. The domain is a square box of 3cmX3cm dimension. The top wall is pulled in the positive x-direction with a velocity of 3cm/s. The Reynolds number for the simulation is chosen to be 100. 300 particles of 1

mm diameter are initially stacked on the bottom wall of the cavity. The particle and fluid densities are kept equal and the simulation is done for the zero gravity condition. The instantaneous particle positions and velocities of the 300 particles used in the flow are shown in Figure 4.10. Clearly a closed loop flow can be seen. It can also be noticed that the velocities are minimal near the left bottom corner and right bottom corner of the cavity in regions where the fluid is stagnant. Also the flow cell is pushed more to the right of the cavity as the top wall is pulled in the positive x-direction. Due to the same reason, the core of the loop where the fluid and particle velocity would be negligible is also shifted more to the top right of the cavity. This can be seen in Figure 4.11 (a), where the trajectory of 12 particles is shown by interconnecting their instantaneous velocities. In Figure 4.11. (b) the trajectory of 12 particles is shown by plotting the instantaneous particle positions during the simulation time of t = 0s to t = 40s.

4.4. Closure

Important aspects of the solution methodology for gas-solid flow simulations have been presented in this chapter. Governing equations for the gas phase have been presented. The solid phase is solved using the DES presented in Chapters 2 and 3. The solution procedure for gas continuum equations involves a finite volume discretization with second-order schemes for convection and diffusion terms and is described in Appendix A. The gas-solid coupling methodology has been described in detail. The drag force formulation, based on the available empirical correlations, has been explained. The procedures for determining the solid void fraction and solid velocity to compute the drag force have been discussed. The procedure for coupling multiple time steps of the particle

simulation with large time steps for the gas-phase simulation has been explained. The methodology has been validated against published simulations of fluidized beds reported in literature. Benchmarked 2-dimenaional bubbling fluidized bed simulations are done. The macro quantities like the bed pressure drop and the bubbling frequency reported experimentally and numerically have been computed and compared. The agreement has been found to be satisfactory. A top wall driven cavity has also been simulated and a qualitative analysis of the results shows satisfactory performance. The code can now be used to simulate newer and more complex cases for better understanding of gas-solid flows. The next chapter shows the application of the code in analyzing drag-correlation used and in simulating fluidized beds with binary mixtures.

Table 4.1. Simulations parameters used to validate the fluidized bed simulations against Tsuji (1993)

Bed Dimensions (W X H)	150 mm X 900 mm
Fluid mesh size	15 X 50
Cell dimensions	10 mm X 20 mm
Particle bed height at rest	220 mm
Minumum fluidization velocity	1.8 m/s
Inlet jet velocity	2.6 m/s
Number of Particle: N	2400
Particle diameter: d	4mm
Particle density: ρ_s	2700 kg/m^3
Gas density: ρ_g	1.205*10^{-3} kg/m^3
Gas viscosity: μ_g	1.80*10^{-5} N/m^2
Particle coeff. Of restitution: ε	0.9
Particle stiffness coeff: k	800 N/m
Particle damping coeff: v	0.18 (N.s)/m
Particle friction coeff: μ_f	0.3
Ratio of fluid time step to particle time step: $\frac{\Delta t_f}{\Delta t_s}$	$\frac{5*10^{-3}}{2*10^{-4}} = 25$

Table 4.2. Simulations parameters for fluid-solid driven cavity simulations

Box Dimensions (W X H)	3 cm X 3 cm
Fluid mesh size	25 X 25
Top wall velocity	3 cm/s
Number of Particles: N	300
Reynold's number: Re	100
Particle diameter: d	1 mm
Particle density: ρ_s	750 kg/m^3
Gas density: ρ_g	750 kg/m^3
Gas viscosity: μ_g	0.675 N/m^2
Particle coeff. Of restitution: ε	0.9
Particle stiffness coeff: k	800 N/m
Particle damping coeff: v	0.18 (N.s)/m
Particle friction coeff: μ_f	0.3
Ratio of fluid time step to particle time step: $\frac{\Delta t_f}{\Delta t_s}$	$\frac{5*10^{-3}}{5*10^{-5}} = 100$

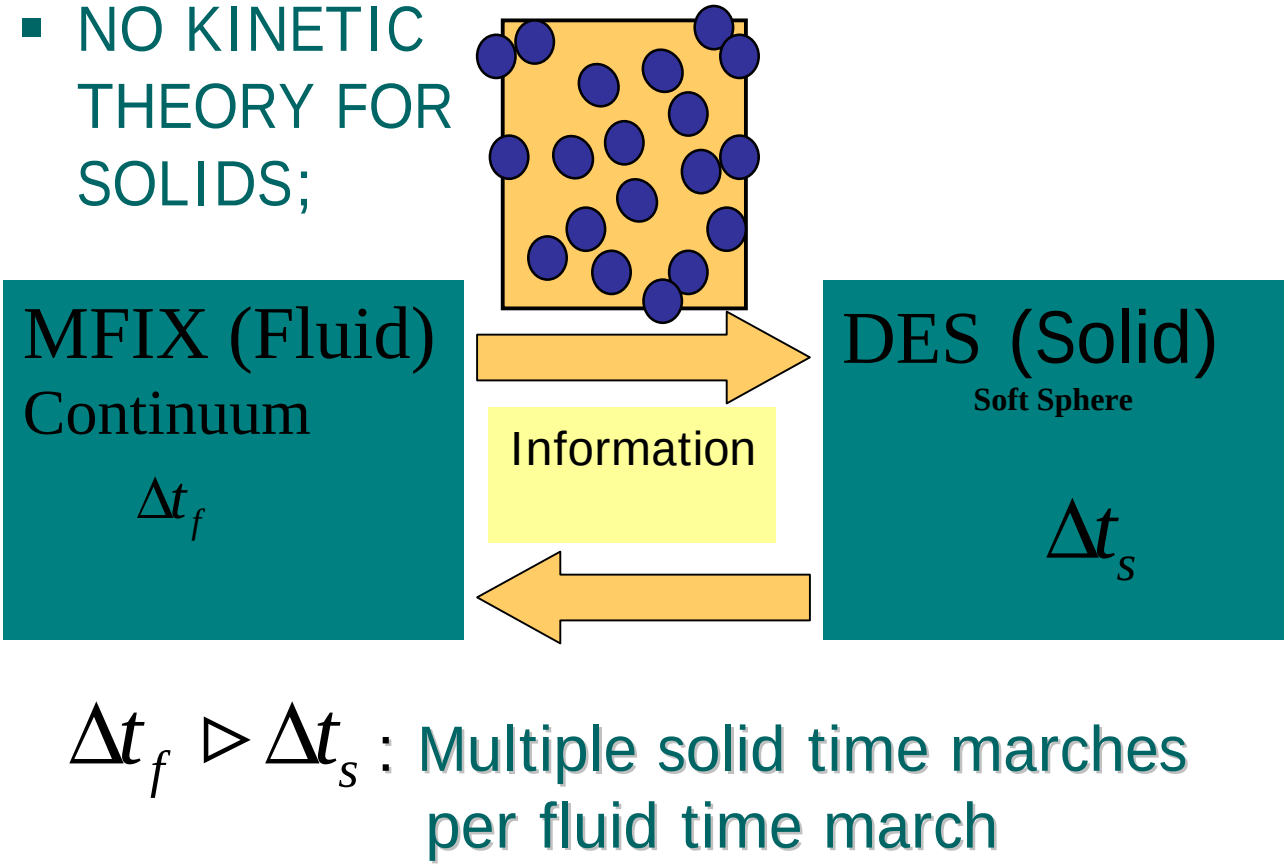

Figure 4.1. Gas-solid coupling scheme

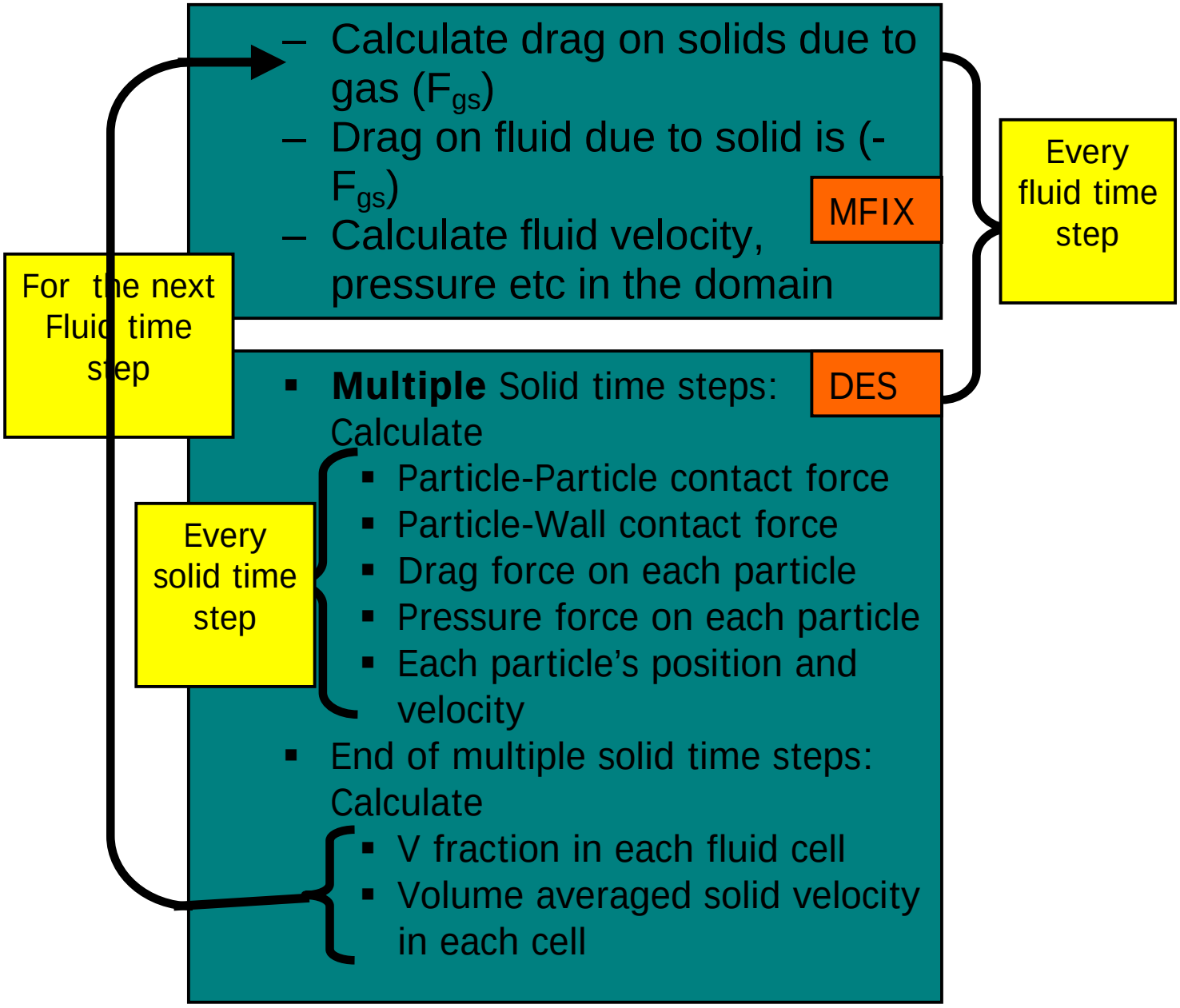

Figure 4.2. Flowchart for MFIX-DES coupling

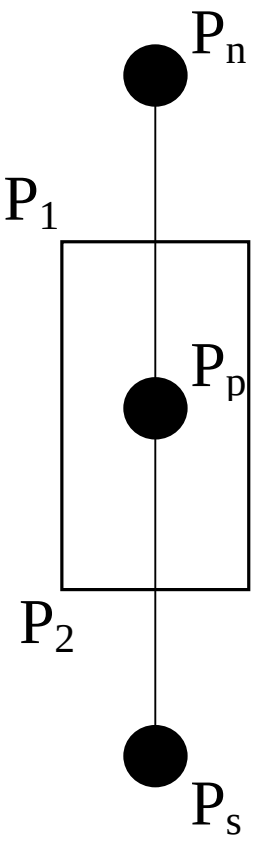

Figure 4.3. Illustration for pressure force calculation

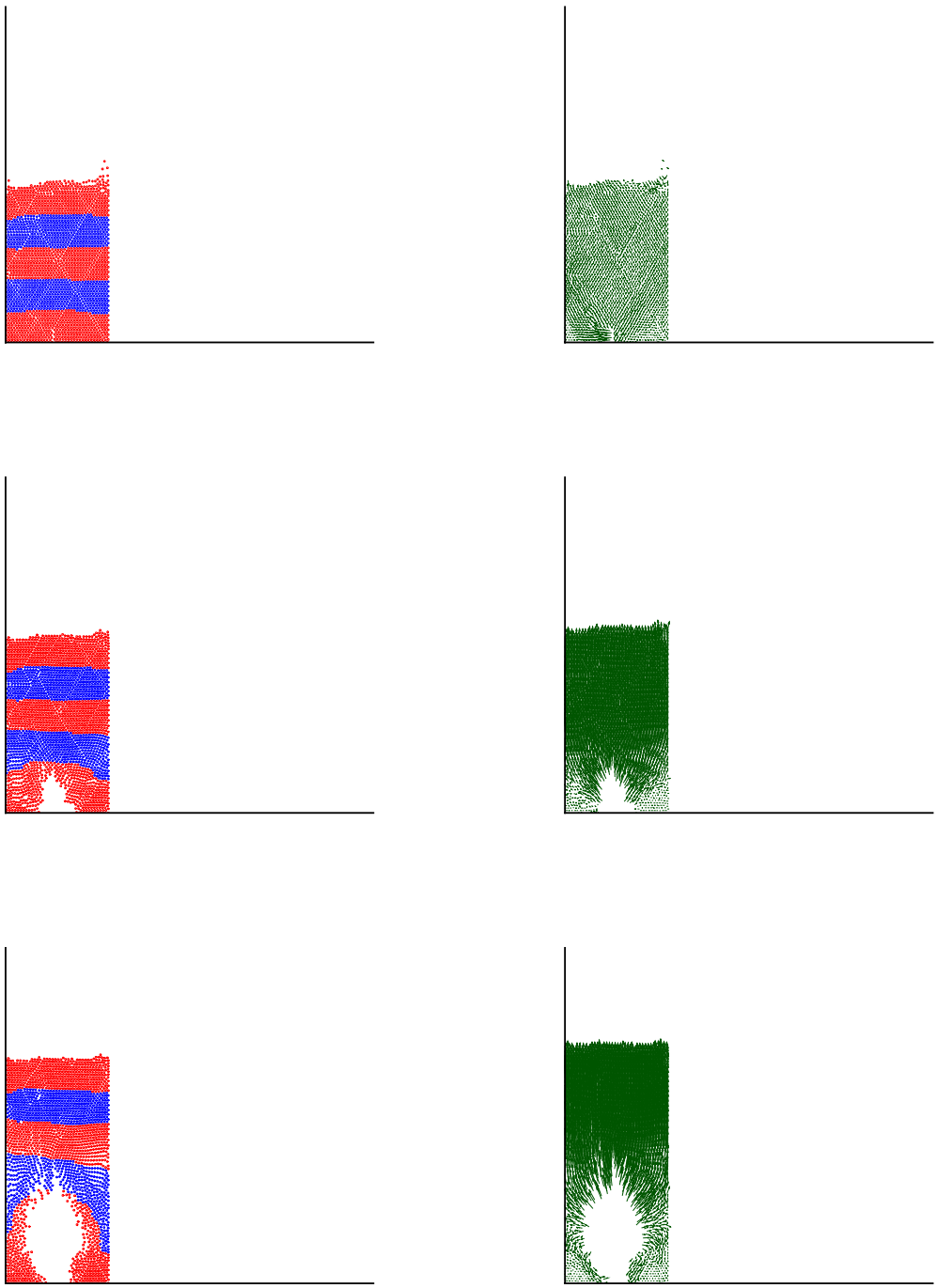

Figure 4.4. (a). Bubbling fluidized bed simulation results showing the particle position and the corresponding velocity vectors. (Continued in next page). The superficial gas velocity is 2.6 m/s.

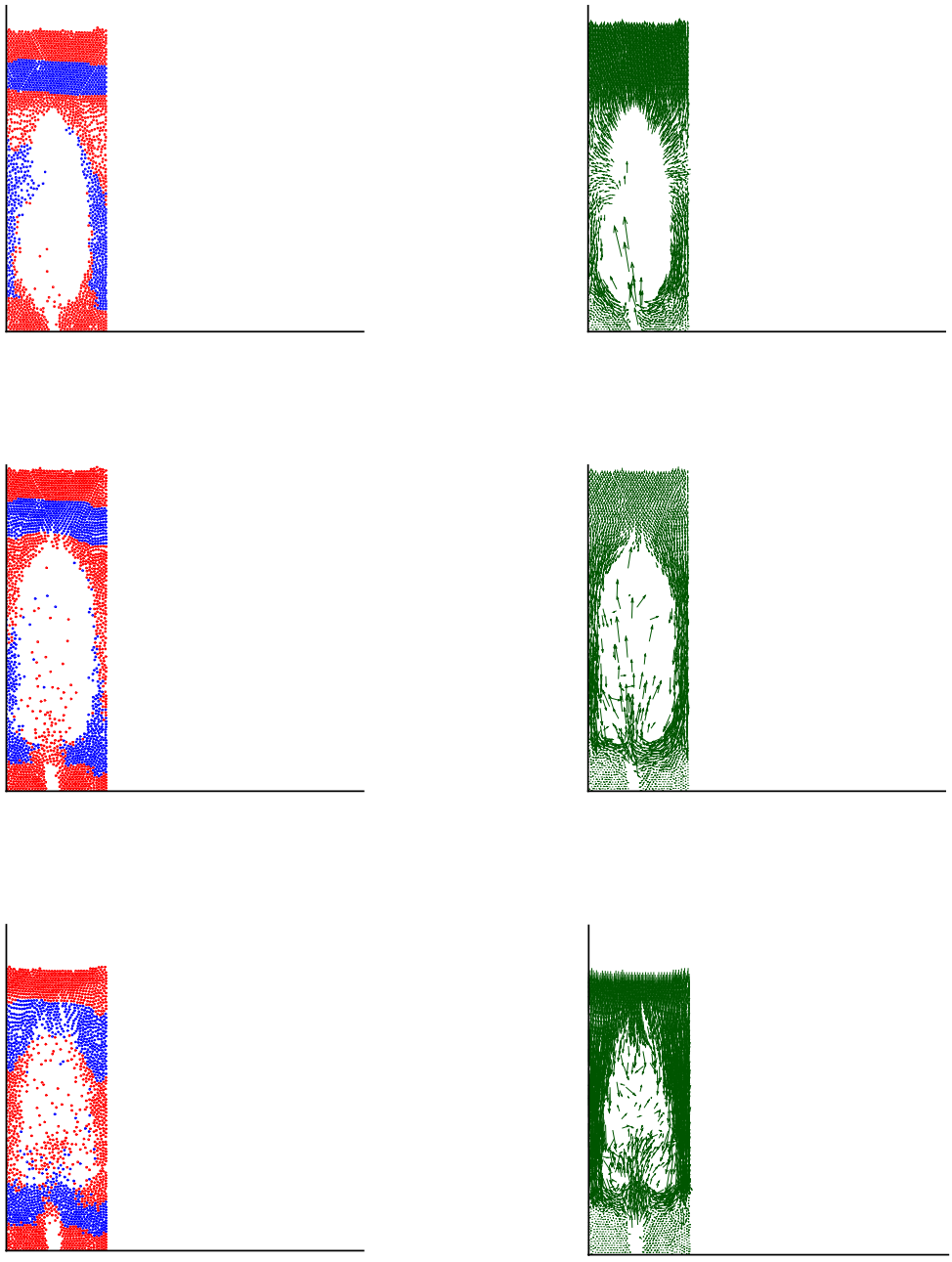

Figure 4.4. (b). Bubbling fluidized bed simulation results showing the particle position and the corresponding velocity vectors. (Continued in next page). The superficial gas velocity is 2.6 m/s.

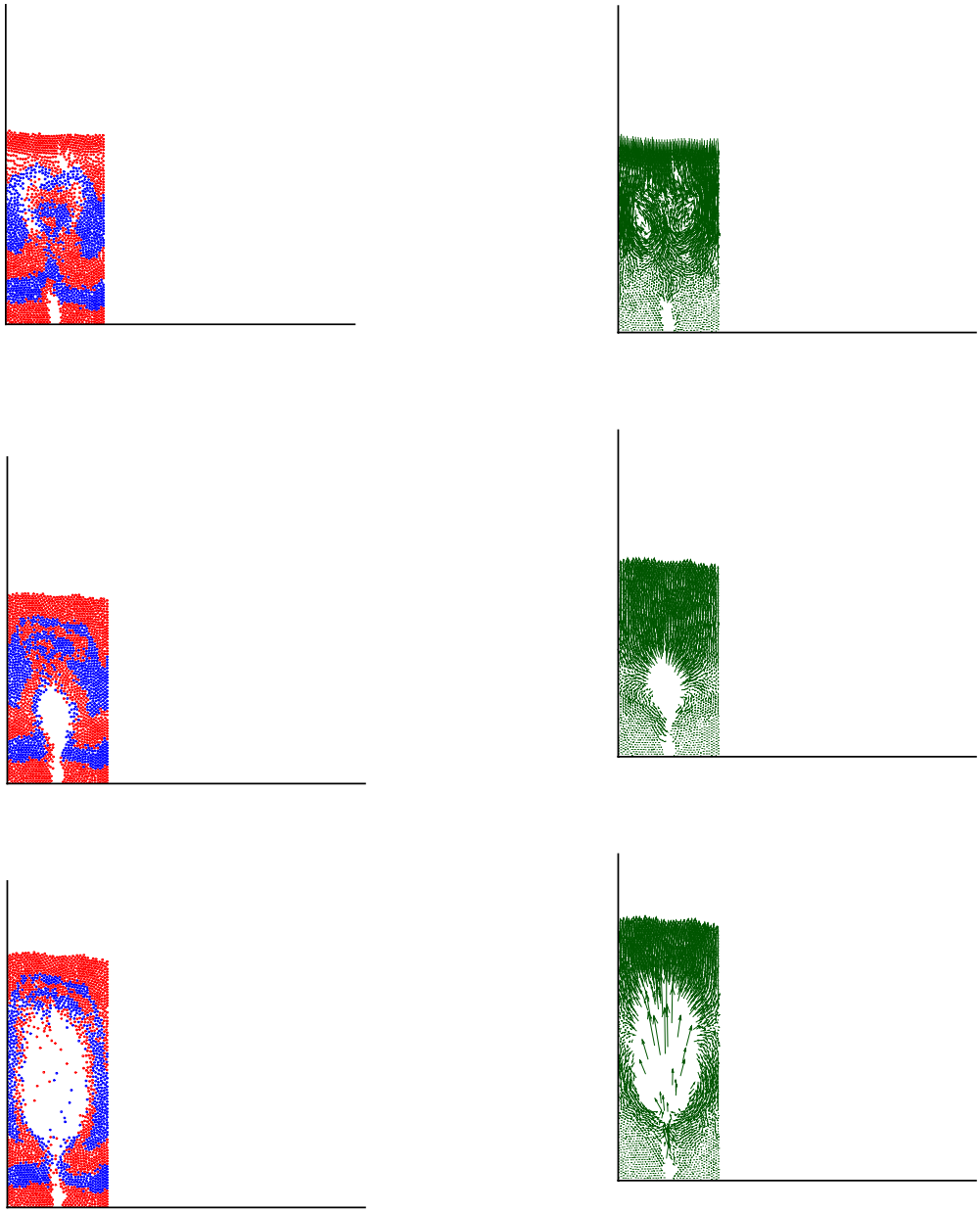

Figure 4.4. (c). Bubbling fluidized bed simulation results showing the particle position and the corresponding velocity vectors. (Continued in next page). The superficial gas velocity is 2.6 m/s.

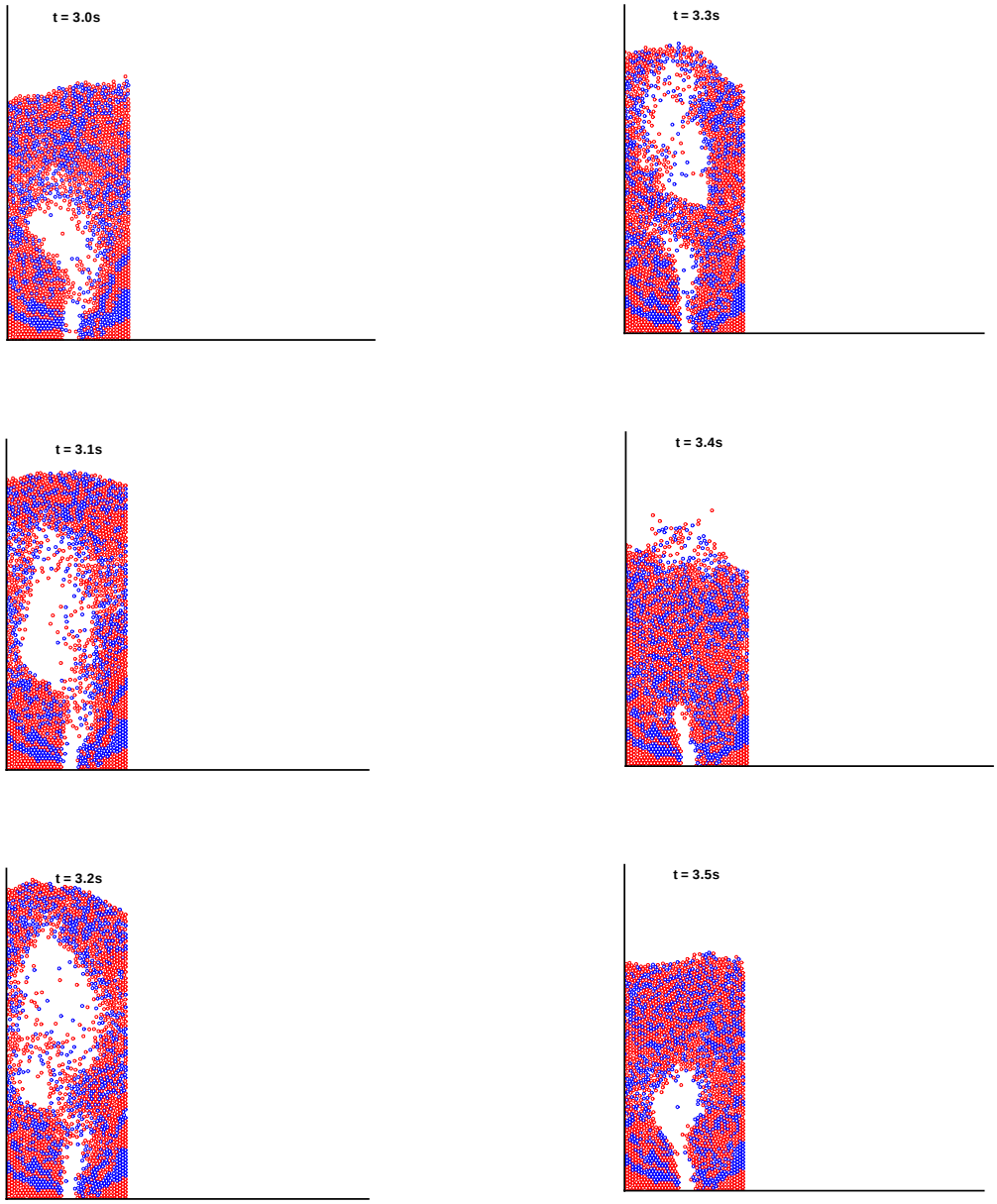

Figure 4.5. (a). Bubbling fluidized bed between 3 and 4 seconds of simulation. Two bubbles form and collapse. (Continued in next page). The superficial gas velocity is 2.6 m/s.

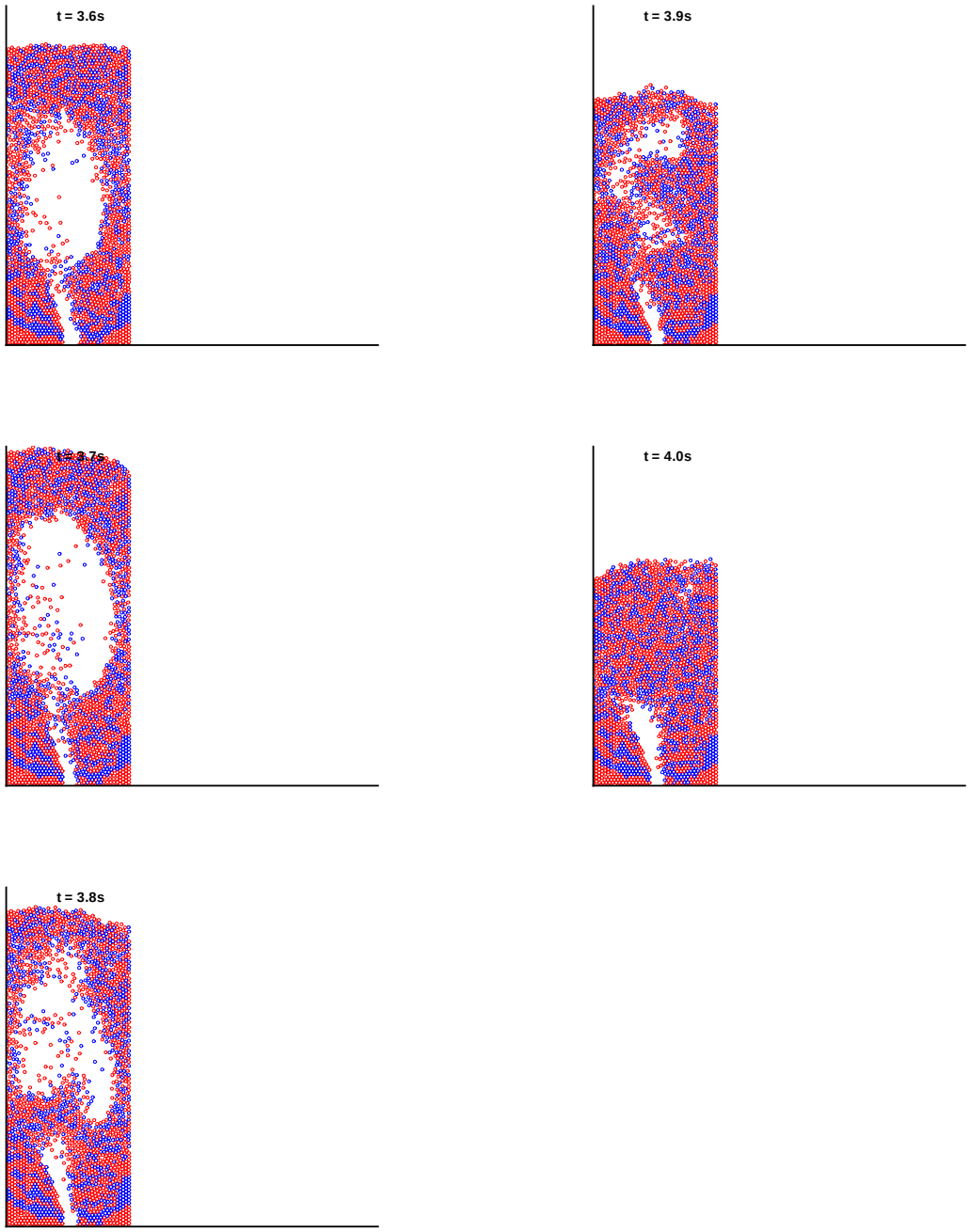

Figure 4.5. (b) Bubbling fluidized bed between 3 and 4 seconds of simulation. Two bubbles form and collapse in 1 second. Bubble swaying is also shown. The superficial gas velocity is 2.6 m/s.

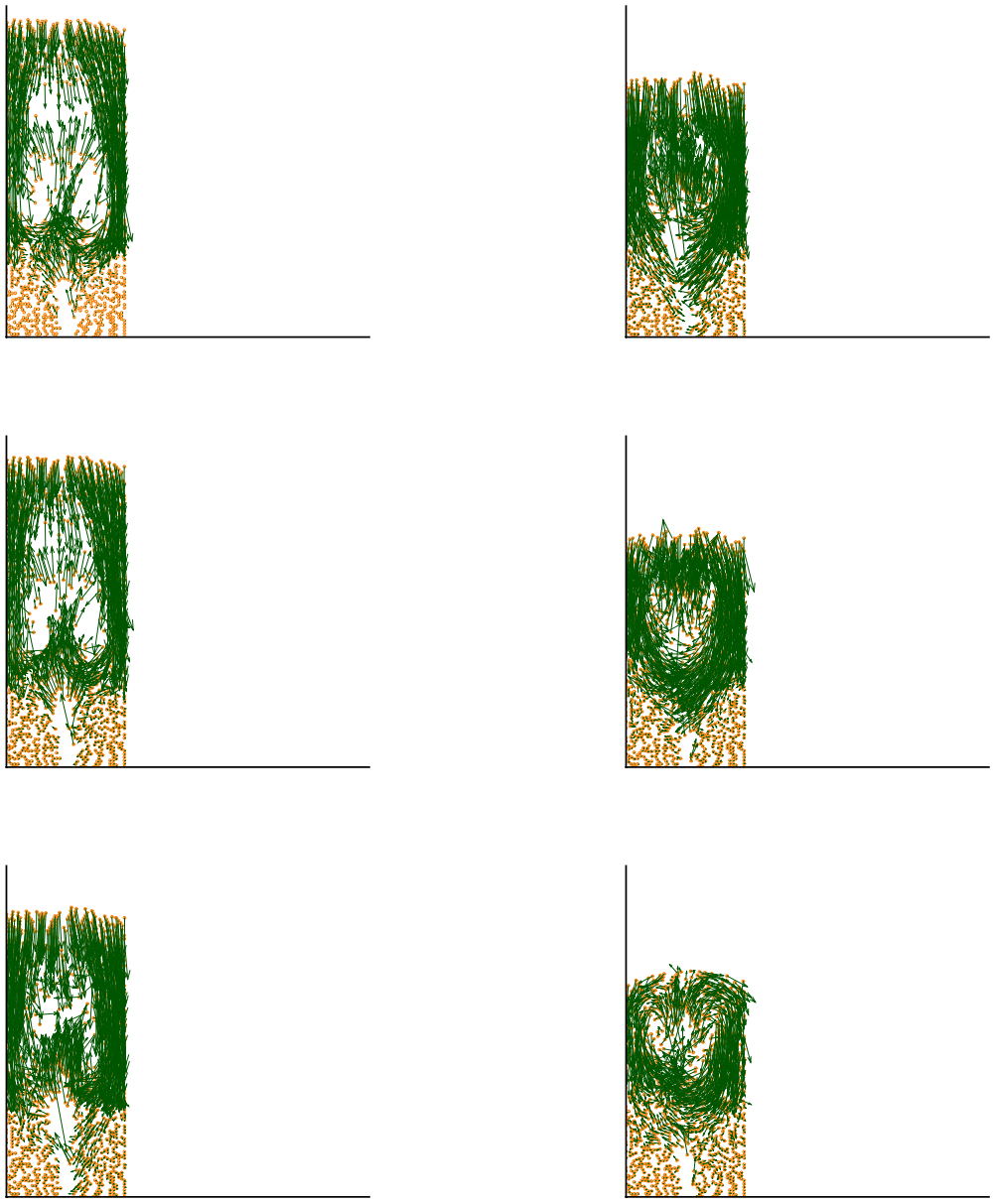

Figure 4.6. (a). Bubbling fluidized bed showing the local velocity vectors to explain the particle motion and velocity changes that occur when bubbles form and collapse. (Continued in next page). The superficial gas velocity is 2.6 m/s.

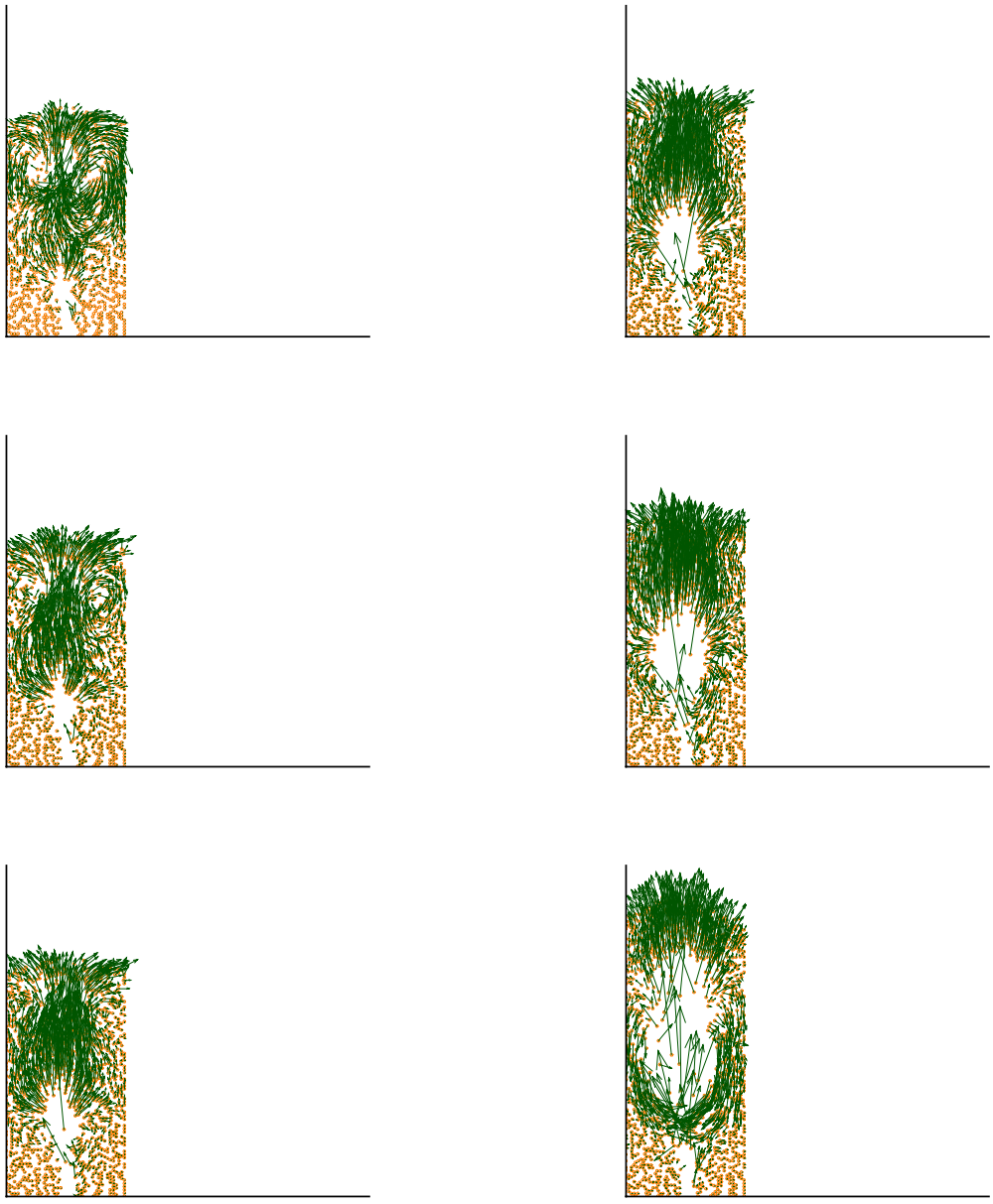

Figure 4.6. (b). Bubbling fluidized bed showing the local velocity vectors to explain the particle motion and velocity changes that occur when bubbles form and collapse. The superficial gas velocity is 2.6 m/s.

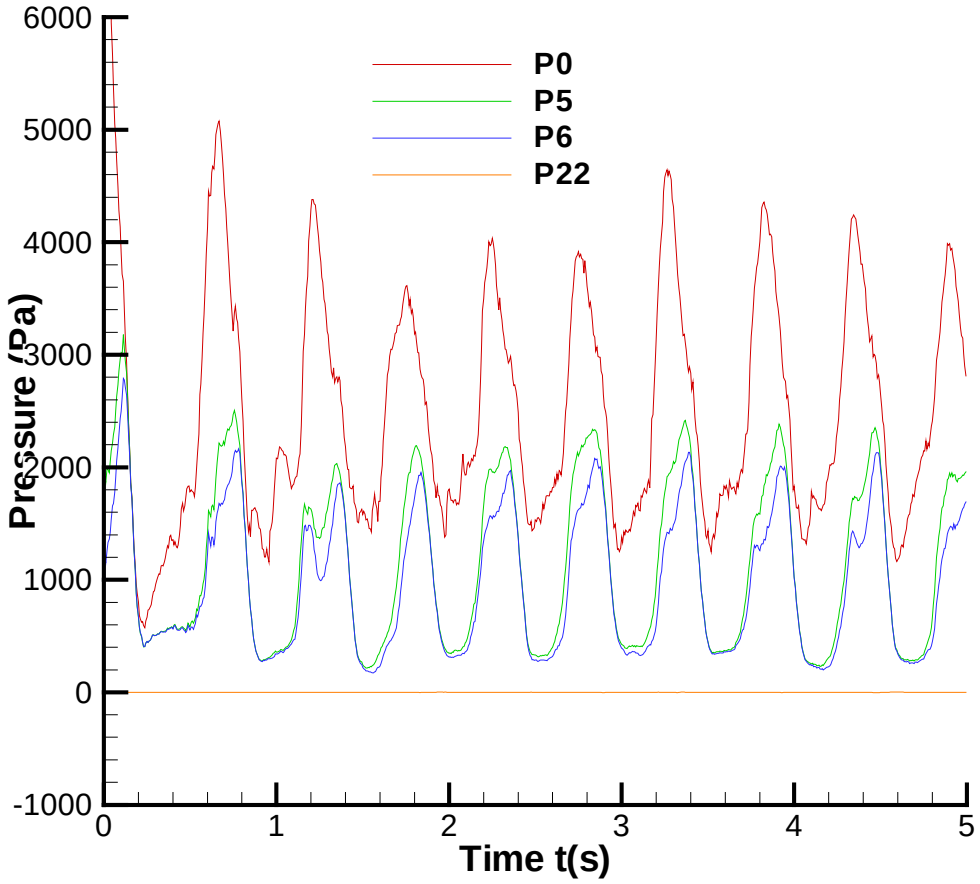

Figure 4.7. Pressure (Pa) vs Time (s) in a fluidized bed. Pressure at various heights from the bottom of the bed. The various plots shown are for pressure at a height (the height in cm from the bed floor is denoted by the number beside P in the legend) from the bed floor.

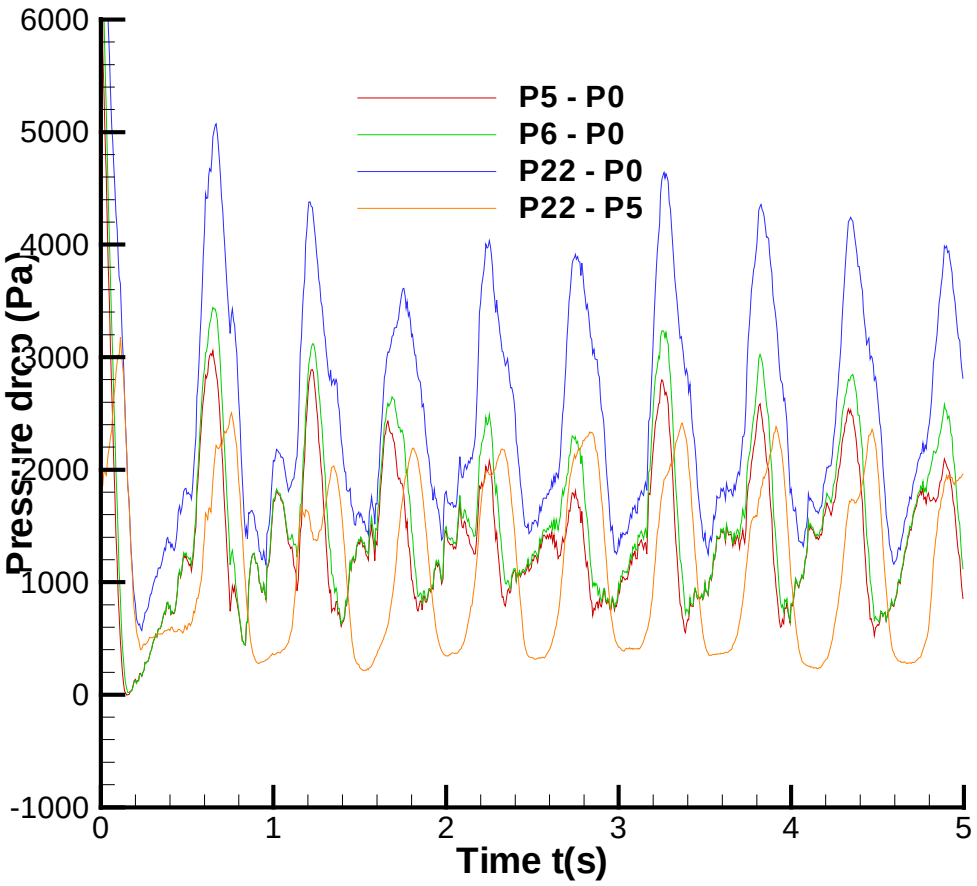

Figure 4.8. Pressure drop (Pa) vs Time (s) in a fluidized bed. Pressure at various heights from the bottom of the bed. The pressure drop range across the bed can be seen to be about 2000 Pa. The various plots shown are for pressure drops between two heights (the height in cm from the bed floor is denoted by the number beside P in the legend).

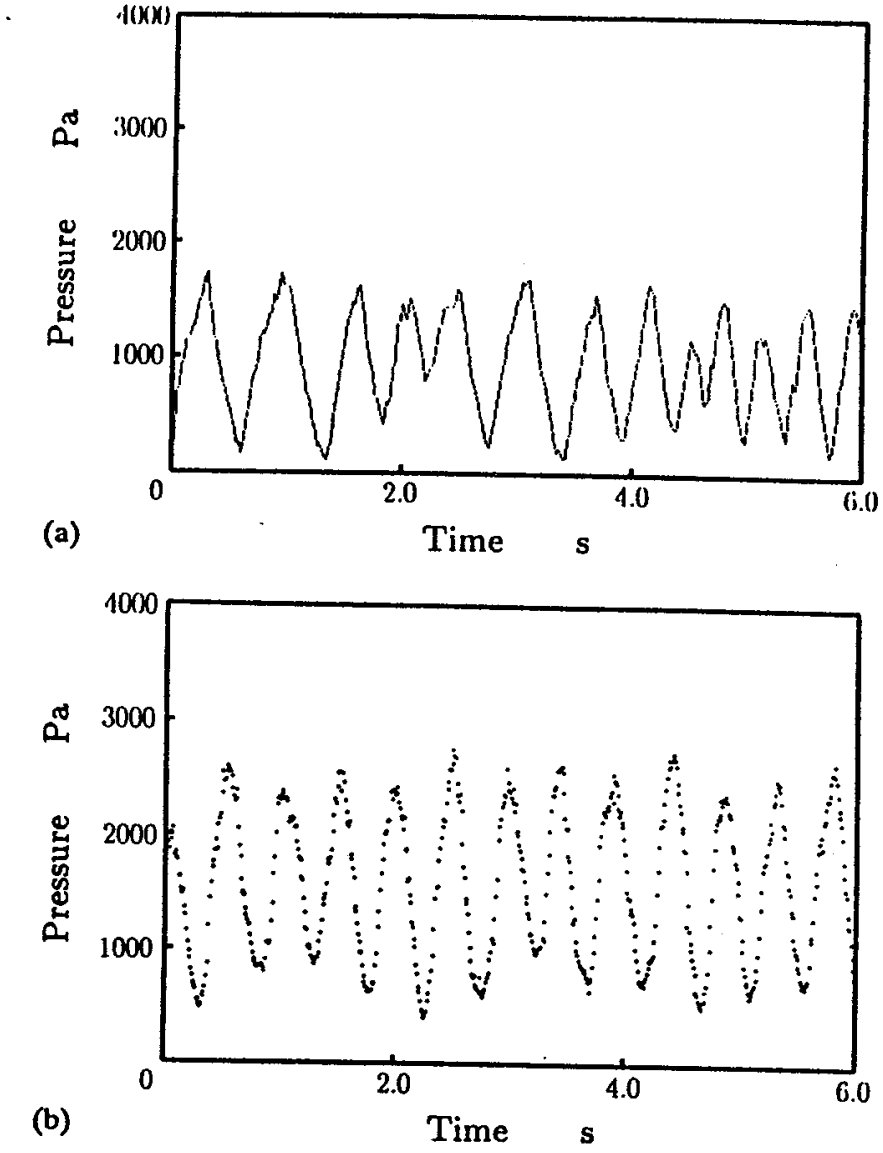

Figure 4.9. Pressure fluctuation from (a) experiment and (b) simulation reported by Tsuji (1993). The pressure drop across the bed, of about 2000 Pa can be seen.

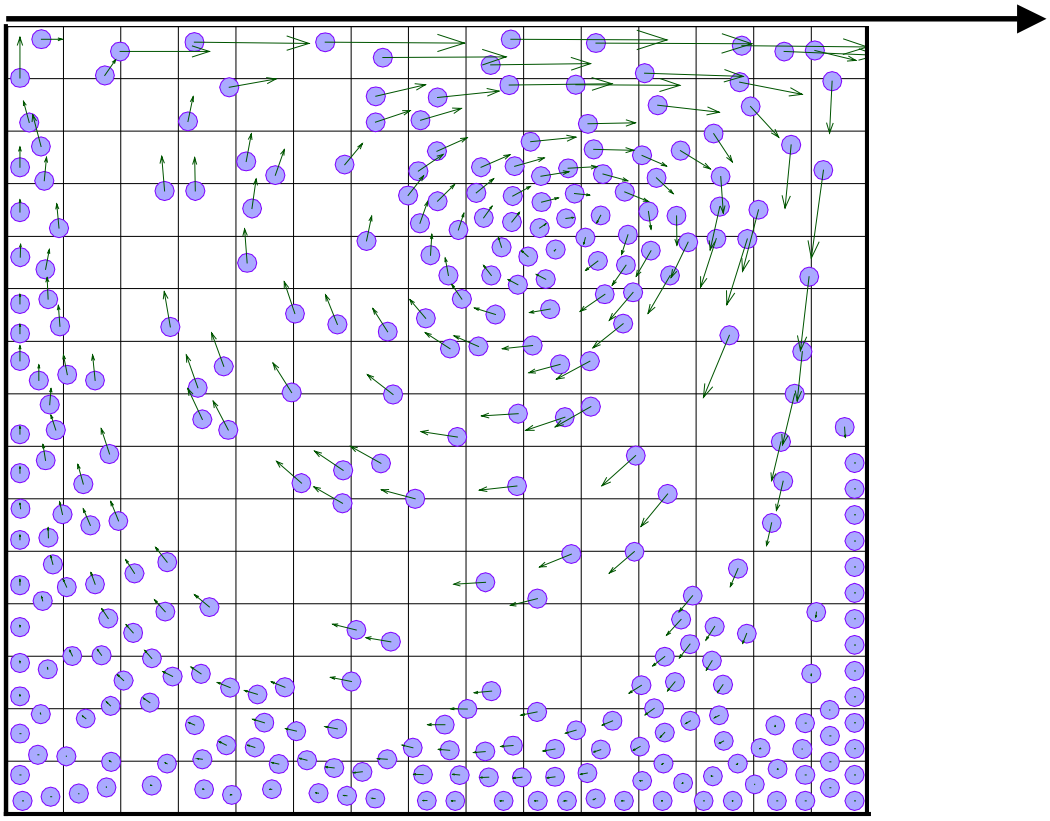

Figure 4.10. Instantaneous particle positions and velocity vectors in a wall-driven cavity. The simulation parameters are shown in Table 4.2.

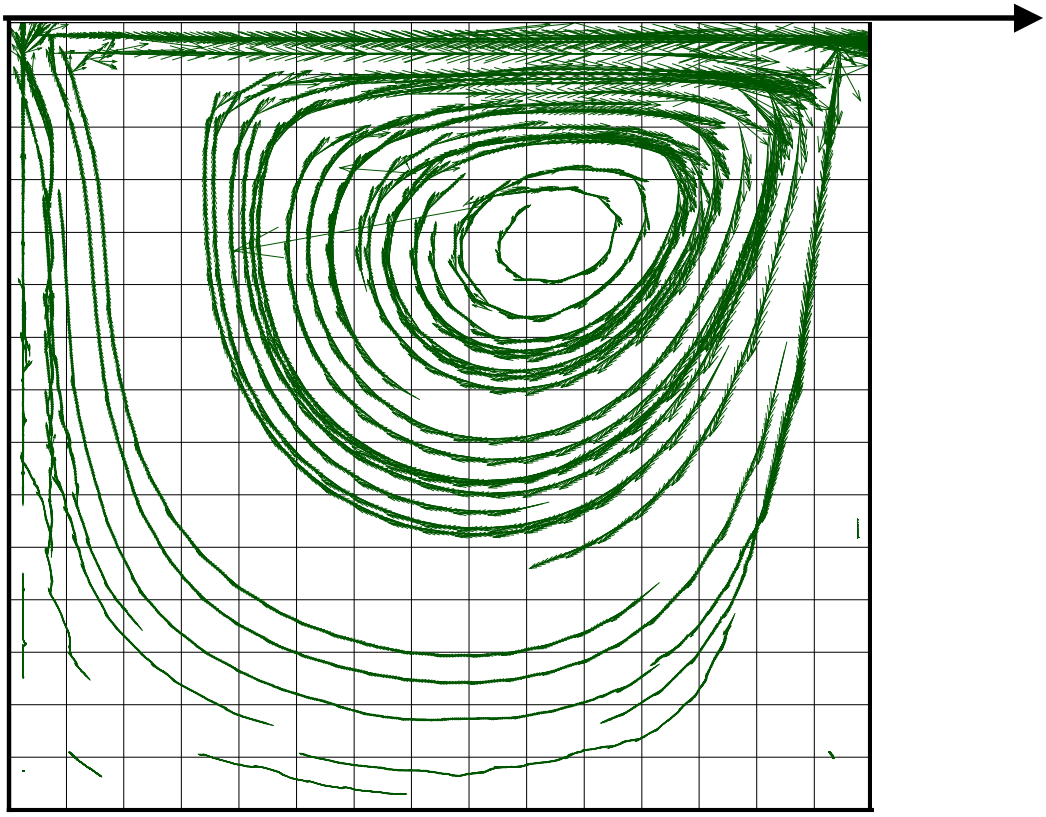

Figure 4.11 (a). Trajectories of 12 particles during the simulation time t= 0s to t=40s seconds for wall- driven cavity. The simulation parameters are shown in Table 4.2.

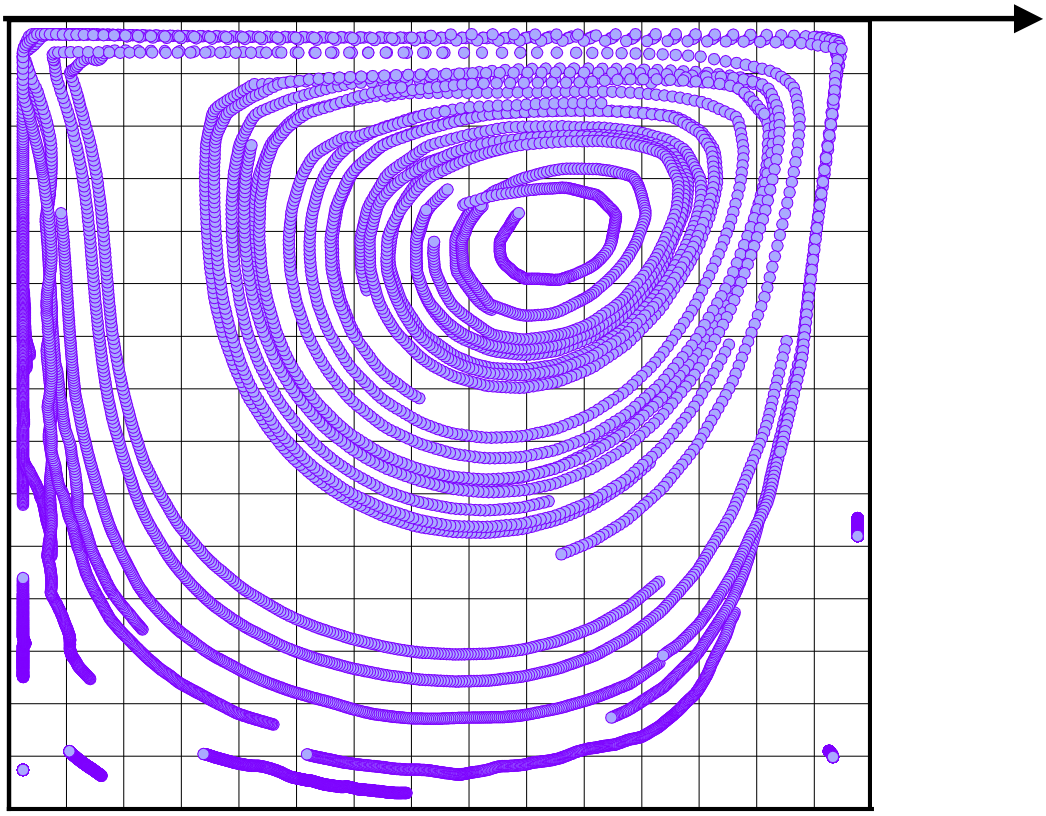

Figure 4.11 (b). Particle positions of 12 particles during simulations time t = 0s to t = 40s seconds for a top wall driven cavity. The simulation parameters are shown in Table 4.2.

Chapter 5

Fluidized Bed Simulations

A fluidized is a bed of fine particles through which a fluid is passed upward from the bottom of the bed, typically though a single inlet jet in the center. If the flow rate of the fluid is low, the particle bed acts as a porous medium and fluid merely percolates through the voids created by the stationary particles. As the fluid flow rate increases, the particles move apart and a few of them vibrate in restricted areas. This is known as an expanded bed. As the flow rate is further increased the particles get suspended in the upward moving fluid. This occurs because the drag exerted by the fluid on the particle counter balances the weight of the particle. This is known as a minimum fluidized bed and the velocity of the inlet jet is referred to as the minimum fluidization velocity. A further increase in the flow rate results in more agitated movement of the solids and formation of bubbles and channels occurs. Such a bed is called a bubbling fluidized bed. On further increasing the flow rate the particles get dispersed and the solids get carried out of the bed. This is referred to as a fluidized bed with pneumatic transport of solids.

Fluidized beds are very important in the chemical industry and are used for chemical conversions. A variety of applications exist namely, coal gasification, particle coating, transportation, mixing of fine powders, heat exchange, drying, particle growth and gas-solid reactions. Due to practical hurdles, fluidized beds used for these processes are difficult to study experimentally. For example, the coal gasification process is extremely difficult to see as the bed is soon coated with soot; as a result, particle motion and reaction dynamics cannot easily be studied. In such situations simulations of many of

these processes helps in better understanding the dynamics of a fluidized bed and also aids in better design and analysis.

The focus of this chapter is the influence of drag correlations on gas-solid flow predictions. As explained in Chapter 4, the choice of drag correlation is critical to determining the interphase drag force between the gas and solid. Some of the drag correlations published in the literature were listed in Chapter 4. In this chapter, gas-solid flows are computed using some of these published correlations and both local flow details and global quantities such as bed pressure drops are compared. In addition, one of the drag correlations is used to compute segregation in a fluidized bed containing a mixture of particles of two sizes. Comparisons of segregation for two different inlet jet velocities are made.

5.1 Comparison of drag correlations

A non-dimensional analysis is done to compare the drag correlations.

5.1.1. Non-dimensional analysis

A one-dimensional analysis is done in the y direction. Consider a particle falling in a stationary fluid in a tank of height L. The force balance equation for the particle is

$$\rho_s \frac{\partial v_s}{\partial t} = F_{gs}(v_g - v_s) + (\rho_g - \rho_s)g \tag{5.1}$$

where the left hand term is the force on the particle. The first term on the right hand side is the drag force on the particle and the second term in the right hand side accounts for buoyancy. Here, ρ_s is the solid particle density, ρ_g is the gas density, v_s is the solid,

particle velocity, v_g is the gas velocity, F_{gs} is the drag coefficient and g is the acceleration due to gravity.

Defining non-dimensional parameters as

$$v_s^* = \frac{v_s}{v_t}$$

$$v_g^* = \frac{v_g}{v_t}$$

$$t^* = t\frac{v_t}{L}$$

Here v_t is the inlet jet velocity. The non-dimensional form of Equation 5.1 would be

$$\frac{\partial v_s^*}{\partial t^*} = \left(\frac{LF_{gs}}{\rho_s v_t}\right)(v_g^* - v_s^*) + \left(\frac{\rho_g - \rho_s}{\rho_s}\right)\frac{gL}{v_t^2} \tag{5.2}$$

For the drag correlations implemented a comparison of the non-dimensional term $\left(\frac{LF_{gs}}{\rho_s v_t}\right)$ is first done to understand the differences in the basic drag correlations.

MFIX Drag Correlation

For the MFIX drag correlation (Syamlal et al, 1994)

$$F_{gs} = \frac{3}{4}\frac{\varepsilon_s \varepsilon_g \rho_g}{V_{rm}^2 d_{pm}} C_{DS}\left[\frac{\mathrm{Re}_m}{V_{rm}}\right]|V_{sm}|$$

The value of $\left(\frac{LF_{gs}}{\rho_s v_t}\right)$, denoted by D_m, is given by:

$$D_m = \frac{3}{4}\frac{\varepsilon_s \varepsilon_g \rho_g L}{V_{rm}^2 d_{pm} \rho_s v_t} C_{DS}\left[\frac{\mathrm{Re}_m}{V_{rm}}\right]|V_{sm}|$$

Tsuji Drag Correlation

For the Tsuji drag (Tsuji et al, 1993) correlation, we have the following value of dimensionless drag coefficient.

When $\varepsilon \le 0.8$, $F_{gs} = \dfrac{\mu(1-\varepsilon)}{d_p^2 \varepsilon}\left[150(1-\varepsilon)+1.75\,\mathrm{Re}\right]$.

The corresponding value of $\left(\dfrac{LF_{gs}}{\rho_s v_t}\right)$, denoted by D_t, is given by:

$$D_t = \frac{\mu(1-\varepsilon)L}{d_p^2 \varepsilon \rho_s v_t}\left[150(1-\varepsilon)+1.75\,\mathrm{Re}\right]$$

When $\varepsilon \rhd 0.8$, $F_{gs} = \dfrac{3}{4} C_D \dfrac{\mu(1-\varepsilon)}{d_p^2}\varepsilon^{-2.7}\,\mathrm{Re}$

The corresponding value of $\left(\dfrac{LF_{gs}}{\rho_s v_t}\right)$ is

$$D_t = \frac{3}{4} C_D \frac{\mu(1-\varepsilon)L}{d_p^2 \rho_s v_t}\varepsilon^{-2.7}\,\mathrm{Re}$$

Wen and Yu Correlation

For Wen and Yu's (1966) correlation

$$F_{gs} = C_d \frac{1}{8}\pi d_p^2 \rho_f \left|\vec{u}_s\right|(\vec{u}_s)\, f(\varepsilon).$$

The corresponding value of $\left(\dfrac{LF_{gs}}{\rho_s v_t}\right)$, denoted by D_k, is given by:

$$D_k = C_d \frac{L}{8\rho_s v_t}\pi d_p^2 \rho_f \left|\vec{u}_s\right|(\vec{u}_s)\, f(\varepsilon)$$

In the present comparison $f(\varepsilon) = \varepsilon^{-4.7}$ is shown.

Figure 5.1(a) shows the graphs for F_{gs} versus the void fraction for the MFIX drag correlation for various Reynolds numbers ranging from 30 to 2000. Figure 5.1(b) shows the graphs for the corresponding D_m versus the void fraction. Figure 5.2(a) shows the graphs for F_{gs} versus the void fraction for the Tsuji drag correlations for various Reynolds numbers ranging from 30 to 2000. Figure 5.2(b) shows the graphs for the corresponding D_t versus the void fraction. Figure 5.3(a) shows the graphs for F_{gs} versus the void fraction for the MFIX drag correlations for various Reynolds numbers ranging from 30 to 2000. Figure 5.3(b) shows the graphs for the corresponding D_k versus the void fraction. Clearly for all the correlations the graphs show unrealistic values for void fractions around zero. A void fraction of zero would mean a solid volume fraction of 1, which is higher than the closest packing solid fraction. For values typical of practical beds, void fractions in the range 0.42 - 0.9 are studied.

Figure 5.4 shows the comparison of the non-dimensional drag coefficient obtained from the MFIX correlation to the one obtained from the Tsuji correlation. D_m / D_t is plotted against the void fraction. The ratio is very close to one for the void fraction range of 0.42 to 0.9 and for all Reynolds numbers. This shows that the two correlations would predict similar bed behavior. Figure 5.5 shows the comparison of the non-dimensional drag coefficient obtained from MFIX correlation to the one obtained from the Wen and Yu correlation. D_m / D_k is plotted against the void fraction. The ratio for the void fraction range of 0.42 to 0.9 is quite different for different Reynolds numbers and is much greater than 1 (almost 10 in some cases). This shows that the two correlations would not predict similar bed behavior. A similar analysis can be done from

Figure 5.6. It shows the comparison of the non-dimensional drag coefficient obtained from the Wen and Yu correlation to the one obtained from the Tsuji correlation. D_k / D_t is plotted against the void fraction. The ratio for the void fraction range of 0.42 to 0.9 is quite different for different Reynolds numbers and is much lesser than 1. This shows that the two correlations would not predict similar bed behavior.

5.1.2. Fluidized Bed Results

Fluidized bed simulations have been performed for the simulation parameters as listed in table 4.1. The MFIX drag correlation, Tsuji's drag correlation, and Wen and Yu's drag correlation (with α values of 4.7 and 8) have been implemented. Simulations were done for the first 10 seconds of bed operation. Ten snap shots of the bed are shown for the different drag correlations in Figures 5.7, 5.8, 5.9 and 5.10. In Figure 5.7 the bed simulated by using the MFIX drag correlation is shown. In Figure 5.8 the bed simulated by using the Tsuji drag correlation is shown. Figures 5.9 and 5.10 are snap shots of the bed simulated by using Wen and Yu's correlation for α values of 4.7 and 8 respectively. It can be seen that the details of the bed behavior are quite different for the four cases, with the bed being most violent in the case of α value of 8. The initial bed height in all cases is 22 cm. The maximum bed height in case of MFIX drag correlation is about 32 cm; in the case of the Tsuji drag correlation, it is 35 cm; in the case of the Wen and Yu correlation with $\alpha = 4.7$, the value is 38 cm; and for the Wen and Yu correlation with $\alpha = 8$, the maximum bed height is 50 cm. For the same initial conditions and the same inlet jet velocity, the bed height varies for the difference cases because of the drag exerted on the particles changes and hence the movement of the particles is predicted

differently. Though the MFIX, Tsuji and Wen and Yu correlation with $\alpha = 4.7$ predict maximum bed heights with 20% of each other, the strong non-linear dependence on void fraction for $\alpha = 8.0$ makes for large differences in both bed height and flow patterns. Thus, the MFIX drag correlation, the Tsuji drag correlation and the $\alpha = 4.7$ case exhibit a single bubble forming periodically. For the case of $\alpha = 8$, bubble formation is not as periodic as in the other cases and the bubble splits into smaller bubbles before collapsing.

Some of the parameters considered in the design of a fluidized bed are the pressure drop across the bed and at various heights in the bed, as well as the bubble size, bubble velocity and bubble frequency. The pressure drop across the bed is plotted against time for the fours cases being studied and are shown in Figures 5.11, 5.12, 5.13 and 5.14. Though the maximum and minimum values are different, the RMS values of the pressure drops are not. The RMS pressure drop value for MFIX drag correlation is 1022 Pa. For Tsuji correlation case it is 1019 Pa, 0.27 percent different from the MFIX value. For $\alpha = 4.7$, the RMS pressure drop value is 942 Pa, which is 7.8 percent different from MFIX value. Even the $\alpha = 8$ case, which appears most violent in behavior, has a RMS pressure drop value of 1043 Pa, which is about 2.11 percent different from MFIX drag correlation. This shows that though the apparent local behavior of the fluidized beds simulated using the various drag correlations is different, the pressure drop is predicted almost similarly by all the correlations. Also shown in the figures are the power spectrum of the pressure drop curves. In all the four cases the dominant frequency is found to be 2 per second. This indicates that the bubbling frequency is 2 per second because it is the formation and collapsing of the bubbles that is a major contributor to the pressure fluctuations across the bed. This shows that the drag correlations in general do a similar

job in predicting the global quantities for a fluidized bed, which are used in design. But this is to be expected as the correlations are generally developed over time averaged quantities and not spatially and temporally local quantities. But local behavior in the fluidized bed is important because this affects the overall heat and mass transfer and hence the chemical conversion. From Figures 5.7 to 5.10, it can be seen that the drag correlations predict similar global quantities like pressure drop, bubble frequency as explained earlier but can differ substantially in the local behavior.

5.1.3. Granular Temperature

In this section, we present plots of the granular temperature in the bed. Granular temperature is a measure of the particle velocity fluctuation in the bed. It is defined as the specific kinetic energy of the random fluctuating component v_{fl} of the particle velocity.

$$\frac{3}{2}\theta = \frac{1}{2}\left\langle v_{fl}{}^{2} \right\rangle$$

Where θ is the granular temperature of a particle and v_{fl} is the fluctuating component of the instantaneous velocity v_1 of the particle, such that

$$v_1 = v_{ave} + v_{fl}$$

where v_{ave} is the average velocity of the particle over a time interval that is sufficiently long time compared to the time scale of the fluctuating velocity, but short compared to the larger times scales in the problem, such as the bubble formation frequency.

The granular temperature of the solid in each computational cell has been computed. The average velocity of the particle is computed from the particle velocity values of previous 100 time steps. Figure 5.15 shows the granular temperature plots at the

8^{th} second in the simulation, for all the four drag correlations studied. The difference in the local behavior can be clearly seen. The peaks represent higher granular temperature; in other words higher particle fluctuation. Comparing the case of $\alpha = 8$ with the others we can see that the fluctuation is more distributed in this case, meaning that the bed is more mixed and hence would predict higher contact times and better chemical conversion. In the other cases the maximum granular energy is near the inlet jet as can be expected as that particles near the jet inlet would experience most drag. The rest of the bed is comparatively quiescent except for localized regions of particle fluctuation.

5.2. Simulation of Binary Mixture Fluidized Beds

Most published research on the simulation of fluidized beds has focused on single-sized particle suspensions using both kinetic theory and, to some extent, discrete element models. In reality, though, there exists a distribution of particle sizes, and segregation patterns are determined by the gas flow. The segregation patterns determine the contact time between the gas and particles of different sizes. This contact time is critical in determining the rates of chemical reactions. A few studies have begun to appear in the literature which study fluidized beds with binary particle distribution. Both kinetic theory (Huilin et al 2003) and discrete element simulation (Tsuji et al, 2003) have been employed for the study of binary mixture fluidized beds. Huilin et al (2003) have implemented the kinetic theory for granular material to study a distributed jet bubbling fluidized bed with binary mixtures. They have reported that segregation occurs in a binary fluidized bed such that the bigger particles sediment to the bottom and the smaller particles remain in the upper regions. For higher superficial velocities more mixing

occurs. Tsuji et al (2003) used DES to study a single central jet binary mixture fluidized bed. They studied the particle size effect and the fluidized bed cylinder size effect on mixing and have reported that better mixing occurs for smaller particles in larger cylinders and at high superficial velocities. They have further studied the effect of particle size ratios and density ratios on the behavior of binary mixture fluidized beds. They reported that depending on the particle size ratio and density ratio, binary mixtures in a fluidized bed can be made mixable or non-mixable. They reported better mixing of particles with lesser difference in size as well as density. Nevertheless, much remains to be understood about the dynamic behavior of binary fluidized beds.

The present work is a further contribution to the growing interest in binary mixture fluidized bed behavior studies. Fluidized beds with binary mixtures have been simulated for the simulation parameters shown in Table 5.1. A particle size ratio of 1 to 2 has been simulated for a single central inlet jet fluidized bed. The minimum fluidization velocity for the bed is 3.8 m/s. Two of the simulated cases are presented here: one for a superficial velocity of 4.5 m/s and the other with the superficial velocity of 6 m/s, much higher than the minimum fluidization velocity. Initially the bigger particle layer is sandwiched between two layers of the smaller particles. The initial bed height is 26 cm. For the purpose of drag correlation implementation, in the present simulations the bed depth has been taken to be the maximum of the two particles diameters. Another option would be to take a mean diameter and use it as the bed depth. The MFIX drag correlation has been used in this simulation.

For the case with superficial gas velocity of 4.5 m/s, the bed rises through bubble formation to 75 cms in the initial transient stage. 5 snapshots of the particle positions in

the first second have been shown in Figure 5.16. The corresponding velocity vectors are shown in Figure 5.17. In Figure 5.18, a snapshot of the bed is shown with both the particle positions and velocity vectors. The bed settles to a maximum height of about 50 cm. The pressure drop across the bed is shown in Figure 5.19.

For the case with superficial gas velocity of 6 m/s, the bed rises to a height of 135 cm through a spouting kind of behavior in the initial transient stage. 5 snapshots of the particle positions in the first second have been shown in Figure 5.20. The corresponding velocity vectors are shown in Figure 5.21. In Figure 5.22, a snapshot of the bed is shown with both the particle positions and velocity vectors. The bed settles to a maximum height of about 60 cm. The pressure drop across the bed is shown in Figure 5.23.

Comparing the two cases clearly demonstrates that for the same bed conditions for low superficial gas velocity, there is substantial segregation at the bed base when binary mixtures are present. The bigger particles tend to settles at the base while the smaller particles occupy the upper regions of the bed. For higher superficial velocities mixing dominates and the segregation at the bed base is not dominant. Also it is interesting to note from the simulations that bigger particles tend to keep away from the side-walls. They typically are in the inlet jet core or around the bubble or segregated on the bed base while smaller particles move closer to the walls. In both the cases slugs are formed on the top of the bed. The bubble forms below the slug and the gas seeps out of the slug as in a porous medium. The pressure drop across the bed in both the cases is around 300 Pa.

5.3. Closure

The effect of drag correlations used to calculate the interphase drag force has been studied and presented in this chapter. This is very important because accurate drag force calculation is needed for predicting both the local and global bed behavior correctly. The drag correlations used here have been developed by using time-averaged data. Therefore they predict similar values of global quantities such as the bed pressure and bubble frequency. But local predictions of void fractions and granular temperatures are substantially different, and may indicate that quantities depending on the local variations, such as chemical reaction rates, may depend strongly on what correlations are used. Better drag correlations fluidized and bubbling beds are necessary, as well as more local experimental data for validating simulation results.

A fluidized bed with two particle sizes has been simulated. The bed behavior for two superficial gas velocities is compared. For superficial velocities closer to the minimum fluidization velocity, segregation takes place with the bigger particles settling at the bed base. For higher superficial velocities, mixing dominates segregation. Slugs are formed in the cases simulated.

Table 5.1. Binary mixture fluidized bed simulation parameters

Bed Dimensions (W X H)	150 mm X 900 mm
Fluid mesh size	15 X 50
Cell dimensions	10 mm X 20 mm
Particle bed height at rest	260 mm
Minumum fluidization velocity	3.8 m/s
Superficial gas velocity	4.5 m/s and 6 m/s
Number of Particle: N	1850
Particle number ratio: N_1/N_2	1650/200
Particle diameter ratio: d_1/d_2	4mm/8.1mm (1:2.1)
Particle density: ρ_s	2700 kg/m^3
Gas density: ρ_g	1.205*10^{-3} kg/m^3
Gas viscosity: μ_g	1.80*10^{-5} N/m^2
Particle coeff. of restitution: ε	0.9
Particle stiffness coeff: k	800 N/m
Particle damping coeff: v	0.18 (N.s)/m
Particle friction coeff: μ_f	0.3
Ratio of fluid time step to particle time step: $\frac{\Delta t_f}{\Delta t_s}$	$\frac{5*10^{-3}}{2*10^{-4}} = 25$

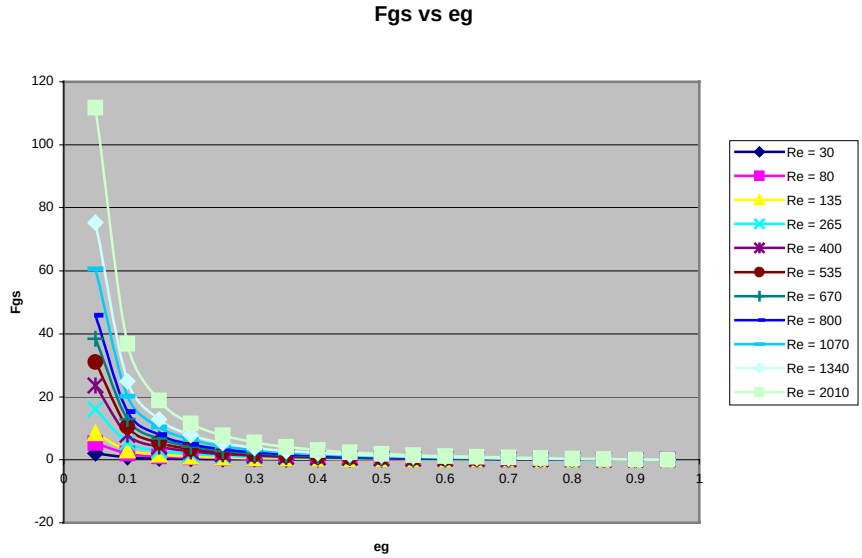

(a)

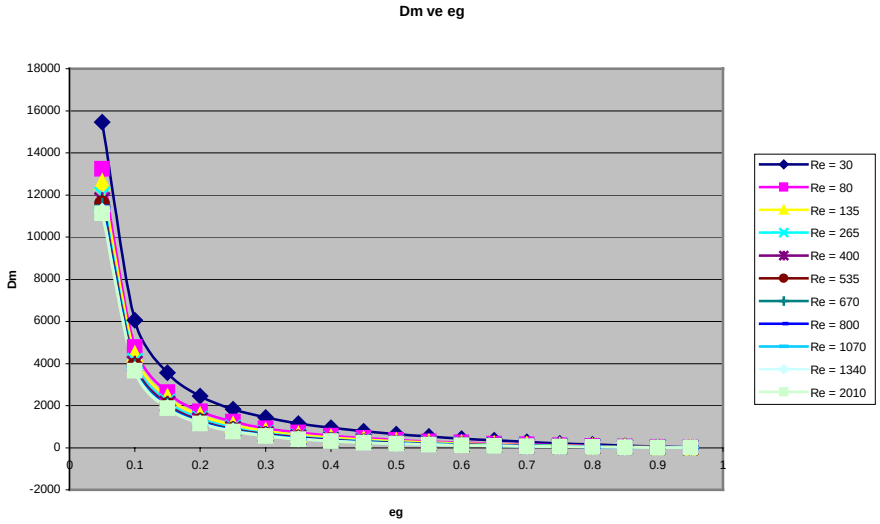

(b)

Figure 5.1. (a) F_{gs} versus the void fraction for the MFIX drag correlation for various Reynolds numbers ranging from 30 to 2000 (b) the corresponding D_m versus the void fraction

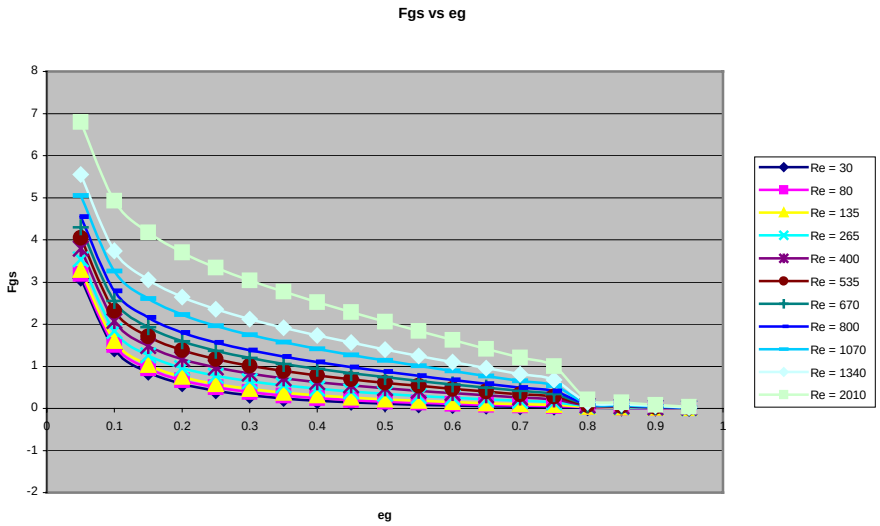

(a)

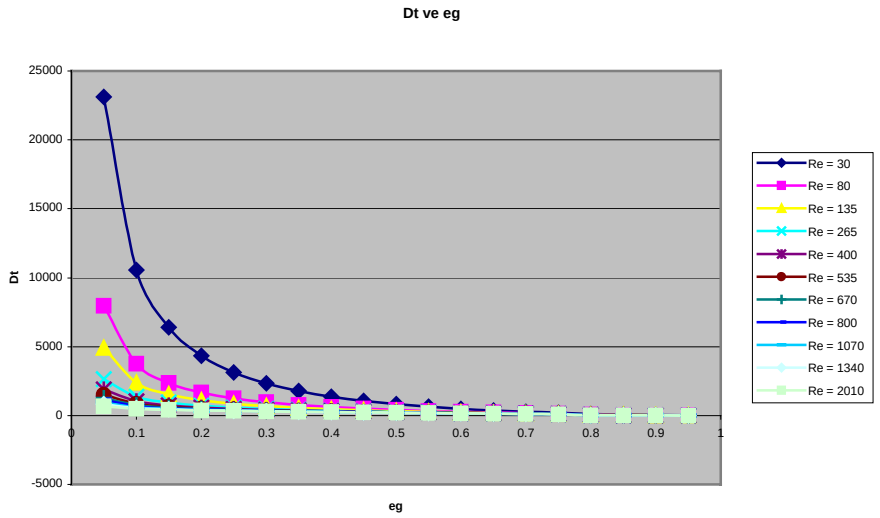

(b)

Figure 5.2. (a) F_{gs} versus the void fraction for the Tsuji drag correlation for various Reynolds numbers ranging from 30 to 2000 (b) the corresponding D_t versus the void fraction

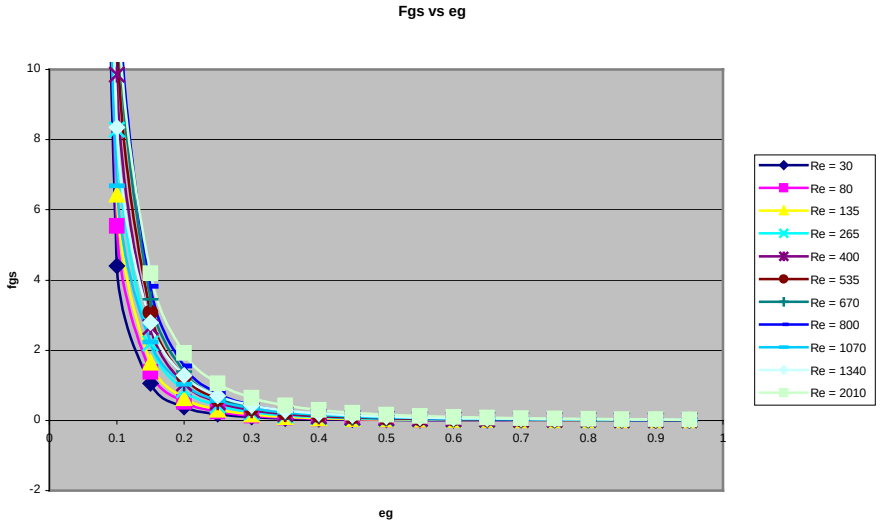

(a)

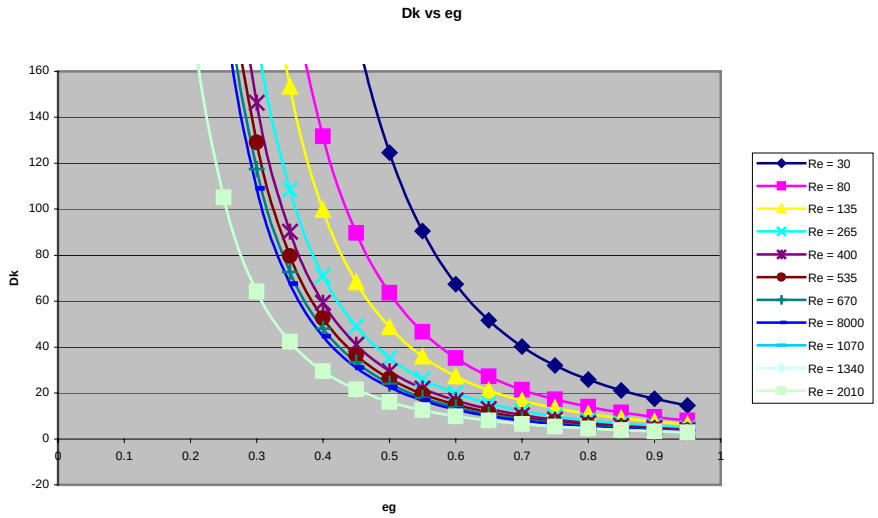

(b)

Figure 5.3. (a) F_{gs} versus the void fraction for the Wen and Yu ($\alpha = 4.7$) drag correlation for various Reynolds numbers ranging from 30 to 2000 (b) the corresponding D_k versus the void fraction.

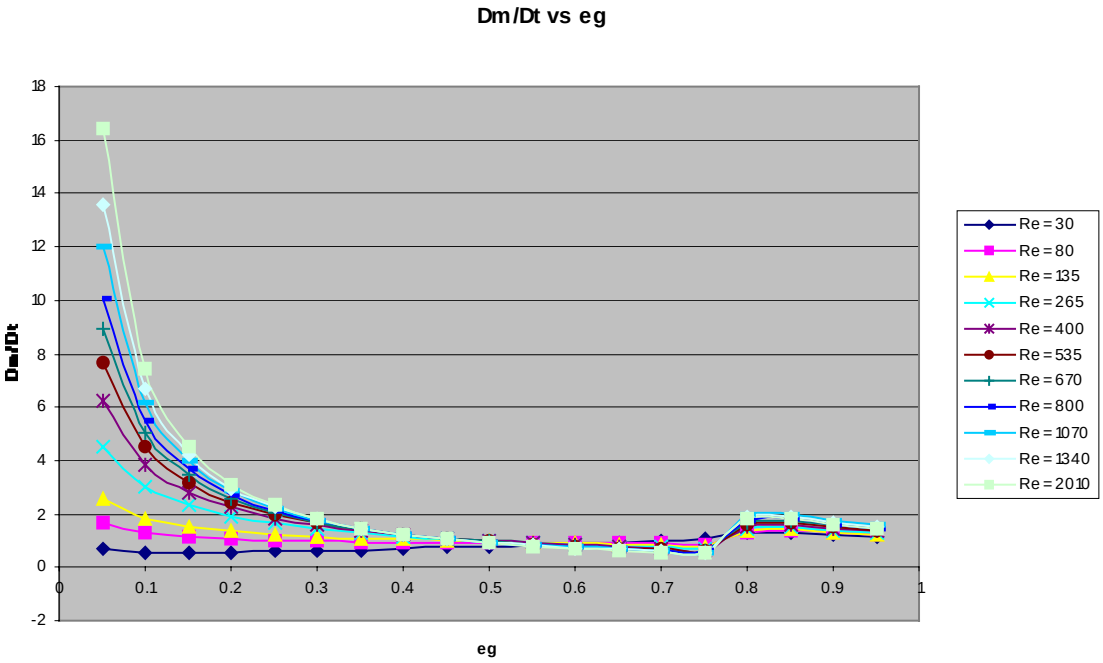

Figure 5.4. D_m/D_t versus void fraction for Reynolds numbers range of 30 to 2000

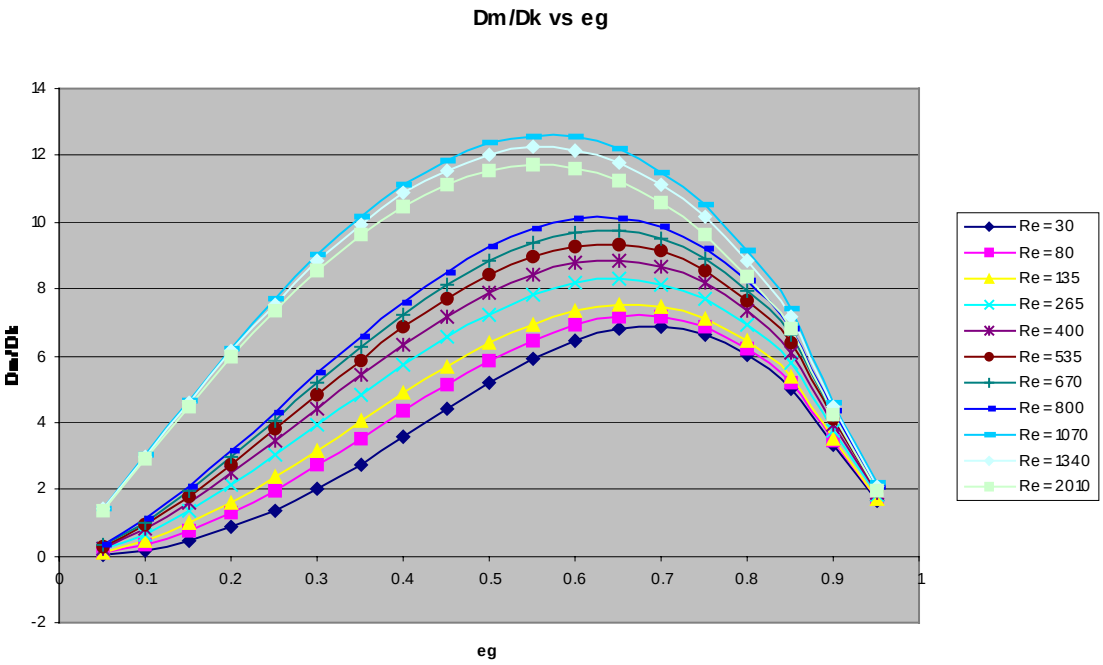

Figure 5.5. D_m / D_k versus void fraction for Reynolds numbers range of 30 to 2000

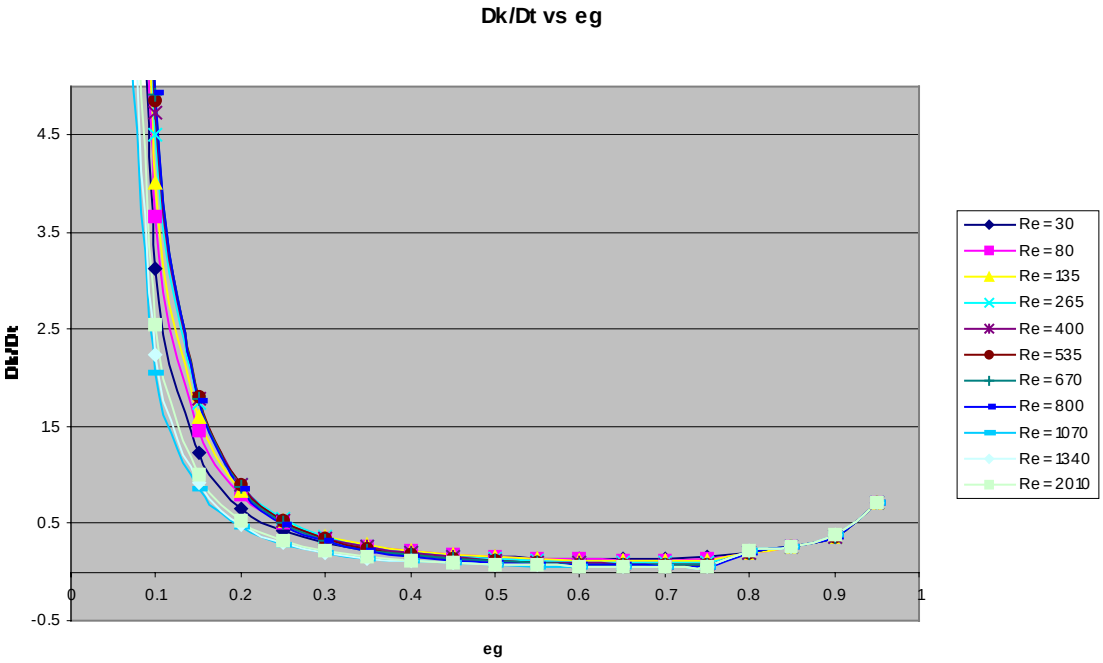

Figure 5.6. D_k / D_t versus void fraction for Reynolds numbers range of 30 to 2000

(1)

(2)

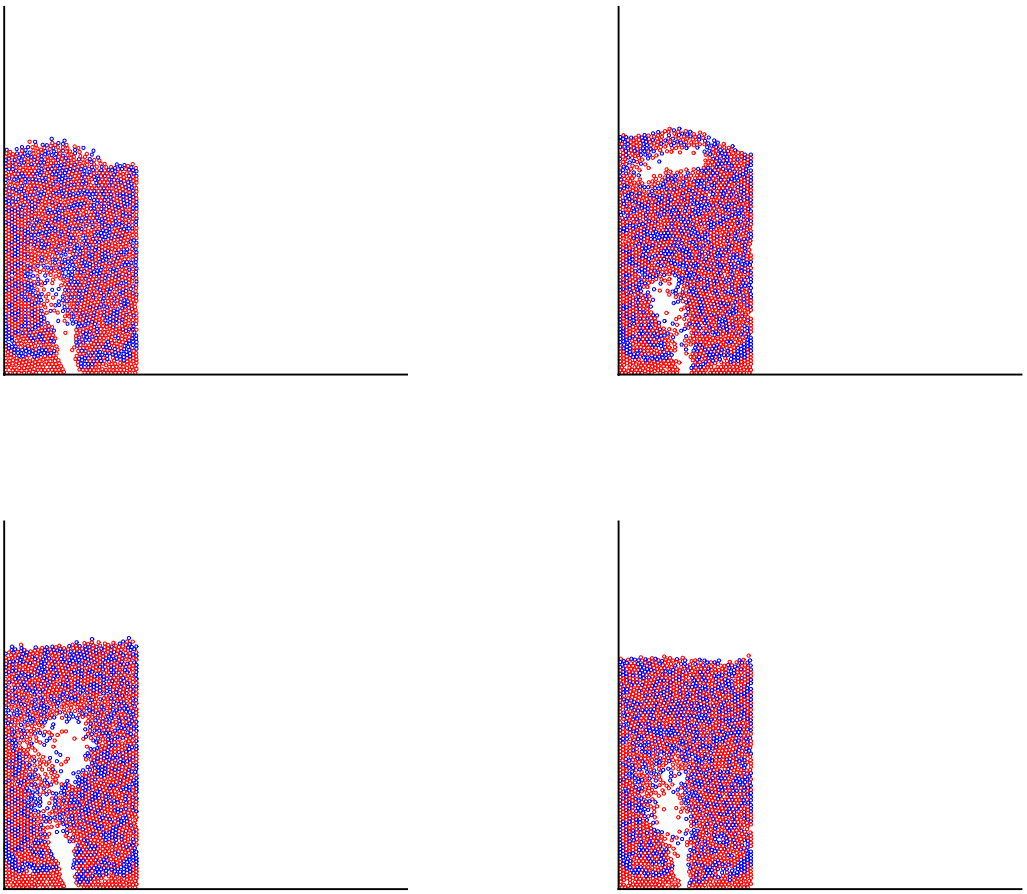

Figure 5.7. Fluidized bed simulated using MFIX drag correlation. 10 snapshots are shown between the 6th and 8th simulation seconds. Superficial gas velocity s 2.8m/s.

(Continued in next page)

(3)

(4)

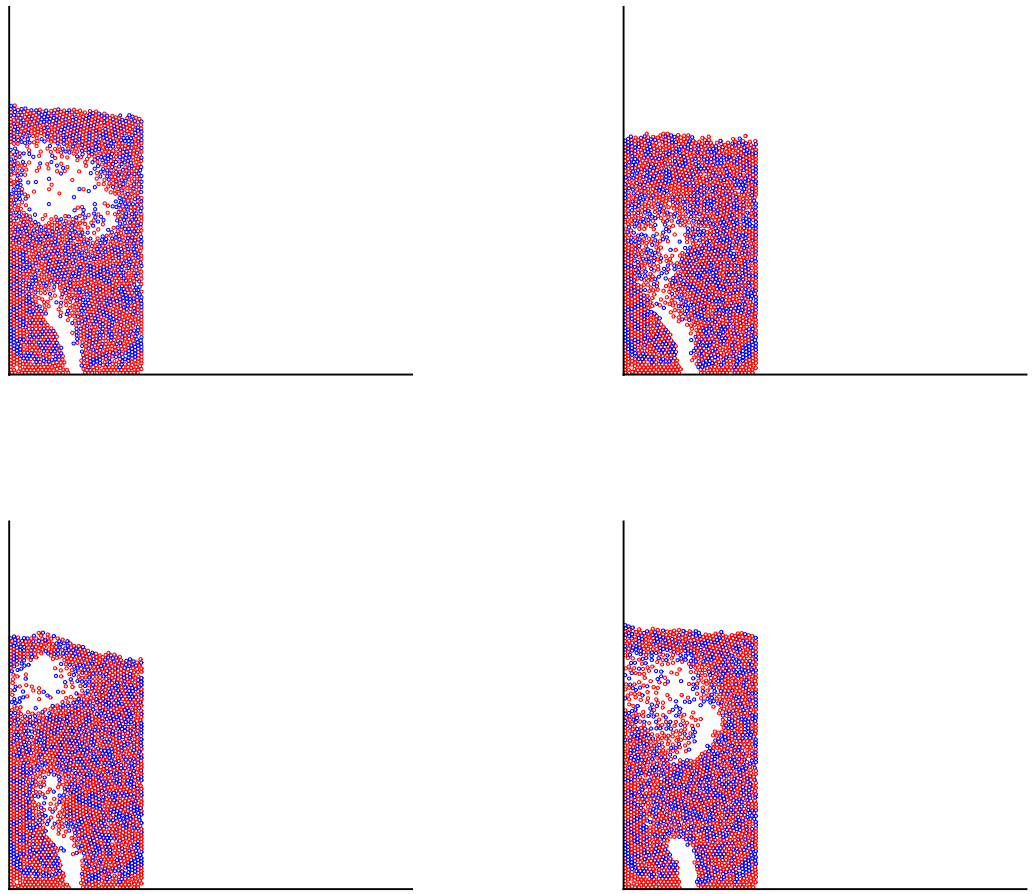

Figure 5.7. Fluidized bed simulated using MFIX drag correlation. 10 snapshots are shown between the 6th and 8th simulation seconds. Superficial gas velocity is 2.8m/s.

(1)

(2)

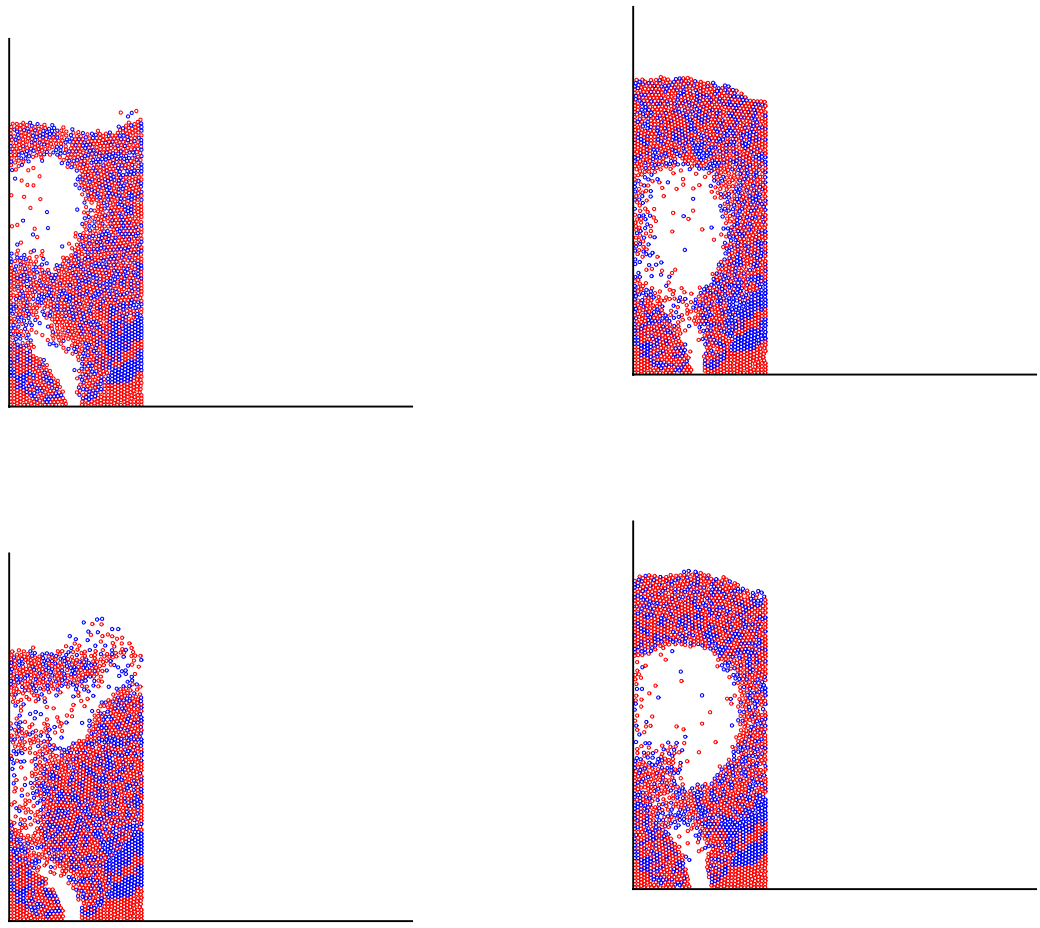

Figure 5.8. Fluidized bed simulated using Tsuji drag correlation. 12 snapshots are shown between the 6th and 8th simulation seconds. Superficial gas velocity is 2.8m/s. (Continued in next page)

(3)

(4)

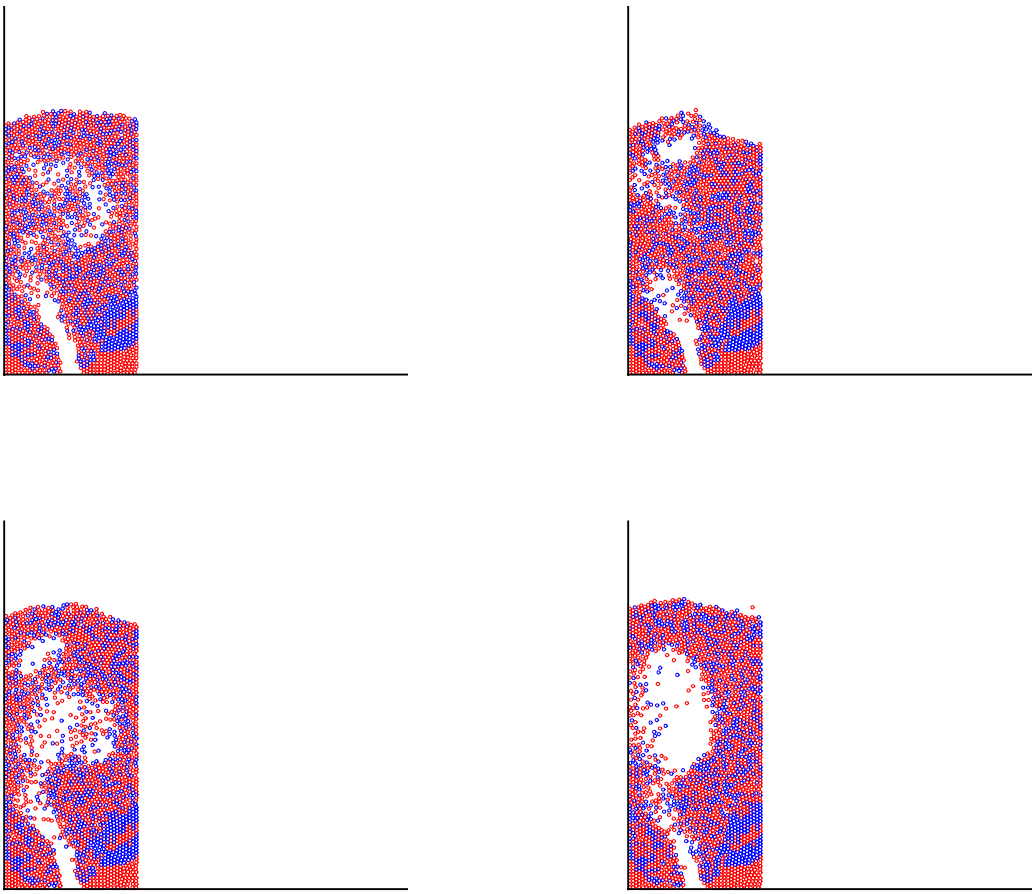

Figure 5.8. Fluidized bed simulated using Tsuji drag correlation. 12 snapshots are shown between the 6th and 8th simulation seconds. Superficial gas velocity is 2.8m/s.

(1)

(2)

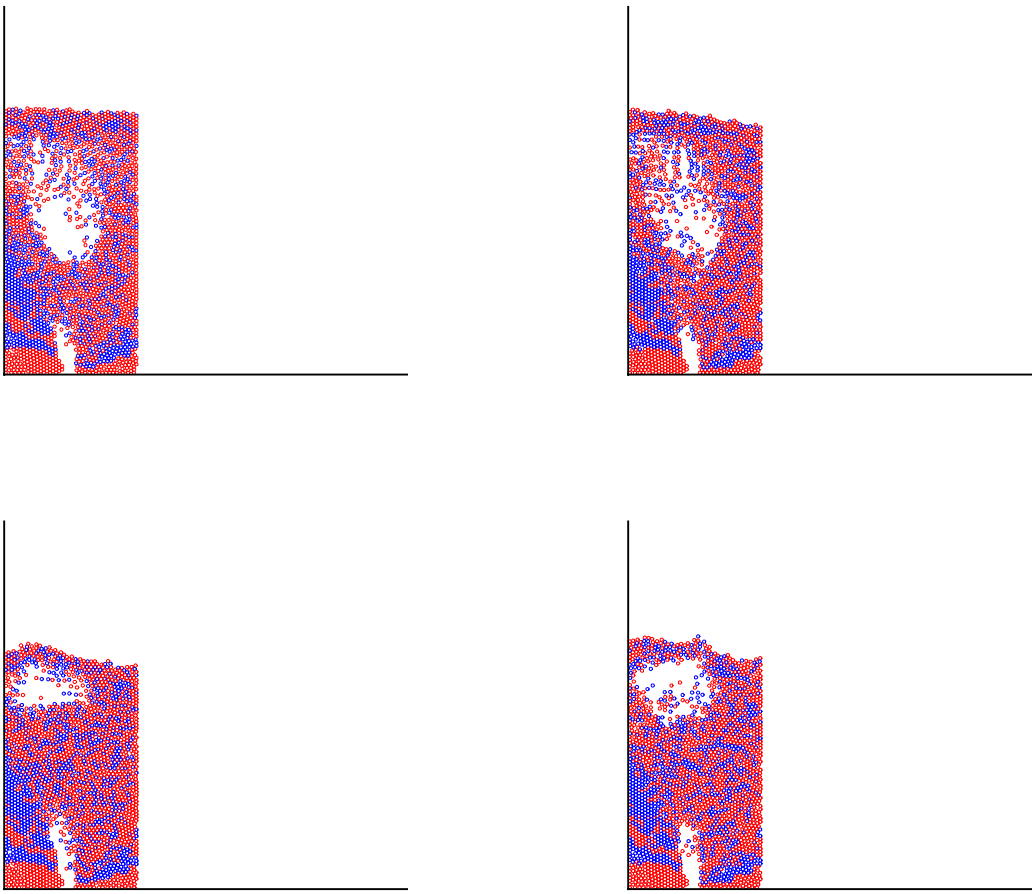

Figure 5.9. Fluidized bed simulated using Wen and Yu drag correlation for $\alpha = 4.7$. 12 snapshots are shown between the 6^{th} and 8^{th} simulation seconds. Superficial gas velocity is 2.8m/s. (Continued in next page)

(3)

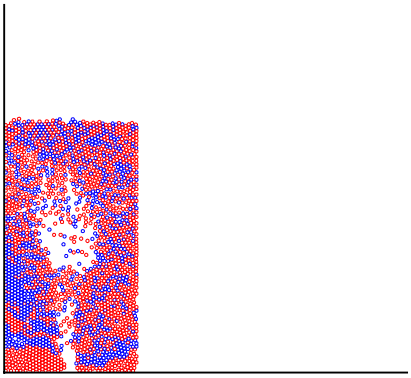

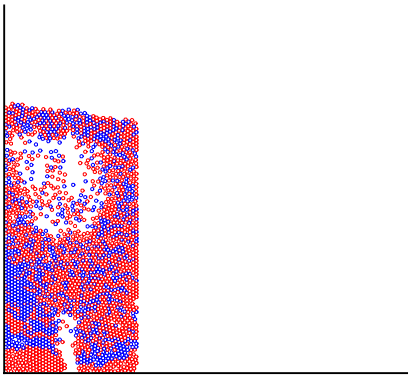

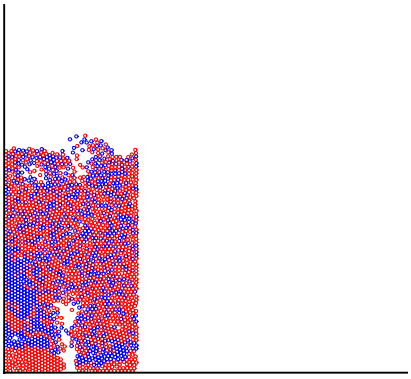

(4)

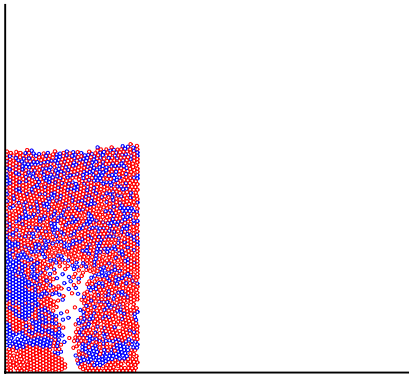

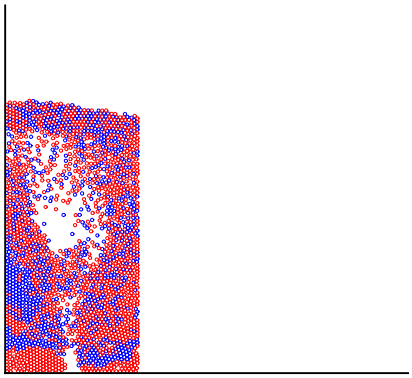

Figure 5.9. Fluidized bed simulated using Wen and Yu drag correlation for $\alpha = 4.7$. 12 snapshots are shown between the 6^{th} and 8^{th} simulation seconds. Superficial gas velocity is 2.8m/s.

(1)

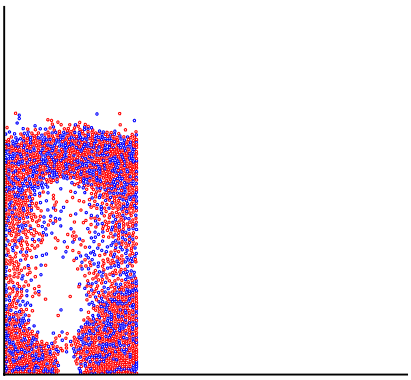

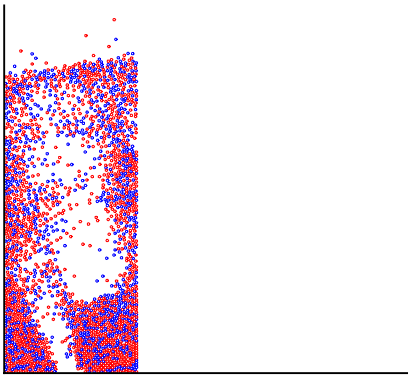

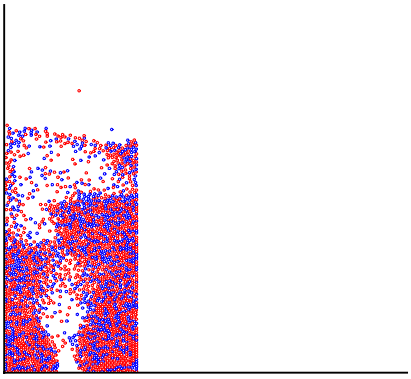

(2)

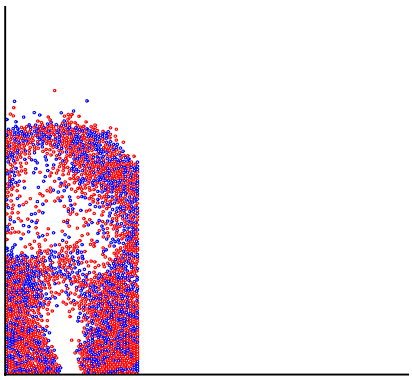

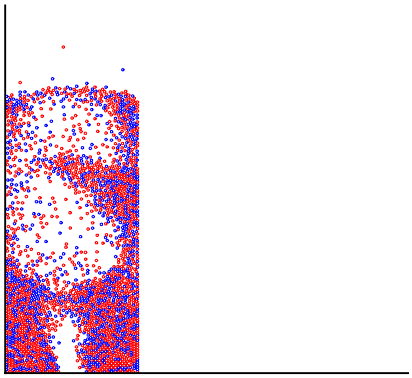

Figure 5.10. Fluidized bed simulated using Wen and Yu drag correlation for $\alpha = 8$. 12 snapshots are shown between the 6^{th} and 8^{th} simulation seconds. Superficial gas velocity is 2.8m/s.

(Continued in next page)

(3)

(4)

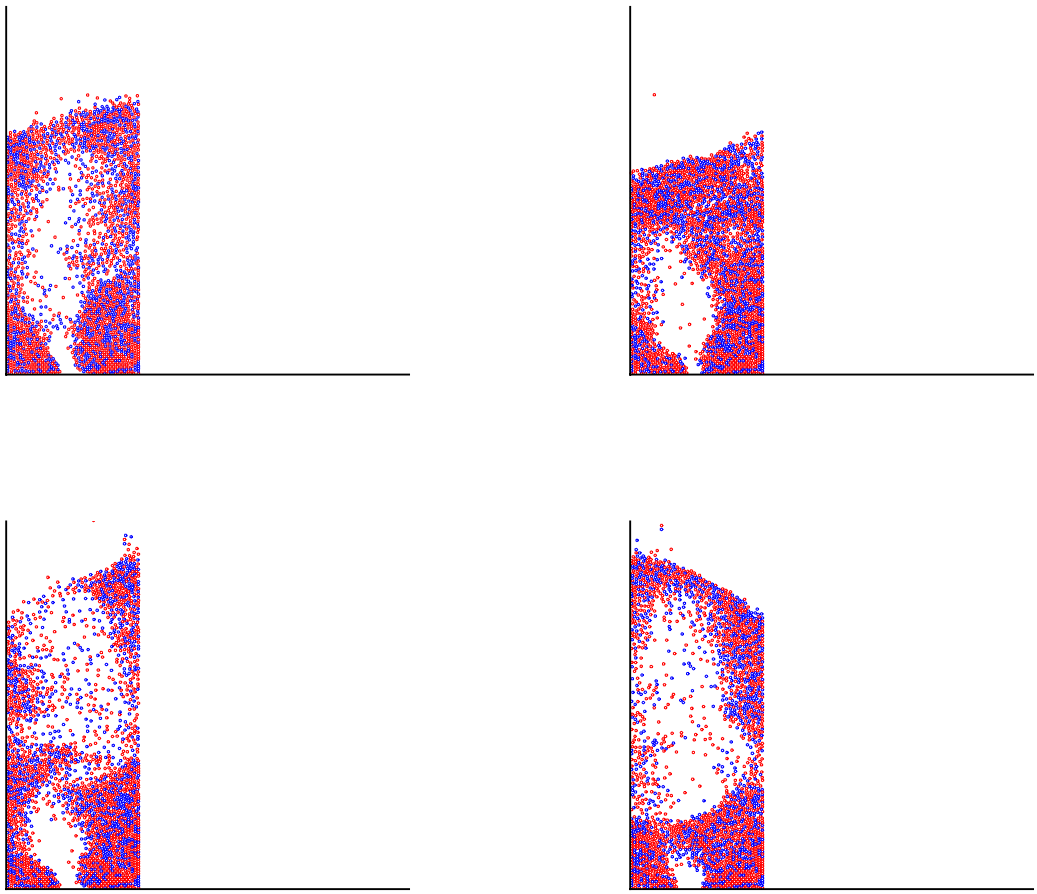

Figure 5.10. Fluidized bed simulated using Wen and Yu drag correlation for $\alpha = 8$. 12 snapshots are shown between the 6^{th} and 8^{th} simulation seconds. Superficial gas velocity is 2.8m/s.

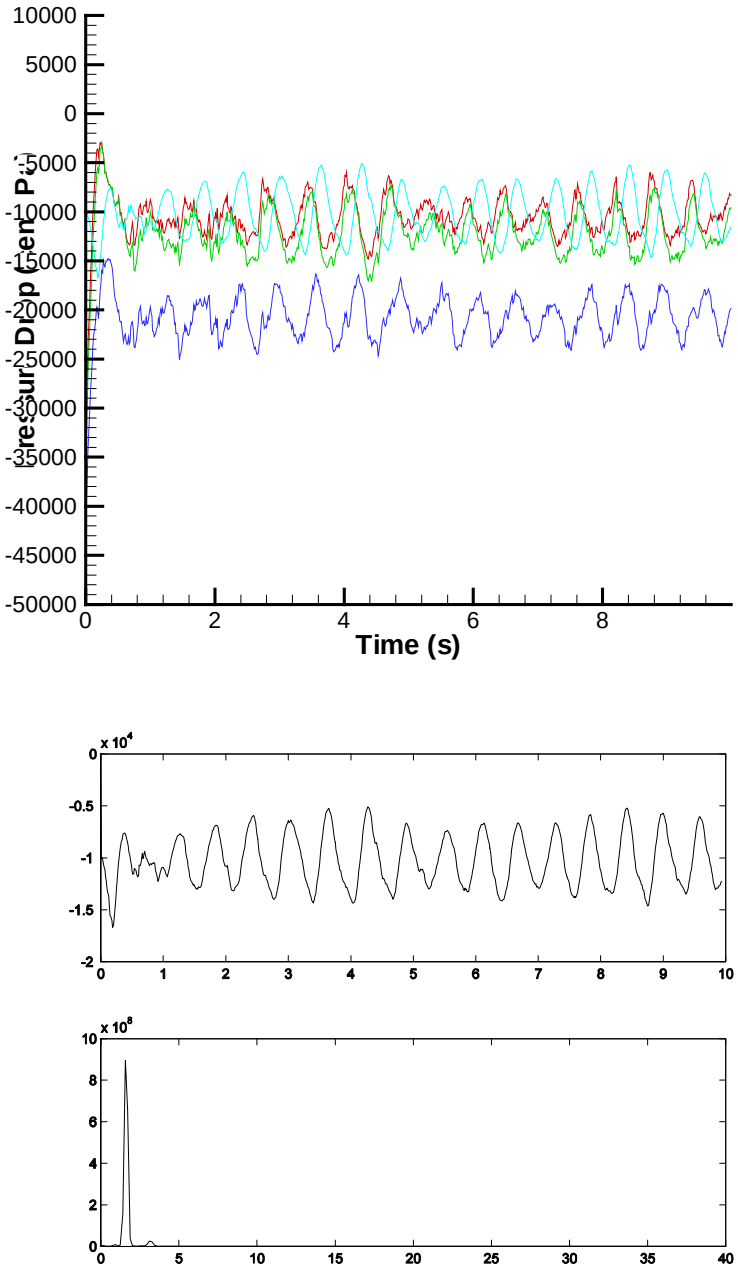

Figure 5.11. Pressure drop (centi Pascals) versus time for fluidized bed simulated using MFIX drag correlation. The middle plot is the pressure drop across the bed. Superficial gas velocity is 2.8 m/s. The frequency is plotted and is 2 per second.

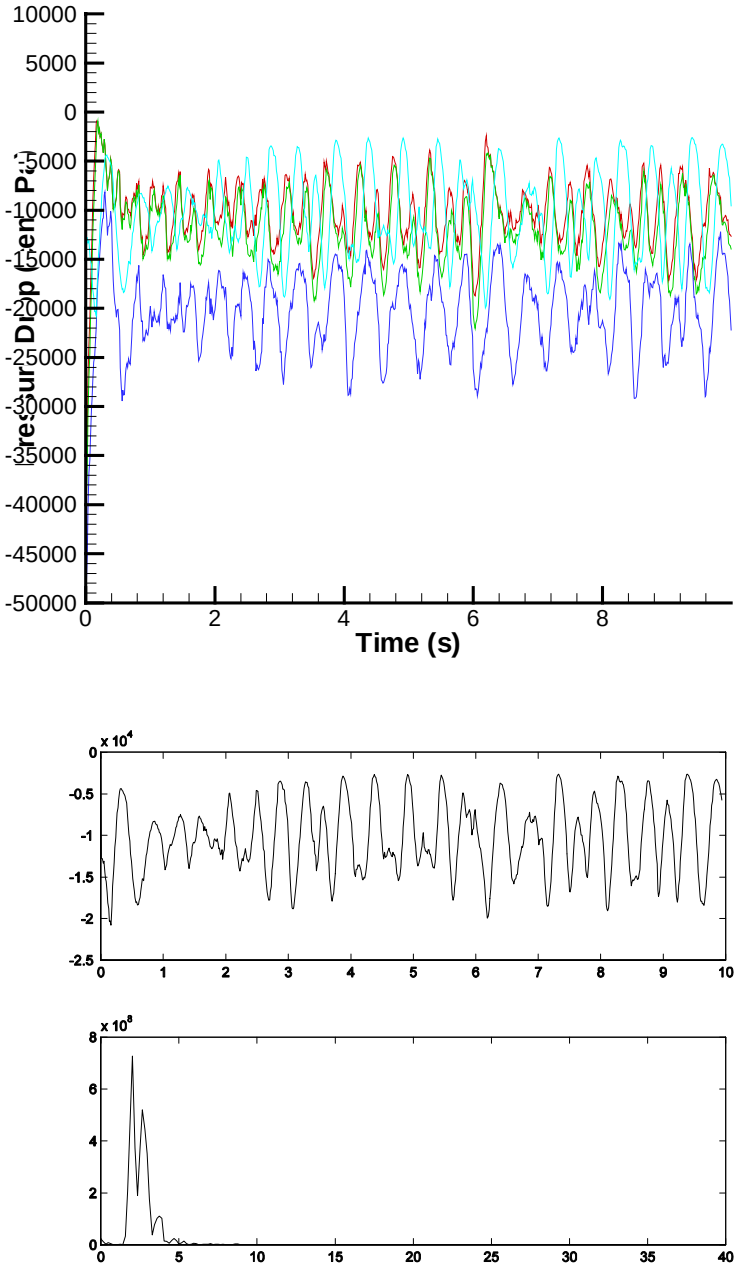

Figure 5.12. Pressure drop (centi Pascals) versus time for fluidized bed simulated using Tsuji drag correlation. The middle plot is the pressure drop across the bed. Superficial gas velocity is 2.8 m/s. The frequency is plotted and is 2 per second.

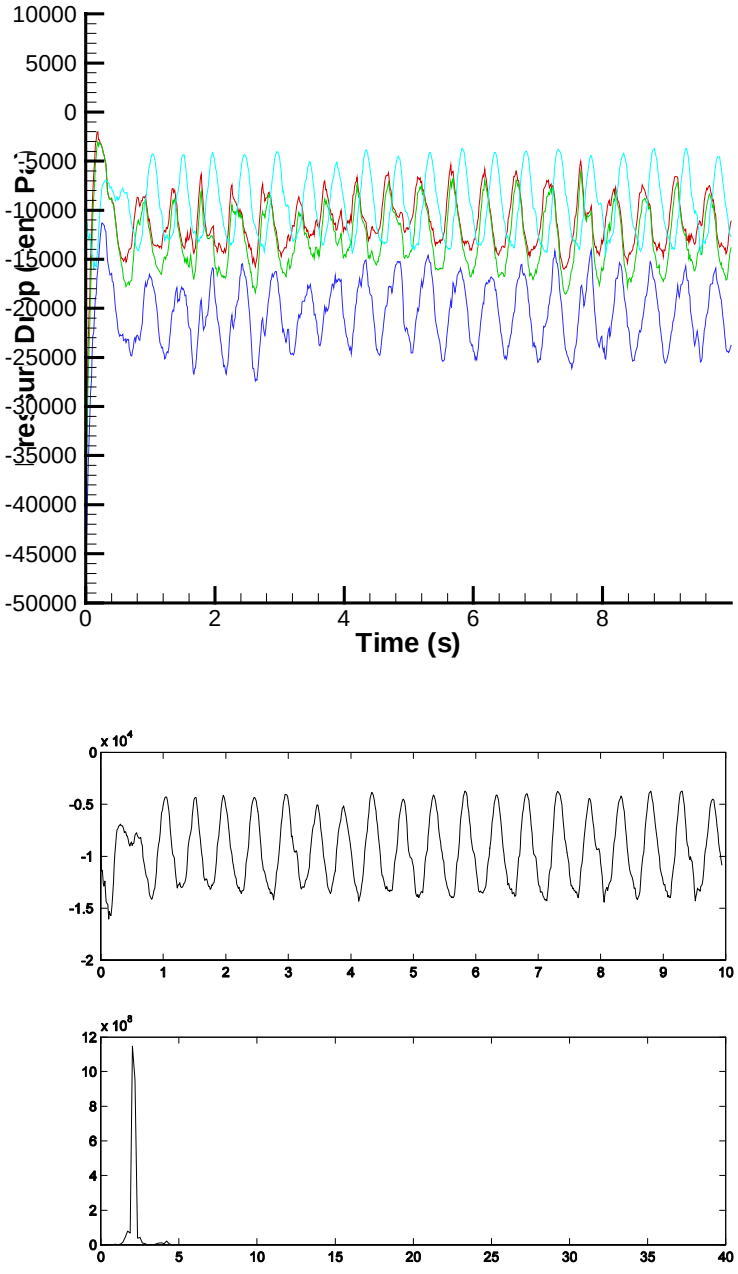

Figure 5.13. Pressure drop (centi Pascals) versus time for fluidized bed simulated using Wen and Yu drag correlation for $\alpha = 4.7$. The middle plot is the pressure drop across the bed. Superficial gas velocity is 2.8 m/s. The frequency is plotted and is 2 per second.

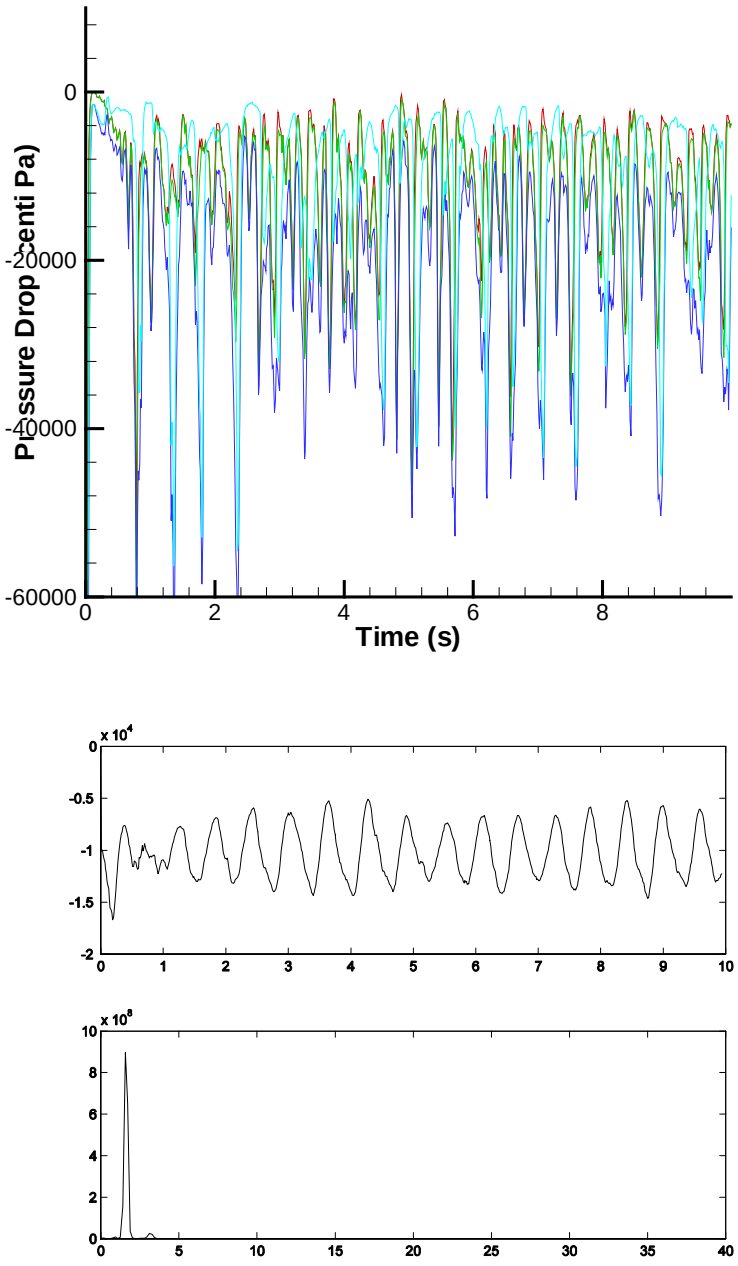

Figure 5.14. Pressure drop (centi Pascals) versus time for fluidized bed simulated using Wen and Yu drag correlation for $\alpha = 8$. The middle plot is the pressure drop across the bed. Superficial gas velocity is 2.8 m/s. The frequency is plotted and is 2 per second.

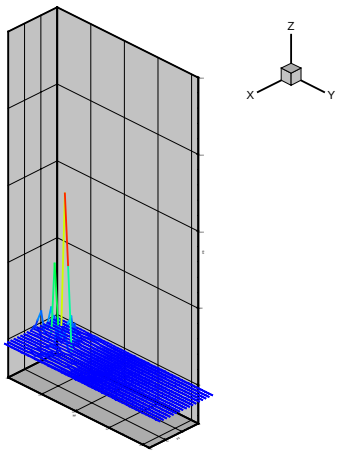

(a)

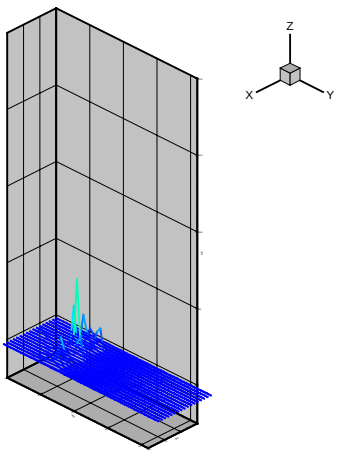

(c)

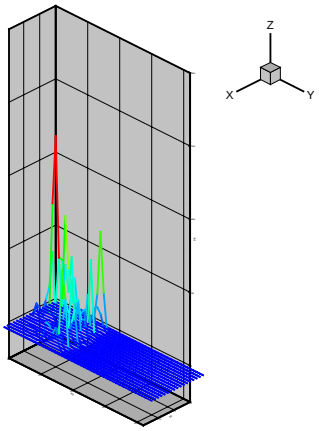

(b)

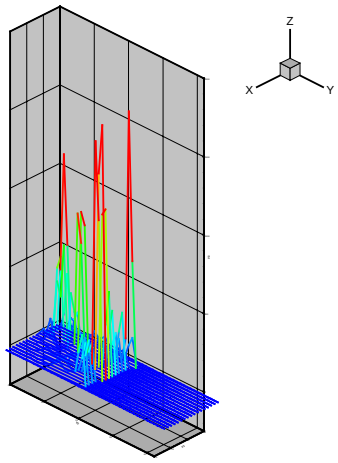

(d)

Figure 5.15. Granular temperature plots for the fluidized beds simulated using (a) MFIX drag correlation (b) Tsuji drag correlation (c) Wen and Yu's drag correlation of $\alpha = 4.7$ and (d) $\alpha = 8$ at t=9s. The fluidized bed is in XY plane. Inlet to outlet is in the positive y direction. Granular temperature is plotted in the Z axis; range is from –250 to 2000 $(m/s)^2$.

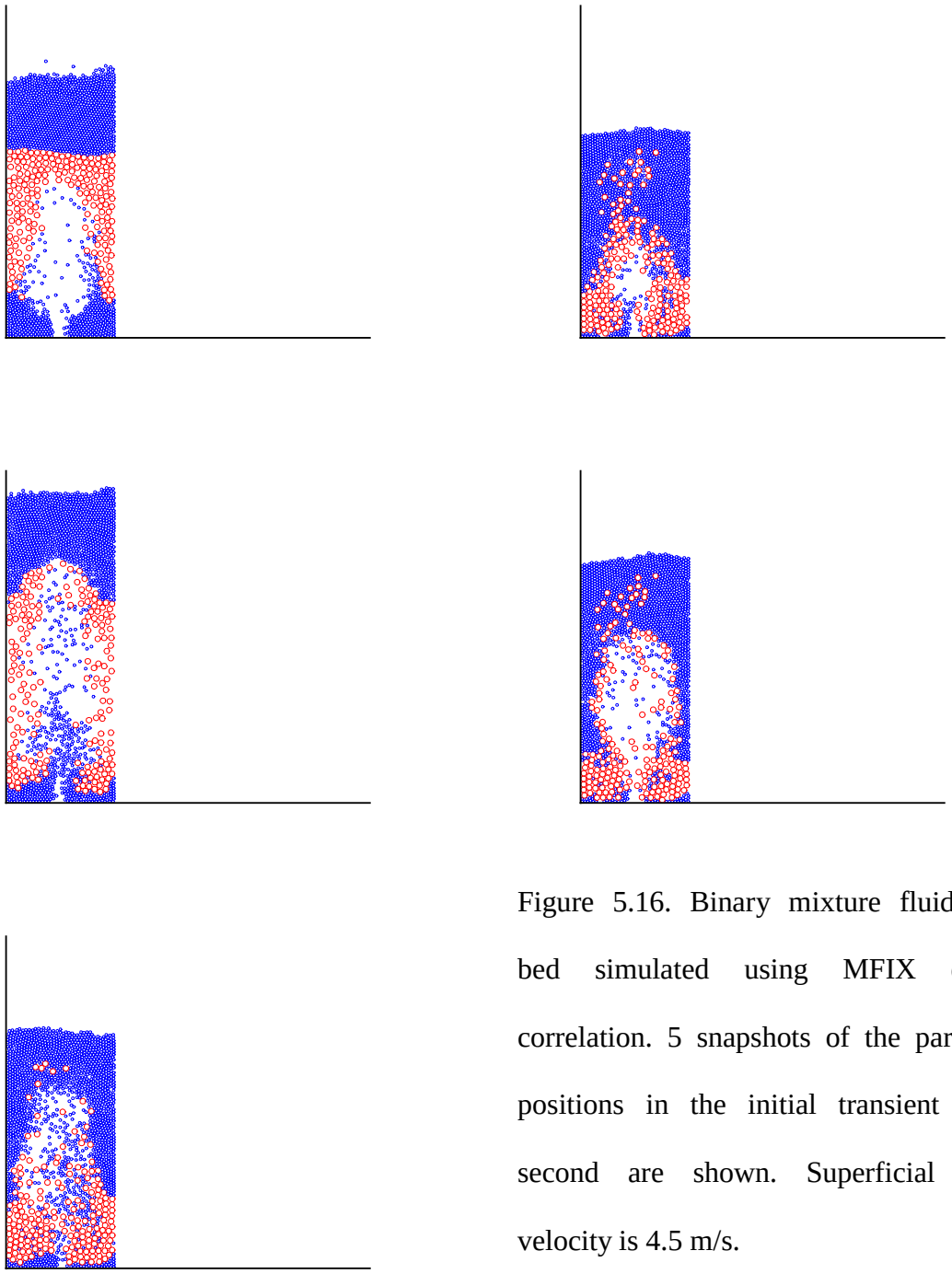

Figure 5.16. Binary mixture fluidized bed simulated using MFIX drag correlation. 5 snapshots of the particle positions in the initial transient one second are shown. Superficial gas velocity is 4.5 m/s.

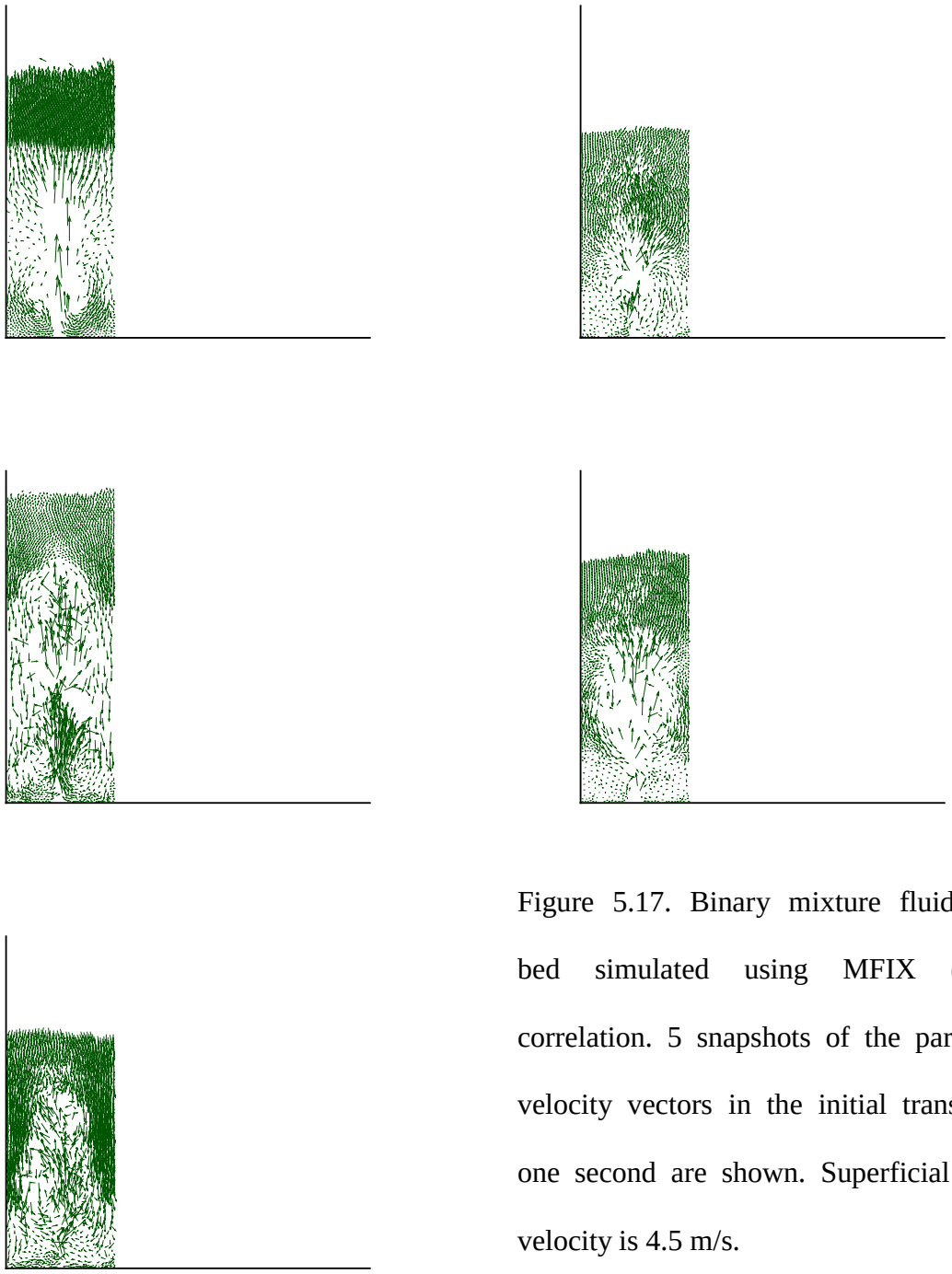

Figure 5.17. Binary mixture fluidized bed simulated using MFIX drag correlation. 5 snapshots of the particle velocity vectors in the initial transient one second are shown. Superficial gas velocity is 4.5 m/s.

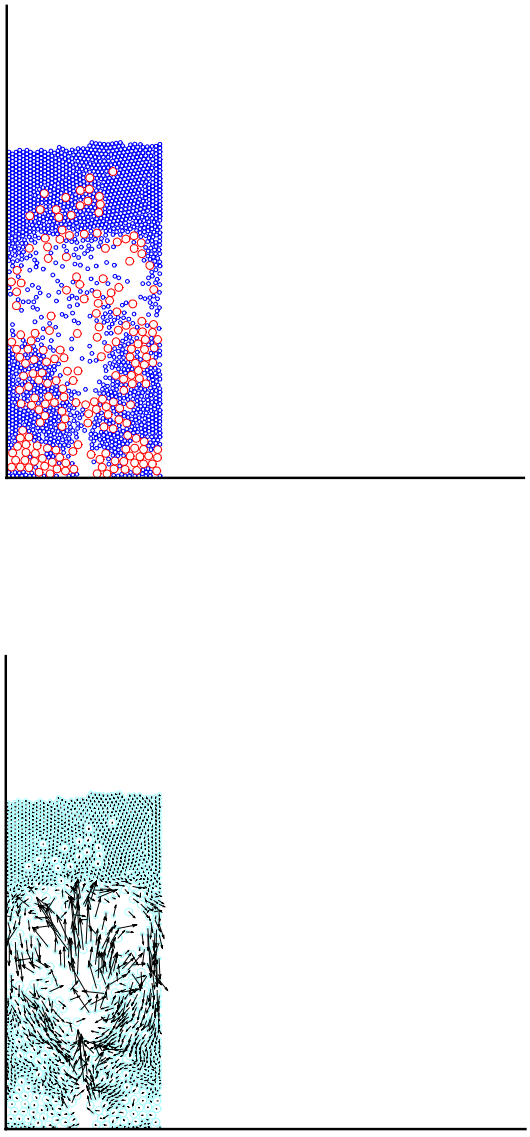

Figure 5.18. Binary mixture fluidized bed simulated using MFIX drag correlation. Snapshot of the particle positions at the end of 3 seconds and the corresponding velocity vectors are shown. Segregation and slug formation can be seen. Superficial gas velocity is 4.5 m/s.

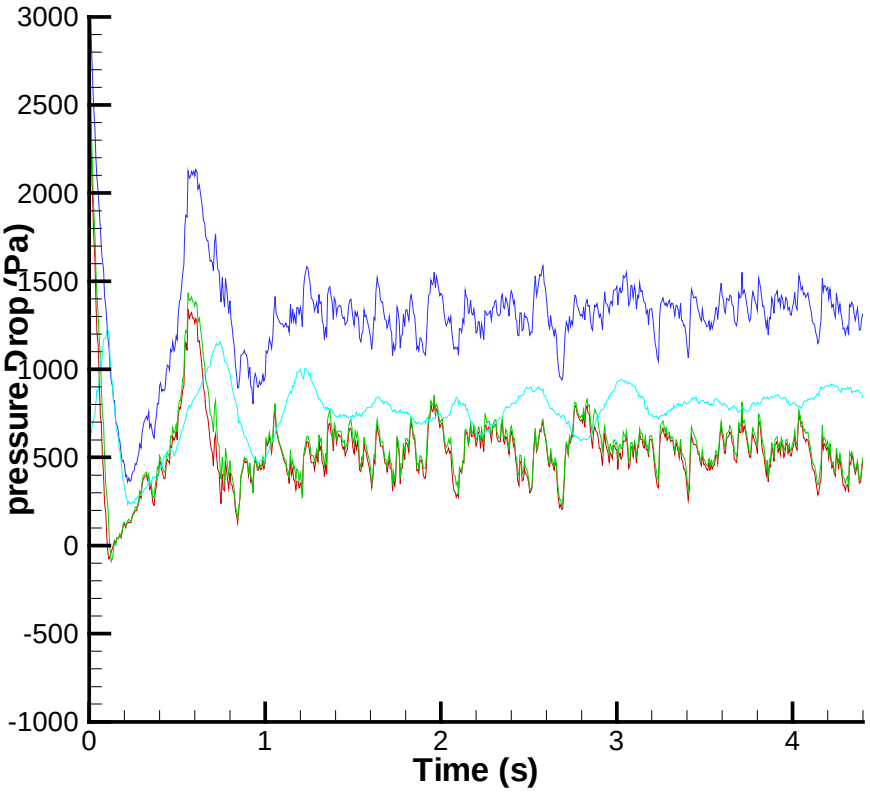

Figure 5.19. Pressure drop (Pa) versus time (s) in a binary mixture fluidized bed for superficial velocity of 4.5 m/s. Pressure drop at various heights from the bottom of the bed. The pressure drop range across the bed can be seen to be about 300 Pa.

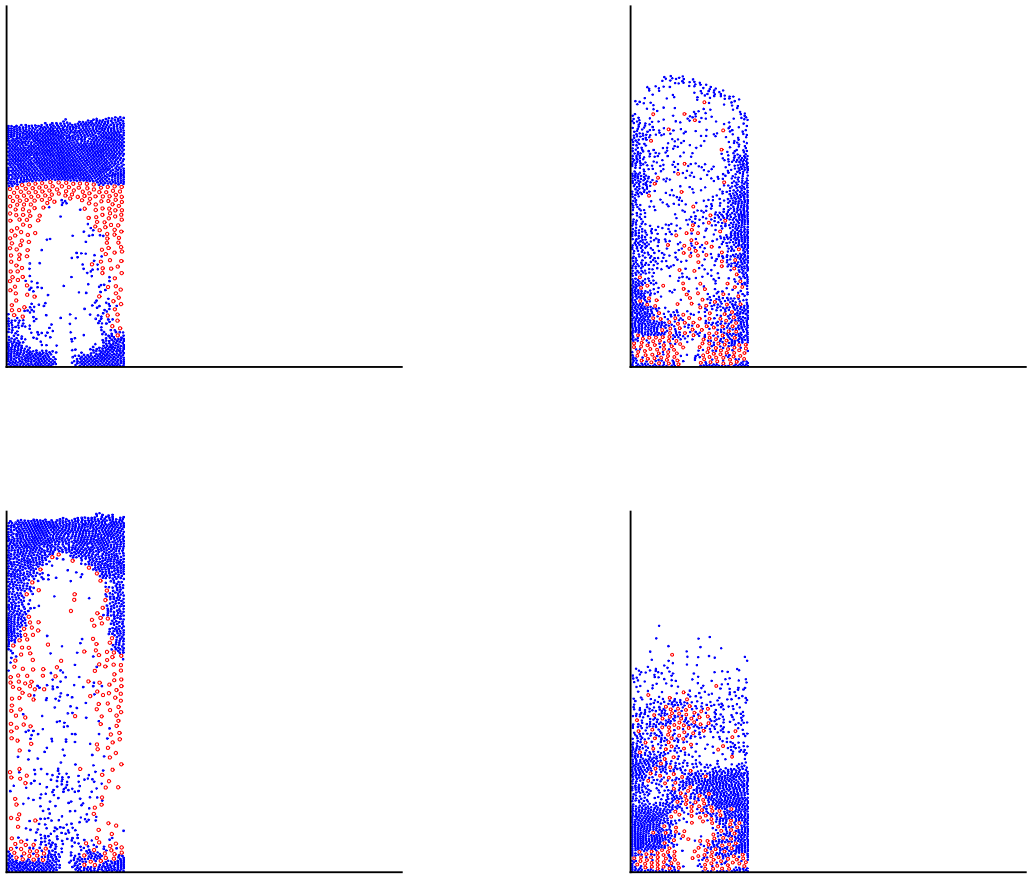

Figure 5.20. Binary mixture fluidized bed simulated using MFIX drag correlation. 5 snapshots of the particle positions in the initial transient one second are shown. Superficial gas velocity is 6 m/s.

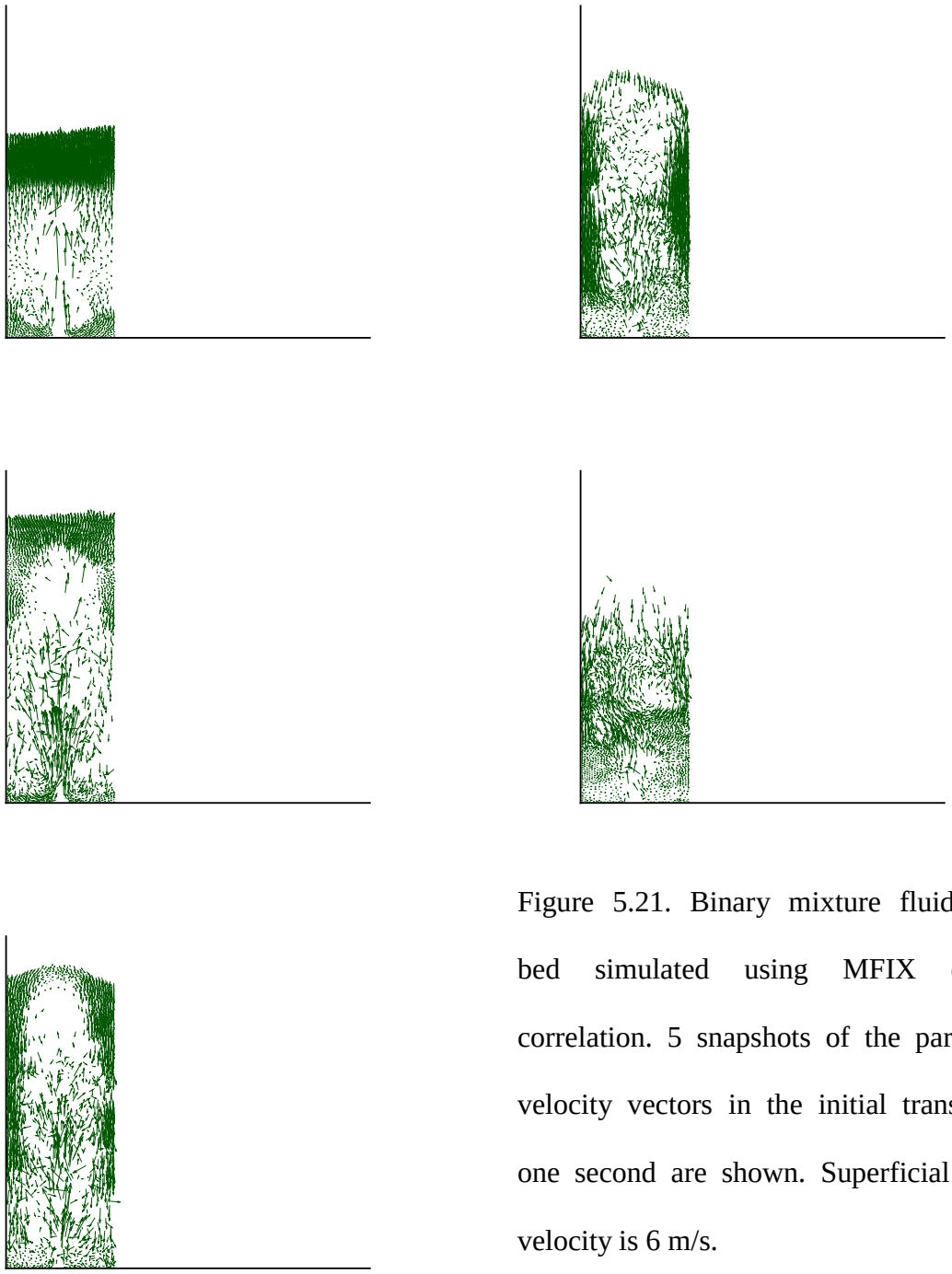

Figure 5.21. Binary mixture fluidized bed simulated using MFIX drag correlation. 5 snapshots of the particle velocity vectors in the initial transient one second are shown. Superficial gas velocity is 6 m/s.

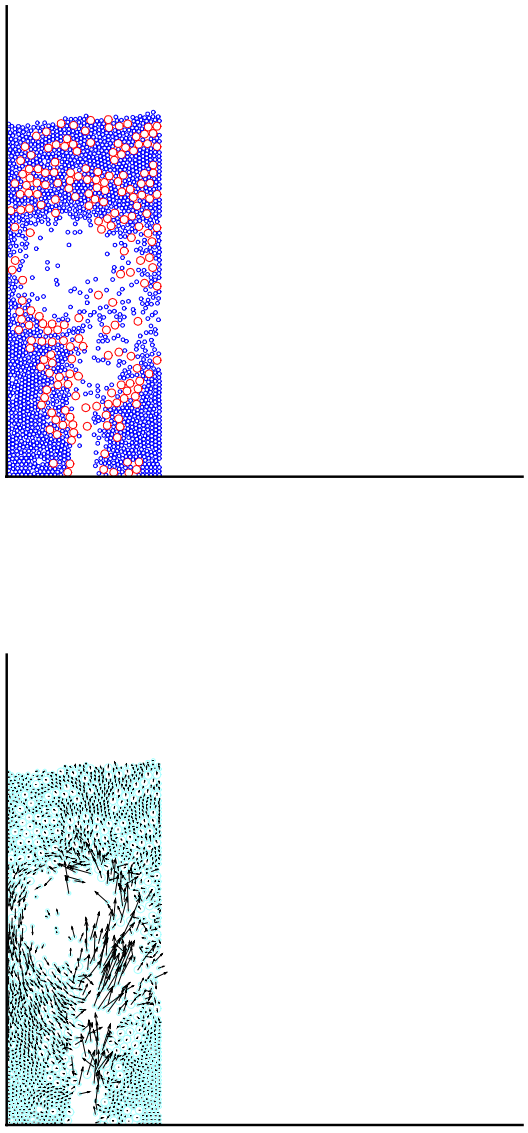

Figure 5.22. Binary mixture fluidized bed simulated using MFIX drag correlation. Snapshot of the particle positions at the end of 3 seconds and the corresponding velocity vectors are shown. Mixing and slug formation can be seen. Superficial gas velocity is 6 m/s.

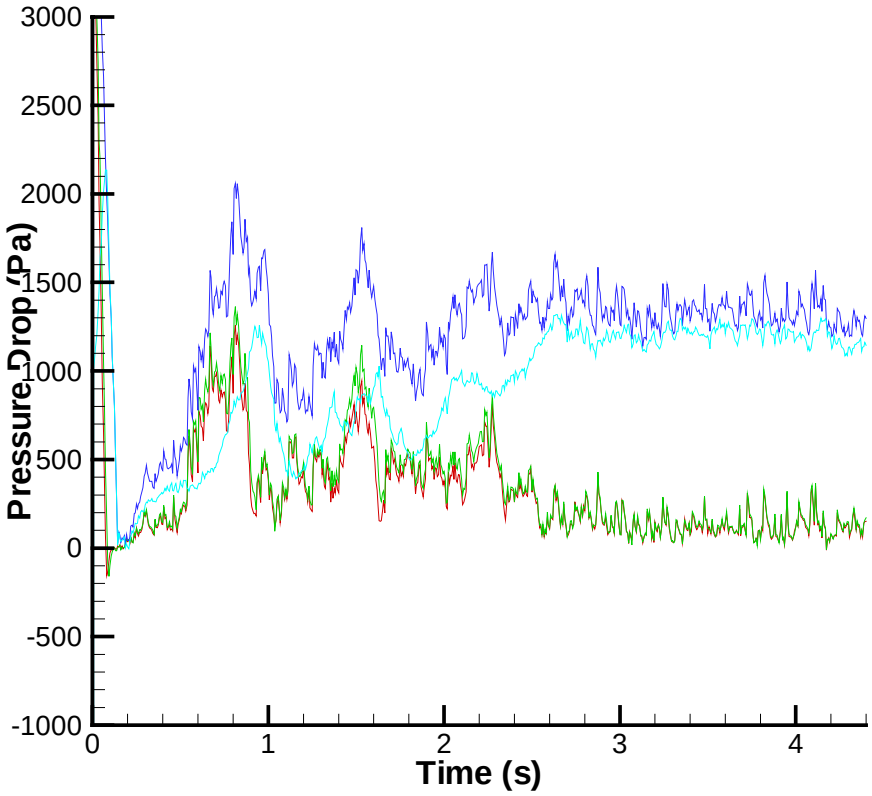

Figure 5.23. Pressure drop (Pa) versus time (s) in a binary mixture fluidized bed for superficial velocity of 6 m/s. Pressure drop at various heights from the bottom of the bed. The pressure drop range across the bed can be seen to be about 300 Pa.

Chapter 6

Summary and Recommendations

The present thesis has addressed the simulation of gas-solid flows by combining discrete element simulation (DES) with a computational fluid dynamic (CFD) simulation of the gas phase. A soft sphere model for DES was implemented and used to simulate various observed phenomena in pure granular flows. These included a study of vibrated granular beds consisting of single-sized particles as well as binary mixtures. DES for the solid phase was then coupled to continuum simulations of the gas phase. The coupled solver was used to simulate fluidized beds. The effect of various drag correlations on the bed simulations was studied. Simulation of fluidized beds containing binary mixtures was also performed.

A brief overview of thesis work done and recommendations for future work are presented in the following sections.

6.1. Overview of the Thesis

6.1.1. Discrete Element Simulations

The objective of the first phase of the thesis was to compute the particle trajectories in a pure granular system with no gas/fluid interaction. The following steps explain the work done in this area.

DES Soft-Sphere Model: The discrete element method which uses Newton's laws to track a solid particle has been implemented. Inter-particle collisions and particle-wall collisions were modeled using the soft-sphere model. The deformation during contact was

accounted for by considering particle overlap during collisions. The normal and tangential forces were computed using a spring-damper-slider model. The model accounts for particle sliding and rotation. The key parameters in discrete element simulations (DES) are the spring stiffness constant and the damping coefficient, as they determine the value of contact forces computed. The spring stiffness constant and the damping coefficient impose a limit on the solid time step for computations. The solid time step is typically about a millionth of a second making DES very time consuming.

Neighbor Search: Determining the neighbors of every particle in the system at every time instant is necessary to find contact forces. Efficient, effective and faster algorithms other than the basic N^2 search, like octree/quadtree and No-Binary search (NBS) have been implemented for neighbor searching. NBS is applicable only for systems of similar sized particles where as the octree/quadtree algorithms are indifferent to the particle size. NBS provides searches in O(N) operations, whereas the octree/quadtree algorithms are O(NlogN).

Vibrated Granular Bed Validation: Pure granular material behavior has been studied for the case of vibrated beds. The granular material bed floor is vibrated sinusoidally with a specified frequency and amplitude. Benchmark cases have been simulated to validate the code and the results have been matched with the published literature. The factors governing vibrated bed behavior are the non-dimensional acceleration amplitude and the non-dimensional bed height. For a given granular bed height, for a range of acceleration amplitudes, various interesting behaviors like heaping, round and cusp surface standing

waves and kinks have been observed. The ranges of bed heights and acceleration amplitudes and also the theory explaining the formation of these phenomena have been confirmed from the simulations.

Vibrated Binary Mixture Simulations: Granular mixtures with two particle sizes in a vibrated bed have also been studied. In the kink formation regime the binary mixtures have been found to demonstrate horizontal segregation, wherein the bigger particles cluster at the kinks thus forming alternating sections of big and small particles. This type of horizontal segregation is explained by the convection cells that occur in kinks.

6.1.2 Coupled Gas-Solid Simulations

The objective of the second phase of the thesis is to couple the particle trajectories to gas/liquid flow, by using DES for the solid phase and MFIX for the continuum gas phase. MFIX contains a capability to simulate incompressible Newtonian flow in 2D and 3D. At present, it contains a kinetic-theory based model for granular flows; DES forms a more accurate alternative to this theory. The following steps have been implemented in this phase of the work.

Calculation of Solids Volume Fraction in the Fluid Cell: Each particle from the DES simulation is located within the fluid control volume; the sum of all particle volumes in the cell yields the solid volume fraction. The particles are classified by size to feed into the multiple-phase capability of MFIX. This requires the computation of several solids

volume fractions per cell. Once the volume fraction is made available to MFIX, blockage effects are automatically taken care of.

Calculation of Averaged Solids Velocity in the Fluid Cell: All the particles in a fluid cell are identified. The velocities of individual particles of a given size are volume-averaged to obtain a single representative solids velocity in the cell. The volume- averaged solids velocity thus obtained are used by MFIX to compute interphase drag.

Calculation of Gas-Solid Interaction: Though a variety of interaction forces couple the gas and solid, the focus in the present work is on the simulation of gas-particle flows for fluidized bed applications. Two interaction forces which are the most dominant for this application, namely interphase drag and buoyancy, have been considered. Since the gas-phase mesh is much larger than the individual particle, it is not possible to resolve the drag numerically. The interphase drag has been computed from experimental correlations for fluidized beds. An important issue in the development is to ensure that the gas and solid drag are equal and opposite to each other, so that net momentum is conserved. Various drag correlations used in literature have been implemented and tested.

Coupling Algorithm for Gas-Solid Flows: A sequential and iterative procedure for coupling the two calculations has been used. Far larger time-steps have been used for the gas than the solid, since the gas has no explicit time-stepping limitations. At every gas-phase time-step, several DES sub-steps are taken and the volume fraction computed at the end of the sub-steps. The gas flow is assumed stationary at old values during this sub-

stepping. Then the gas flow is iterated to convergence within the time step. The procedure is repeated until the desired time interval is covered.

Fluidized Bed Validation: Benchmark 2D fluidized beds have been simulated. Global parameters of interest such as the pressure drop across the bed over time and the bubbling frequency have been matched satisfactorily.

Investigation of the Effect of Drag Correlations on Fluidized Bed: Various drag correlations used in literature have been implemented and their effect on the 2D simulation results has been studied. It is found that all the correlations studied predict similar values of global quantities such as the bed pressure drop and bubbling frequency. But they differ in predicting the local bed behavior.

Binary Mixture Fluidized Bed Simulation: Fluidized Beds with binary mixtures have also been simulated in 2D. Segregation is predominantly seen at the bed base for superficial velocities close to the minimum fluidization velocity.

6.2. Recommendations for Future Work

Some recommendations for future work in this area are listed below.

Computational investigation of canonical gas-solid flows: The DES-MFIX coupled code is a powerful tool to investigate various gas-solids flow phenomena. Of particular interest is the investigation of cluster formation in riser flows. It has been observed both

experimentally and computationally that gas-solid flows are inherently unsteady, and over time, tend to aggregate into clusters or streak-like structures. A number of mechanisms have been postulated for this phenomenon, and all may be active to a greater or lesser extent. An important phenomenon is clustering due to drag. The presence of particles tends to form wakes in which other particles congregate. This is represented approximately by the drag correlations implemented here. The second reason for clustering could be inelastic collapse. Since particle-particle interactions are inelastic, the loss of energy during collision results in particles clustering together. A third possible mechanism is turbulent segregation. For dilute enough concentrations, turbulent eddies tend to segregate particles into low velocity regions between eddies. It is as yet unclear which of these mechanisms acts over what range of parameters, and all seem to be active to a greater or lesser extent. The code developed here can be used to explicitly test the influence of some of these mechanisms individually. The influence of particle properties, particle size and size distribution on cluster formation are of particular interest. To be of real interest, these computations must be done in three dimensions. In practical terms, it is likely that a combination of 2D and 3D calculations need to be performed.

3D Simulations: Though the code developed in the present work has both 2D and 3D capabilities, only 2D simulations have been done due to computational time limitations. For more realistic simulations and more significant contributions to gas-solid flows, 3D simulations need to be performed. To simulate the same solids volume fraction, a larger number of particles must be simulated, substantially increasing the computational cost. However, the computational models and the solution algorithm would remain the same.

Parallelization of DES: Parallel computing must be exploited for realistic gas-solid flow simulations. This is because as the particle number increases, the computation time increases drastically and hence the cost. Strategies for parallel DES must be explored. Coupling of parallel DES and parallel continuum simulations must also be performed.

Comparison with Other Theories: To be useful to the researcher, the DES results at each time step should be able to obtain temporally or spatially-averaged quantities. These include quantities like the solids stress tensor and granular temperature, which are useful for comparison with competing theories for granular flow. Though some of these capabilities (such as the granular temperature calculation) have been implemented, more detailed output quantities would be useful.

DES for Complex Particle Shapes: DES for spherical particles is implemented in the present work. Though this gives good insight into granular material and gas-solid flow behavior, for practical purposes it would be of interest to implement other shapes like ellipsoids, chains, and rods. Calculation times increase substantially as contact detection and drag force calculations become more complicated. Approximate representations of particle shape using agglomerations of spherical particles should be explored as an alternative. Of particular interest to the chemical process industry would be mixing and segregation behavior of particle systems of different particle shapes.

DES for Nano-Fluids: Nano-fluids are essentially suspensions of nano-sized particles and carbon nanotubes in fluids, and have been know to exhibit substantial increases in thermal conductivity. Extending the DES technique to include other forces such as electrostatic, Brownian, and Van der Waals forces would yield a powerful tool for analyzing and understanding this class of fluids

Other Chemical Processes: Many other chemical processes such as particle coating, particle growth, gasification etc., which are performed in a fluidized bed, may be simulated for better understanding.

Appendix

Description of MFIX

Multiphase Flow with Interphase eXchange (MFIX) is a general-purpose hydrodynamic code, which solves for multiphase flows in energy conversion and chemical processing applications (MFIX Theory Guide, User's Manual: Syamlal et al, 1994). It addresses both dense and dilute gas-solid flows as well as species transport, chemical reactions and heat transfer. It is written in FORTRAN 90 and admits three-dimensional Cartesian and cylindrical coordinate systems with non-uniform grids. MFIX admits a single fluid phase and several solid phases. A continuum approach is taken for both fluid and solid phases, which are treated as interpenetrating continua. The fluid phase is considered to be a Newtonian, incompressible flow, and can be either laminar or turbulent. Each solid phase is tracked separately, and is described by its own momentum and mass conservation equations. At present, a kinetic theory treatment of the solid phase stresses is adopted (Lun et al, 1984). The discrete element simulation (DES) serves as a replacement the kinetic theory model for the solid stresses, as well as the present procedure for computing solid-phase volume fractions and other solids related values. The fluid phase governing equations and calculation procedure are described below.

1. Gas-Phase Governing Equations

The governing equations for the gas phase are given below.

Conservation of Mass

$$\frac{\partial}{\partial t}(\varepsilon_g \rho_g) + \nabla \cdot (\varepsilon_g \rho_g \vec{v}_g) = \sum_{n=1}^{N_g} R_{gn}$$

The first term in the left hand side of the above equation is the rate of mass accumulation per unit volume and the second term is the net rate of mass flux. Both the terms on left account for the gas void fraction. The term on the right hand side is the interphase mass transfer.

Conservation of Momentum

$$\frac{\partial}{\partial t}(\varepsilon_g \rho_g \vec{v}_g) + \nabla \cdot (\varepsilon_g \rho_g \vec{v}_g \vec{v}_g) = \nabla \cdot \bar{\bar{S}}_g + \varepsilon_g \rho_g \vec{g} - \sum_{m=1}^{M} \vec{I}_{gm} + \vec{f}_g$$

The first term in the left hand side of the above equation is the rate of momentum accumulation per unit volume and the second term is the net rate of momentum flux. Both the terms on left account for the gas void fraction. The first term on the right hand side is the gas-phase stress tensor, the second term is the body force, the third term is the interaction force representing the momentum transfer between the gas phase and the mth solid phase and the last term is the flow resistance.

The interaction force between the gas phase and the mth phase solid is given by

$$\vec{I}_{gm} = -\varepsilon_g \nabla P_g - F_{gm}(\vec{v}_{sm} - \vec{v}_g) - R_{0m}[\xi_{0m}\vec{v}_{sm} + \bar{\xi}_{0m}\vec{v}_g]$$

The first term on the right hand side is the buoyancy force, the second term is the drag force and the third term describes the momentum transfer from gas phase to solids phase.

In all the above equations, ε_g **i**s the gas phase void fraction, ρ_g is the gas density, v_g is the gas velocity vector, v_{sm} is the velocity vector of the mth phase solid.

2. Gas Phase Numerical Method

The numerical technique used for the gas phase in MFIX is based on the finite volume technique. The domain is divided into control volumes, each typically containing a large number of particles. Balances of mass, momentum, energy and species are written for these control volumes. Second-order discretization operators are used for both convection and diffusion terms, including a variety of second-order limited schemes for convection. A fully-implicit time stepping schemes with automatic time-step control has also been implemented. Pressure-velocity coupling in the gas phase is through the SIMPLE algorithm (Patankar, 1980). A variety of linear solvers, including a preconditioned conjugate gradient method and GMRES are available. MFIX uses a structured mesh, either Cartesian or cylindrical, in either 2D or 3D. All transported scalars are stored at cell centroids. A staggered-velocity formulation is used. Both gas and solids velocities are stored at cell faces, and the gas and solids pressures are stored at cell centroids. The equations described above may be cast into the form of a general convection-diffusion equation (Patankar, 1980).

2.1. Discretization of Convection-Diffusion Terms

For simplicity, we consider a 1-D situation. The transport equations contain convection-diffusion terms of the form

$$\frac{\partial(\rho u \phi)}{\partial x} - \frac{\partial}{\partial x}(\Gamma \frac{\partial \phi}{\partial x})$$

The domain is divided into rectangular control volumes. The convection-diffusion equation is integrated over the control volume (CV) to yield:

$$\int[\frac{\partial(\rho u\phi)}{\partial x}-\frac{\partial}{\partial x}(\Gamma\frac{\partial\phi}{\partial x})]dV=[\rho u\phi_e-(\Gamma\frac{\partial\phi}{\partial x})_e]A_e-[\rho u\phi_w-(\Gamma\frac{\partial\phi}{\partial x})_w]A_w$$

The diffusive flux at the east face can be approximated to second order accuracy by

$$(\Gamma\frac{\partial\phi}{\partial x})_e=\Gamma_e\frac{(\phi_E-\phi_P)}{\delta x_e}+O(\delta x^2)$$

For the convection terms, MFIX uses a general second-order discretization which can be made to default to a first-order upwind scheme if desired. The value of ϕ at the east face, for example, is written as

$$\phi_e=\xi_e\phi_E+\overline{\xi}_e\phi_P$$

where $\overline{\xi}_e=1-\xi_e$ and ξ_e is a weighting factor.

For the upwind discretization scheme

$$\xi_e=\begin{cases}0 & u_e\geq 0\\ 1 & u_e<0\end{cases}$$

The value of ϕ at the west face, for example, is then written as

$$\phi_w=\xi_w\phi_W+\overline{\xi}_w\phi_P$$

where $\overline{\xi}_w=1-\xi_w$

For the upwind discretization scheme

$$\xi_w=\begin{cases}1 & u_w\geq 0\\ 0 & u_w<0\end{cases}$$

MFIX provides a number of second-order accurate discretizations for the convection terms, which are essentially embodied in the ξ factor. Details can be found in (Syamlal, 1998).

2.2. Discretization of Scalar Transport Equation

We now turn to the discretization of a complete transport equation for a scalar ϕ:

$$\frac{\partial}{\partial t}(\varepsilon_m \rho_m \phi) + \frac{\partial}{\partial x_i}(\varepsilon_m \rho_m v_{mi} \phi) = \frac{\partial}{\partial x_i}(\Gamma_\phi \frac{\partial \phi}{\partial x_i}) + R_\phi$$

We integrate Equation (2.10) over a control volume and consider each term in turn. The terms from left to right are as follows:

Transient term:

Using a fully implicit scheme, we write

$$\int \frac{\partial}{\partial t}(\varepsilon_m \rho_m \phi) dV \approx [(\varepsilon_m \rho_m \phi)_P - (\varepsilon_m \rho_m \phi)_P^0] \frac{\Delta V}{\Delta t}$$

where the superscript 'o' indicates old (previous) time step values.

Convection term:

$$\begin{aligned}
\int \frac{\partial}{\partial x_i}(\varepsilon_m \rho_m v_{mi} \phi) dV \approx \\
&\{\xi_e (\varepsilon_m \rho_m \phi)_E + \overline{\xi}_e (\varepsilon_m \rho_m \phi)_P\}(u_m)_e A_e \\
&- \{\xi_w (\varepsilon_m \rho_m \phi)_P + \overline{\xi}_w (\varepsilon_m \rho_m \phi)_W\}(u_m)_w A_w \\
&+ \{\xi_n (\varepsilon_m \rho_m \phi)_N + \overline{\xi}_n (\varepsilon_m \rho_m \phi)_P\}(v_m)_n A_n \\
&- \{\xi_s (\varepsilon_m \rho_m \phi)_P + \overline{\xi}_s (\varepsilon_m \rho_m \phi)_S\}(v_m)_s A_s \\
&+ \{\xi_t (\varepsilon_m \rho_m \phi)_T + \overline{\xi}_t (\varepsilon_m \rho_m \phi)_P\}(w_m)_t A_t \\
&- \{\xi_b (\varepsilon_m \rho_m \phi)_P + \overline{\xi}_b (\varepsilon_m \rho_m \phi)_B\}(w_m)_b A_b
\end{aligned}$$

Diffusion term:

$$\begin{aligned}
\int \frac{\partial}{\partial x_i}(\Gamma_\phi \frac{\partial \phi}{\partial x_i}) dV \approx (\Gamma_\phi \frac{\partial \phi}{\partial x})_e A_e - (\Gamma_\phi \frac{\partial \phi}{\partial x})_w A_w \\
+ (\Gamma_\phi \frac{\partial \phi}{\partial y})_n A_n - (\Gamma_\phi \frac{\partial \phi}{\partial y})_s A_s \\
+ (\Gamma_\phi \frac{\partial \phi}{\partial z})_t A_t - (\Gamma_\phi \frac{\partial \phi}{\partial z})_b A_b
\end{aligned}$$

The diffusive fluxes are approximated using the method described previously. For example, the diffusive flux through the east face is given by

$$(\Gamma_\phi \frac{\partial \phi}{\partial x})_e \approx (\Gamma_\phi)_e \frac{\phi_E - \phi_P}{\Delta x_e}$$

The cell face values of diffusion coefficients are calculated using a harmonic mean of the values defined at the cell centers. For example,

$$(\Gamma_\phi)_e = [\frac{1-f_e}{(\Gamma_\phi)_P} + \frac{f_e}{(\Gamma_\phi)_E}]^{-1}$$
$$= \frac{(\Gamma_\phi)_P (\Gamma_\phi)_E}{f_e(\Gamma_\phi)_P + (1-f_e)(\Gamma_\phi)_E}$$

where we use the definition

$$f_e = \frac{\Delta x_E}{\Delta x_P + \Delta x_E}$$

Source term:

Source terms are generally nonlinear and are first linearized as follows:

$$R_\phi \approx \overline{R}_\phi - R'_\phi \phi_P$$

For the stability of the iterative procedure, it is essential that $R'_\phi \geq 0$. Integration of the source term over a control volume gives

$$\int R_\phi dV \approx \overline{R}_\phi \Delta V - R'_\phi \phi_P \Delta V$$

Combining the equations derived above we get

$$
\begin{aligned}
&[(\varepsilon_m\rho_m\phi)_P-(\varepsilon_m\rho_m\phi)_P^0]\frac{\Delta V}{\Delta t}\\
&\quad+\{\xi_e(\varepsilon_m\rho_m\phi)_E+\overline{\xi}_e(\varepsilon_m\rho_m\phi)_P\}(u_m)_e A_e-\{\xi_w(\varepsilon_m\rho_m\phi)_P+\overline{\xi}_w(\varepsilon_m\rho_m\phi)_W\}(u_m)_w A_w\\
&\quad+\{\xi_n(\varepsilon_m\rho_m\phi)_N+\overline{\xi}_n(\varepsilon_m\rho_m\phi)_P\}(v_m)_n A_n-\{\xi_s(\varepsilon_m\rho_m\phi)_P+\overline{\xi}_s(\varepsilon_m\rho_m\phi)_S\}(v_m)_s A_s\\
&\quad+\{\xi_t(\varepsilon_m\rho_m\phi)_T+\overline{\xi}_t(\varepsilon_m\rho_m\phi)_P\}(w_m)_t A_t-\{\xi_b(\varepsilon_m\rho_m\phi)_P+\overline{\xi}_b(\varepsilon_m\rho_m\phi)_B\}(w_m)_b A_b\\
&\quad+\{(\Gamma_\phi)_e\frac{\phi_E-\phi_P}{\Delta x_e}A_e-(\Gamma_\phi)_w\frac{\phi_P-\phi_W}{\Delta x_w}A_w\}+\{(\Gamma_\phi)_n\frac{\phi_N-\phi_P}{\Delta y_n}A_n-(\Gamma_\phi)_s\frac{\phi_P-\phi_s}{\Delta y_s}A_s\}\\
&\quad+\{(\Gamma_\phi)_t\frac{\phi_T-\phi_P}{\Delta z_t}A_t-(\Gamma_\phi)_b\frac{\phi_P-\phi_B}{\Delta z_b}A_b\}+(\overline{R}_\phi-R'_\phi\phi_P)\Delta V
\end{aligned}
$$

This equation may be rearranged to get the following linear equation for ϕ

$$a_P\phi_P=\sum_{nb}a_{nb}\phi_{nb}+b$$

where the subscript *nb* represents E, W, N, S, T, and B. Before using the above equation for determining ϕ, it is recommended that the discretized continuity equation multiplied by ϕ be subtracted from it. The coefficients are then defined as follows:

$$a_E=D_e-\xi_e(\varepsilon_m\rho_m)_E(u_m)_e A_e$$

$$a_W=D_w+\overline{\xi}_w(\varepsilon_m\rho_m)_W(u_m)_w A_w$$

$$a_N=D_n-\xi_n(\varepsilon_m\rho_m)_N(v_m)_n A_n$$

$$a_S=D_s+\overline{\xi}_s(\varepsilon_m\rho_m)_S(v_m)_s A_s$$

$$a_T=D_t-\xi_t(\varepsilon_m\rho_m)_T(w_m)_t A_t$$

$$a_B=D_b+\overline{\xi}_b(\varepsilon_m\rho_m)_B(w_m)_b A_b$$

$$a_P=\sum_{nb}a_{nb}+a_P^o+R'_\phi\Delta V$$

$$b=a_P^o\phi_P^o+\overline{R}_\phi\Delta V$$

$$a_P^o=\frac{(\varepsilon_m\rho_m)^o}{\Delta t}\Delta V$$

Here, the diffusion contribution, D_e is given by,

$$D_e = \frac{(\Gamma_\phi)_e A_e}{\Delta x_e}$$

Other diffusion terms may be written analogously.

The final form of the discretized equations is:

$$a_P \phi_P = \sum a_{nb} \phi_{nb} + b$$

To ensure the stability of the calculations, it is necessary to under-relax the changes in the field variable during iterations

$$\frac{a_P}{\omega_\phi} \phi_P = \sum_{nb} a_{nb} \phi_{nb} + b + \frac{(1-\omega_\phi)}{\omega_\phi} a_p \phi_P^*$$

where $0 \le \omega_\phi \le 1$. When $\omega_\phi = 0$, the old value remains unchanged. MFIX provides a choice of linear equation solvers, including conjugate gradient and GMRES solvers with preconditioning.

2.3. Outline of Solution Algorithm

For every fluid time step

1) Start of the time step. Calculate physical properties, exchange coefficients, and reaction rates.
2) Calculate fluid velocity fields based on the current pressure field: u_m^*, v_m^*, w_m^*
3) Calculate fluid pressure correction P_g'
4) Update fluid pressure field applying an under relaxation: $P_g = P_g^* + \omega_{pg} P_g'$

5) Calculate fluid velocity correction from P_g' and update fluid velocity fields: e.g., $u_m = u_m^* + u_m'$

6) Complete several iterations of the gas phase until a suitable convergence criterion is met.

7) Begin DES sub-stepping. Use multiple solid time steps for a single fluid time step. At every solid time step

   a) Calculate the inter-particle and particle-wall contact forces

   b) Calculate the gas drag on each particle

   c) Calculate the pressure force on each particle

   d) Calculate each particles acceleration, new velocity and new position

8) End of sub-stepping: calculate the solids volume fraction and the void fraction in each cell. Calculate the solids velocity in each cell. Feed these values into MFIX

9) Compute the drag force exerted by the solid phase on the gas phase. This is done through the gas-phase source term.

10) If the desired time interval for simulation has been reached, stop simulation. Else, go to Step 1.

List of References

1. Andreotti B., and Douady S., 2001, “Selection of velocity profile and flow depth in granular flows”, Phys. Rev. E., Vol. 63, 031305

2. Bagnold R.A., 1954, “Experiments on gravity-free dispersion of large solid spheres in a Newtonian fluid under shear”, Proc. Rey. Soc., Vol. 225, 49-63.

3. Bouillard J. X., Lyczowski R. Y. and Gidaspow D., 1989, “Porosity distributions in a fluidized bed with an immersed obstacle”, AIChE Journal, Vol. 35, 908

4. Blair D.L., Mueggenburg N.W., Marshall A.H., Jaeger H.M., and Nagel S.R., 2001, "Force distributions in 3D granular assemblies: Effects of packing order and inter-particle friction", Phys. Rev. E., Vol. 63, 041304

5. Brennen C.E., Ghosh S., and Wassgren C.R., 1996, “Vertical Oscillation of a bed of granular material”, J. of Applied Mech., Vol. 63, No. 1, 156-161

6. Campbell C.S., 1982, Shear flows in granular material, Ph.D Thesis, California Institute of technology

7. Caps H., and Vandewalle N., 2001, “Ripple and kink dynamics”, Phys. Rev. E., Vol. 64, 041302

8. Choi H.G., and Joseph D.D., 2001, “Fluidization by lift of 300 circular particles in plane Poiseuille flow by direct numerical simulation”, J. Fluid Mech., Vol. 438, 101-128

9. Cleary P.W., 1999, “The effect of particle shape on hopper discharge”, Second International Conference on CFD in the Minerals and Process Industries

10. Cleary P.W., and Joseph H.A., 1999, “Three dimensional modeling of high pressure die casting”, Second International Conference on CFD in the Minerals and Process Industries

11. Clement E., and Duran J., and Rajchenbach J., 1996, “Experimental study of heaping in a two-dimensional sandpile”, Phys. Rev. Lett., Vol. 69, 8, 1189-1192

12. Crowe C., Sommerfeld M., and Tsuji Y., 1998, Multiphase flows with droplets and particles, CRC Press, New York

13. Cundall P.A., and Strack O.D.L., 1979, “A discrete numerical model for granular assemblies” Geotechnique, Vol. 29, No. 1, 47-65

14. Dasgupta S., Jackson R., and Sundaresan S., 1997, “Developing Flow of Gas-Particle Mixtures in Vertical Ducts.” Ind. Eng. Chem. Res., Vol. 36, 3375

15. Dasgupta S., Jackson R., and Sundaresan S., 1998, “Gas-Particle Flow in Vertical Pipes with High Mass Loading of Particles.” Powder Tech., Vol. 96, 6

16. Detamore M.S., Swanson M.A., Frender K.R., and Hrenya C.M., 2001, “A kinetic theory analysis of the scale up of circulating fluidized beds”, Powder tech., Vol. 116, 190-203

17. Douady S., fauve S., and Laroche C., 1989, “Subharmonic instabilities and defects in a granular layer under vertical vibrations”, Europhys. Lett., Vol. 8, 7, 621-627

18. Ehrichs E., Jaeger H., Karczmar G., Knight J.B., and Kuperman V., 1995, “Granular convection observed by magnetic resonance imaging”, Science, Vol. 267, 5204, 1632-1634

19. Evesque P., and Rajchenbach J., 1989, “Instability in a sand heap”, Phys. Rev. Lett., Vol. 69., 1, 44-46

20. Fauve S., Douady S., and Laroche C., 19889, “Collective behaviors of granular masses under vertical vibration”, J. Phys. France, Vol. 50., 3, 187-191

21. Foley J.D., van Dam A., Feiner Ak.K and Hughes J.F., 1997, Computer graphics: Principles and practice, Second edition, Adison-Wesley Publishing Company

22. Gallas J., Herrmann H., and Sokolowski S., 1992,”Convection cells in vibrating granular media”, Phys. Rev. Lett., Vol. 69, 9, 1371-1374

23. Garside, J. and Al-Dibouni, M.R., Velocity-voidage relationships for fluidization and sedimentation, I&EC Pro. Des. Dev., Vol. 16, pp206-214, 1977.

24. Gera D. and Tsuji Y., 1997, “A legend from potential flow theory to discrete particle simulations”, Invited paper: Hydrodynamics of fluidization

25. Glasser B.J., Kevrekidis Y.G., and Sundaresan S., 1996, "One- and Two-Dimensional Traveling Wave Solutions in Gas-Fluidized Beds." J. Fluid Mech., Vol. 306, 183

26. Glasser B.J., Kevrekidis Y.G., and Sundaresan S.,1997, "Fully-Developed Traveling Wave Solutions and Bubble Formation in Fluidized Beds." J. Fluid Mech., Vol. 334, 157

27. Glasser B.J., Sundaresan S., and Kevrekidis Y.G., 1998 "From Bubbles to Clusters in Fluidized Beds." Phys. Rev. Lett., Vol. 81, 1849

28. Goldhirsch I., and Zanetti G., 1993, “Clustering instability in dissipative gases”, Phys. Rev. lett., Vol. 70, 1619-1622

29. Göz M.G., Glasser B.J., and Kevrekidis Y.G., and Sundaresan S., 1996, “Traveling Waves in Multi-Phase Flows.” Adv. Fluid Mech., Vol. 9, 307

30. Göz M.F., and Sundaresan S., 1998, “The Growth, Saturation, and Scaling Behavior of One- and Two-Dimensional Disturbances in Fluidized Beds.” J. Fluid Mech., Vol. 362, 83

31. Hunt M.L., Weathers R.C., Lee A.T., and Brennen C.E., 1999, “Effects of horizontal vibration on hopper flows of granular materials”, Physiscs of Fluids, Vol. 11, 68-75

32. Jaeger H., and Nagel S., 1992, “Physics of the granular state”, Science, Vol. 255, 5051, 1523-1531

33. Jenkins, J.T., and Savage, S. B., 1983, “A theory for the rapid flow of identical, smooth, nearly elastic, spherical particles”, J. Fluid Mech., Vol. 130, 187-202

34. Josserand C., Tkachenko A., Mueth D.M., and Jaeger H.M., 2000, "Memory effects in shaken granular material," Phys. Rev. Lett., Vol. 85, 3632-3635

35. Knight J.B., Jaeger H.M., Nage S.R., 1993, “Vibration-induced size seperation in granular media: the convection connection”, Phys. Rev. Lett., Vol. 70, 24, 3728-3731

36. Knight J.B., Ehrichs E.E., Kuperman V.Y., Flint J.K., Jaeger H.M. and Nagel S.R., 1996, “An experimental study of granular convection”, Phys. Rev. E.

37. Li, Jie and Kuipers, J.A.M., Gas-particle interactions in dense gas-fluidized beds, Chemical Engineering Science, Vol. 58, pp711-718, 2003.

38. Limtrakul, S., Chalermwattanatai, A., Unggurawirote, K., Tsji, Y., Kawaguchi, T., Tanthapanichakoon, W., Discrete particle simulation of solids motion in a gas-solid fluidized bed, Chemical Engineering Science, Vol. 58, pp915-921, 2003.

39. Lohner R., 1998, “Some useful data structures for the generation of unstructures grids”, Communications in Applied Numerical Methods, Vol. 4, 123-135

40. Lun, C.K.K., Savage, S. B., Jeffery, D.J., and Chepuriny, N., 1984, “Kinetic theories for granular flow: inelastic particles in Couette flow and slightly inelastic particles in a general flowfield”, J. Fluid Mech., Vol. 140, 223-256

41. Massoudi M., and Boyle E.J., 1991, “A review of theories for flowing granular materials with applications to fluidized beds and solids transport”, DOE/PETC/TR-91/8 (DE9101311), Pittsburgh Energy Technology Center, Pittsburgh

42. Medved M., 2002, "Connections between response modes in a horizontally driven granular material", Phys. Rev. E., Vol. 65, 021305

43. Medved M., Jaeger H.M., and Nagel S.R., 2000, "Modes of Response in Horizontally Vibrated Granular Material", Europhys. Lett., Vol. 52, 66

44. Medved M., Jaeger H.M., and Nagel S.R., 2001, "Convection in a fully immersed granular slurry", Phys. Rev. E., Vol. 63, 061302

45. Melo F., Umbanhower P., and Swinney H., 1994, “Transition to parametric wave patterns in a vertically oscillated granular layer”, Phys. Rev. Lett., Vol. 72, 1, 172-175

46. Melo F., Umbanhower P., and Swinney H., 1995, “Hexagons, kinks and disorder in oscillated granular layers”, Phys. Rev. Lett., Vol. 75, 21, 3838-3841

47. Metcalf T.H., Knight J.B., and Jaeger H.M., 1996, “Standing wave patterns in shallow beds of vibrated granular material”

48. Miles J., and Henderson D., 1990, “Parametrically forced surface waves”, Ann. Rev. Fluid. Mech., Vol. 22, 143-165

49. Möbius M.E., Lauderdale B.E., Nagel, S.R. and Jaeger H.M., 2001, “Size Separation of Granular Particles”, Nature 414, 270

50. Mortenson E., 1997, Geometric Modeling, John Wiley & Sons Inc

51. Moslemian D., 1987, “Study of solids motion, mixing and heat transfer in gas-solid fluidized beds”, PhD thesis, University of Illinois, USA.

52. Mueth D.M, Debregeas G.F., Karczmar G.S., Eng P.J, Nagel S.R., and Jaeger H.M., 2000, “Signatures of granular microstructure in dense shear flows”, Nature 406, 385

53. Mueth D.M., Jaeger H.M., and Nagel S.R., 1998, “Force Distribution in a Granular Medium”, Physical Review E., Vol. 57, 3164-3169

54. Munjiza A., and Andrews K.R.F.,1998, “NBS contact detection algorithm for bodies of similar size”, Int. J. Numerical Methods in Eng., Vol. 43, 131-149

55. Nakanishi H., and Toyoshima S., 1991, “Gas-solid flow simulation of discharge of powder coal from a bin”, Ga-Solis Flows, ASME, Vol. 121

56. Nott P.R., Alam M., Agrawal K., Jackson R., and Sundaresan S., 1999, “The Effect of Boundaries on the Plane Couette Flow of Granular Materials: A Bifurcation Analysis.” J. Fluid Mech., Vol. 397

57. Pak H., and Behringer R., 1993, “Surface waves in vertically vibrated granular materials”, Phys. Rev. Lett., Vol. 71, 12, 1832-1835

58. Pan T.W., Joseph D.D., Bai R., Glowinski R., and Sarin V., 2001,“Fluidization of 1204 spheres: simulation and experiment”, J. Fluid Mech.

59. Patankar N.A., and Joseph D.D., 2001, “Lagrangian numerical simulation of particulate flows”, Int. J. Multiphase Flow, Vol. 27, 10, 1685-1706

60. Patankar N.A., and Joseph D.D., 2001, “Modeling and numerical simulation of particulate flows by the Eulerian-Lagrangian approach”, Int. J. Multiphase Flow, Vol. 27. 10, 1659-1684

61. Patankar N.A., Huang P.Y., Ko T., and Joseph D.D., “Lift-off of a single particle in Newtonian and viscoelastic fluids by direct numerical simulation”, J. Fluid Mech., Vol. 438, 67-100

62. Patankar N.A., Ko T., Choi H.G., and Joseph D.D., 2001, “A correlation for the lift-off of many particles in plane Poiseuille flows of Newtonian fluids”, J. Fluid Mech., Vol. 445, 55-76

63. Patanker S.V., 1980, Numerical heat transfer and fluid flow, McGraw Hill, New York

64. Popken L., and Cleary P.W., 1999, “Comparison of kinetic theory and discrete element schemes for modeling granular couette flows”, J. Computational Physiscs, Vol. 155, 1-25

65. Rajchenbach J., 1991, “Dilatant process for convection motion in a sand heap”, Europhys. Lett., Vol. 16., 2, 149-152

66. Rajchenbach J., 2001, “Stress transmission through textured granular packings”, Phys. Rev. E., Vol 63, 041301

67. Rhodes M.J., Wang X.S., Nyugen M., Stewart P., and Liffman K., 2001, “Onset of cohesive behavior in gas fluidized beds: a numerical study using DEM”, Chemical Engineering Science, Vi. 56, 4433-4438

68. Richardson, J.F., and Zaki, W.N., Sedimentation and fluidization: Part I, Trans. Inst. Chem. Eng. Vol 32, pp35-53, 1954.

69. Savage, S. B., and Jeffery, D.J., 1981, "The stress tensor in a granular flow at high shear rates", J. Fluid Mech., Vol. 110, 255-272

70. Savage S.B., 1984, "The mechanics of rapid granular flows", advances in Applied Mechanics, Vol. 24, 289-366

71. Savage S.B., 1988, "Streaming motions in a bed of vibrationally fluidized dry granular material", J. Fluid Mech., Vol. 194., 457-478

72. Sawley L.M. and Cleary P.W., 1999, "A parallel discrete element method for industrial granular flow simulations", EPFL-Supercomputing Review

73. Srivastava A., Agrawal K., Reddy Karri S.B., and Knowlton T.M., and Sundaresan S., 1998, "Dynamics of Gas-Particle Flow in Circulating Fluidized Beds." Powder Tech., Vol. 100, 173

74. Syamlal, M. and O'Brien, T.J., Simulation of granular layer inversion in liquid fluidized beds, Int. J. Multiphase Flow, Vol. 14, pp. 473-481, 1988.

75. Syamlal, M., Roger, W., and O'Brien, T.J., MFIX documentation: theory guide, Technical Note, DOE/METC-94/1004, NTIS/DE94000087, National Technical Information Service, Springfield, VA. 1994a.

76. Syamlal, M., MFIX documentation: user's manual, technical note, DOE/METC-95/1013, NTIS/DE95000031, National Technical Information Service, Springfield, VA. 1994b.

77. Syamlal, M., MFIX documentation: numerical technique, technical note, DOE/MC31346-582495, NTIS/DE98002029, National Technical Information Service, Springfield, VA. 1998.

78. Taguchi Y-h., 1992, "New origin of convective motion: elastically induced convection in granular materials", Phys. Rev. Lett., Vol. 69, 9, 1367-1370

79. Tanaka T, Kajiwara Y., and Inada T., 1988, "Flow dynamics of granular materials in a hopper", Trans of ISIJ, Vol. 28, 907-915

80. Tanaka T, Mituji H., and Takahashi T., 1986, "Extractive Fluidized Classification", Advanced Powder technology, Vol. 7, 575-591

81. Tsuji Y., Shen N-Y., and Morikawa Y., 1991, "Lagrangian simulation of dilute gas-solid flows in a horizontal pipe", Adv. Powder Tech., Vol. 2, 63

82. Tsuji Y., Tanaka T., and Ishida T., 1992, “Lagrangian simulation of plug flows of cohesionless particles in a horizontal pipe”, Powder Tech., Vol. 71, 239-250

83. Tsuji Y., Kawaguchi T., and Tanaka T., 1993, “Discrete particle simulation of two dimensional fluidized bed”, Powder Tech., Vol. 77, 79-87

84. Villarruel F., Lauderdale B., Mueth D.M., and Jaeger H.M., 2000, "Compaction of rods: Relaxation and Ordering in Vibrated, Anisotropic Granular Material", Phys. Rev. E, Vol. 61, 6914

85. Wang D., and Campbell C.S., 1992, “Reynolds analogy for a shearing granular material”, J. Fluid Mech., Vol. 244, 527-546

86. Wang C-H, Jackson R., and Sundaresan S., 1996, “Stability of Bounded Shear Flow of Granular Materials.” J. Fluid Mech., Vol. 308, 31

87. Wang C-H, Jackson R.,and Sundaresan S., 1997 “Instabilities of Fully-Developed Rapid Flow of Granular Material in a Channel.” J. Fluid Mech., Vol. 342, 179

88. Wassgren C.R., Brennen C.E., and Hunt M.L., 1995, “Granular flow in vertically vibrating hopper”, Proceedings of the 10th ASCE Engineering Mechanics Conference

89. Wassgren C.R., Brennen C.E., and Hunt M.L., 1996, “Vertical vibration of a deep bed of granular material in a container”, J. Applied Mechanics, Vol. 63, 712-719

90. Wassgren C.R., Hunt M.L., Brennen C.E., 1997, “Investigation of f/2 and f/4 waves in granular beds subject to vertical sinusoidal oscillations”, Proceedings of the 3rd International Conference on Powders and Grains

91. Wassgren C.R., 1996, “Vibration of granular material”, Ph.D Thesis, California Institute of technology

92. Xu B.H., and Yu A.B., 1997, “Numerical simulation of the gas-solid in a fluidized bed by combining discrete particle method with computational fluid dynamics”, J. Chemical Engineering Science, Vol. 52, 2785-2809